

Understanding Subduction-Zone Rheology and Crustal Deformation  
in Earthquake Cycles

by

Haipeng Luo  
B.Sc., Wuhan University, China, 2014  
M.Sc., Wuhan University, China, 2017

A Dissertation Submitted in Partial Fulfillment  
of the Requirements for the Degree of

DOCTOR OF PHILOSOPHY

in the School of Earth and Ocean Sciences

© Haipeng Luo, 2021  
University of Victoria

All rights reserved. This dissertation may not be reproduced in whole or in part, by  
photocopy or other means, without the permission of the author.

## **Supervisory Committee**

### Understanding Subduction-Zone Rheology and Crustal Deformation in Earthquake Cycles

by

Haipeng Luo

B.Sc., Wuhan University, China, 2014

M.Sc., Wuhan University, China, 2017

#### **Supervisory Committee**

Dr. Kelin Wang (School of Earth and Ocean Sciences)

**Co-Supervisor**

Dr. Edwin Nissen (School of Earth and Ocean Sciences)

**Co-Supervisor**

Dr. Stan Dosso (School of Earth and Ocean Sciences)

**Departmental Member**

Dr. Henning Struchtrup (Department of Mechanic Engineering)

**Outside Member**

## Abstract

### **Supervisory Committee**

Dr. Kelin Wang (School of Earth and Ocean Sciences)

### **Co-Supervisor**

Dr. Edwin Nissen (School of Earth and Ocean Sciences)

### **Co-Supervisor**

Dr. Stan Dosso (School of Earth and Ocean Sciences)

### **Departmental Member**

Dr. Henning Struchtrup (Department of Mechanic Engineering)

### **Outside Member**

My PhD program is focused on how earthquake cycle deformation in subduction zones is governed by the rheology of the asthenosphere and lithosphere. The method of research is numerical modelling of deformation processes constrained by geodetic observations. This dissertation includes research results on the three deformation phases of earthquake cycles, namely the coseismic, postseismic, and interseismic phases.

**Coseismic:** Tension cracks were produced by megathrust earthquakes in the Chile-Peru forearc, seemingly challenging the elastic rebound theory. We explain the cracks as the consequence of less or no interseismic stress accumulation in the near-surface material due to its viscoelastic behaviour, in contrast to the deeper elastic crust. Elastic rebound of the deeper crust during earthquakes induces more stress in the near-surface material than has been accumulated and thus generates the tensile failure. The results confirm the validity of the elastic rebound theory and highlight the importance of understanding the heterogeneity of lithosphere rheology.

**Postseismic:** A sharp contrast between the cold forearc and hot arc and backarc, considered fundamental to subduction dynamics, indicates the presence of a cold mantle wedge nose, but direct evidence is limited. The cold nose, if present, should behave elastically for the time scale of earthquake cycles. Through modelling postseismic vertical motion following great subduction earthquakes, we propose and demonstrate that global observations of postseismic uplift just seaward of the volcanic arc provide a geodetic signature of the cold nose. This finding helps to establish a link between the relatively short-term earthquake cycle deformation with long-term thermo-petrologic

processes. It also solves a mystery that has puzzled the scientific community for six decades regarding crustal deformation caused by the largest recorded earthquake on Earth – the 1960 moment magnitude ( $M_w$ ) 9.5 Chile earthquake.

**Interseismic:** In the southern area of the 1960  $M_w$  9.5 Chile earthquake, regional geodetic measurements in the 21st century show a rapid systematic landward increase in the velocity of station motion that cannot be explained by the standard viscoelastic earthquake cycle model. We propose that the velocity increase is due to a sudden downdip widening of the zone of megathrust locking. This finding not only raises new theoretical questions for the study of megathrust fault mechanics but also has important implications to assessing seismic hazard in the subduction zone environment.

In addition to the earthquake cycle deformation studies, we explore along-strike viscosity variations in a slab window associated with the Chile triple junction which terminated the southward rupture propagation of the 1960 Chile earthquake. We model geodetically observed ongoing surface uplift due to recent climatically induced mass loss at the Patagonian icefields that are situated just above the slab window. The results suggest an order of magnitude viscosity contrast within the slab window, with the younger and thus warmer northern part being much less viscous. This case study provides an example for how the anatomy of an active tectonic system can be geodetically “imaged” using non-tectonic signals.



## Table of Contents

Supervisory Committee .....	ii
Abstract.....	iii
Table of Contents .....	v
List of Tables .....	vii
List of Figures.....	viii
Acknowledgements .....	x
Chapter 1. Introduction.....	1
Chapter 2. Coseismic tension cracks in the Chile-Peru forearc reflecting viscoelastic behaviour of near-surface material .....	5
2.1. Article Information .....	5
2.2. A model of shallow viscoelastic relaxation for seismically induced tension cracks in the Chile-Peru forearc .....	6
2.2.1. Abstract.....	6
2.2.2. Plain Language Summary.....	7
2.2.3. Introduction .....	7
2.2.4. Basic Concepts and Modelling Strategy.....	9
2.2.4.1. Near-surface Viscoelasticity.....	9
2.2.4.2. Conceptual Model for Forearc Cracks .....	10
2.2.4.3. Numerical Model .....	12
2.2.5. Model Results .....	12
2.2.5.1. Reference Model .....	12
2.2.5.2. Testing the Role of Downdip Rupture Termination.....	15
2.2.5.3. Application to the 2014 Iquique Earthquake .....	17
2.2.6. Conclusions .....	18
2.2.7. Acknowledgements .....	19
2.3. Supporting Information .....	20
Chapter 3. Postseismic uplift near volcanic arc as the geodetic signature of cold mantle wedge corner.....	26
3.1. Article Information .....	26
3.2. Postseismic geodetic signature of cold forearc mantle in subduction zones .....	27
3.2.1. Abstract.....	27
3.2.2. Introduction .....	28
3.2.3. Postseismic uplift due to viscoelastic stress relaxation .....	30
3.2.4. Modelling modern geodetic postseismic observations.....	32
3.2.5. Postseismic deformation of the 1960 giant Chile earthquake .....	35
3.2.6. Other contributing factors.....	37
3.2.7. Methods .....	38
3.2.8. Acknowledgements .....	39

3.3. Extended Data.....	40
Chapter 4. Landward increase in GNSS velocities in South Chile indicating enhanced interseismic megathrust locking .....	52
4.1. Article Information .....	52
4.2. A recent increase in megathrust locking in the southernmost rupture area of the giant 1960 Chile earthquake .....	54
4.2.1. Abstract.....	54
4.2.2. Introduction .....	54
4.2.3. Geodetic Observations.....	57
4.2.3.1. Two-decade displacement history at site COYQ .....	57
4.2.3.2. A regional increase in eastward velocity .....	62
4.2.4. Case for a recent increase in megathrust locking .....	65
4.2.4.1. The finite element model .....	65
4.2.4.2. A model of enhanced locking.....	66
4.2.4.3. A model of slow slip followed by enhanced locking .....	69
4.2.4.4. Discussion of enhanced locking .....	71
4.2.5. Conclusions .....	73
4.2.6. Acknowledgements .....	74
4.3. Supplementary Material .....	75
4.3.1. Decomposition of signals in COYQ time series.....	75
4.3.2. GNSS Data .....	76
5. Conclusions .....	78
Appendix. Along-strike viscosity variation in Chile slab window inferred from uplift due to recent glacial melting .....	80
A.1. Article Information .....	80
A.2. Lateral variation in slab window viscosity inferred from global navigation satellite system (GNSS)-observed uplift due to recent mass loss at Patagonia ice fields...82	82
A.2.1. Abstract.....	82
A.2.2. Introduction .....	82
A.2.3. Ice mass loss and its geodetic signature .....	84
A.2.4. Modelling GIA above the slab window.....	86
A.2.4.1. Along-strike Viscosity Contrast .....	86
A.2.4.2. Uncertainties in Ice Loss History .....	88
A.2.5. Discussion.....	88
A.2.6. Conclusion.....	90
A.2.7. Acknowledgements .....	91
A.3. Supplemental Material.....	91
A.3.1. Modelling Method .....	91
A.3.2. Supplemental Figures and Tables.....	93
Bibliography .....	100

## List of Tables

Table 3.1. Summary of postseismic forearc uplift observations following subduction earthquakes .....	48
Table 3.2. Parameters for the postseismic deformation models of the four earthquakes shown in Figure 3.3 .....	50
Table 4.1. Values of the parameters in equation 4.1 for the COYQ time series .....	76
Table 4.2. GNSS site velocities for the 2010–2019 measurements in southern Chile. ....	77
Table A.1. Newly obtained uplift rates for the ten continuous GNSS sites shown in Figure A.1a.....	93
Table A.2. Chile-ridge Slab window viscosity values and roomt-mean-square fit to GNSS data in different models .....	94

## List of Figures

Figure 1.1. An overview of the research topics in this dissertation .....	2
Figure 2.1. Reported surface cracks along the Chile–Peru forearc and association with megathrust rupture.....	8
Figure 2.2. Conceptual model for the formation of forearc cracks .....	11
Figure 2.3. The 2D reference model for the modelling in Chapter 2 .....	14
Figure 2.4. Controlling effects of downdip rupture termination on crack generation.....	16
Figure 2.5. Cross-section view of the reference 2D model of stress change summarized in Figure 2.3.....	20
Figure 2.6. Similar to Figure 2.5 but for a model in which the mantle exhibits bi-viscous transient viscoelastic rheology.....	21
Figure 2.7. Similar to Figure 2.3 but for the model shown in Figure 2.6.....	22
Figure 2.8. Coseismic slip of the 2014 Iquique earthquake and surface stresses induced by it.....	23
Figure 2.9. Megathrust slip and crustal stress along the profile shown in Figure 2.8.....	25
Figure 3.1. Schematic illustration of thermal and rheological structure in subduction zones.....	29
Figure 3.2. 2D models of postseismic deformation to illustrate the physical process discussed in Chapter 3 .....	31
Figure 3.3. Model postseismic vertical deformation for four subduction earthquakes compared with observations .....	34
Figure 3.4. Observed and modelled deformation associated with the 1960 $M_w$ 9.5 Chile earthquake.....	36
Figure 3.5. Global synthesis of postseismic uplift following subduction earthquakes observed in the forearc near the volcanic arc .....	40
Figure 3.6. Map view of observed and modelled postseismic deformation 5 years after the 2011 $M_w$ 9 Tohoku-oki earthquake.....	41
Figure 3.7. Observed and modelled time series of GNSS sites after the 2011 $M_w$ 9 Tohoku-oki earthquake.....	42
Figure 3.8. Map view of observed and modelled postseismic deformation 5 years after the 2010 $M_w$ 8.8 Maule earthquake .....	43
Figure 3.9. Observed and modelled time series of GNSS sites after the 2010 $M_w$ 8.8 Maule earthquake .....	44
Figure 3.10. Map view of observed and modelled postseismic deformation 5 years after the 2007 $M_w$ 8.4 Bengkulu earthquake .....	45
Figure 3.11. Observed and modelled time series of GNSS sites after the 2007 $M_w$ 8.4 Bengkulu earthquake .....	46
Figure 3.12. 2-D Models of postseismic deformation to test the effects of upper plate thickness .....	47
Figure 4.1. Schematic illustration of postseismic deformation of subduction earthquakes .....	56
Figure 4.2. Observed and model-predicted GNSS site velocities in southern Chile.....	57
Figure 4.3. Time history of weekly position of GNSS site COYQ .....	59
Figure 4.4. Definition of the South America (SA) reference frame .....	60
Figure 4.5. Regional change in GNSS velocity in the early 21st century .....	63

Figure 4.6. Rapid decrease in west velocity with respect to SA (Figure 4.4) at GNSS site COYQ explained with a model of enhanced megathrust locking .....	67
Figure 4.7. Regional map view of the enhanced locking model and site velocities prior to the locking increase .....	68
Figure 4.8. An alternative to the model of Figures 4.6 and 4.7 seen at COYQ: A slow slip event followed by enhanced locking .....	70
Figure 4.9. Regional map view of the model shown in Figure 4.8 .....	72
Figure A.1. Regional tectonic setting of and GNSS velocities at the Patagonian ice fields.....	83
Figure A.2. Model settings of our preferred Chile-ridge slab window model.....	85
Figure A.3. Results of glacial isostatic adjustment models for Chile-ridge slab window... ..	87
Figure A.4. Geodynamics and crustal deformation in the region of Chile triple junction ... ..	90
Figure A.5. Ice mass loss history of Northern and Southern Patagonia ice fields and thinning rates of models .....	95
Figure A.6. Weekly vertical positions of the GNSS sites listed in Table A.1 .....	96
Figure A.7. Vertical as well as horizontal deformation predicted by the 3D preferred model shown in Figure A.3a and by a 1-D model.....	98
Figure A.8. Three test models that can roughly explain the GNSS data shown in Figure A.1b .....	99

## Acknowledgements

I thank my supervisor, Dr. Kelin Wang, for the opportunity of doing my PhD at the School of Earth and Ocean Sciences (SEOS), University of Victoria (UVic), and for the scientific knowledge and research philosophy I learned from him.

I thank my co-supervisor Dr. Edwin Nissen for helping me in many ways during my stay at UVic and my other committee members, Dr. Stan Dosso and Dr. Henning Struchtrup, for their guidance.

I thank Dr. Jiangheng He at the Pacific Geoscience Centre (PGC), Geological Survey of Canada, for developing the numerical code used in my research and for his help during my study.

I thank Dr. Thomas James at PGC for improving my knowledge of glacial melting induced deformation. I thank Dr. Garry Rogers at PGC for helping to improve my knowledge of plate tectonics when we were office mates before my candidacy exam.

I thank my international coauthors Boudewijn Ambrosius, Raymond M. Russo, Victor Mocanu, Hiroki Sone, Rui Fernandes and Michael Bevis for the fruitful collaborations during my PhD.

I thank fellow students, colleagues, and visiting students and scientists at SEOS and PGC for their help and fruitful discussion: Yijie Zhu, Tianhaozhe Sun, Matías Carvajal (University of Concepcion, Chile), Yuji Itoh (University of Tokyo, Japan), Xin Zhou (China Earthquake Administration), Matthew Sypus, Dawei Gao, Megan Caston, Taizi Huang, Fengzhou Tan, Max Lauch, and Yang Wang (University of Chinese Academy of Sciences, China). I thank Carlos Herrera, Israporn (Grace) Sethanant, and Fatemeh Nemati at SEOS for nominating me as a Graduate Representative at Faculty of Graduate Studies Council and Rebecca Morris at SEOS for her help during my tenure on the council. I thank Department Secretary Allison Rose, Graduate Program and Office Support Secretary Kalisa Valenzuela at SEOS, and Finance and Administration Officer Barbara Anderson (retired) at PGC for their help in my SEOS/PGC life.

I thank my family in China for their support, especially my mother Erjun Bu.

## Chapter 1. Introduction

Knowing how subduction zone rheology governs earthquake cycles is important to understanding subduction geodynamics. Understanding the interplay between megathrust slip/locking behaviour and mantle rheology helps to understand how strain energy is accumulated and released in earthquake cycles and therefore contributes to the assessment of earthquake and tsunami hazards. Crustal deformation associated with subduction earthquake cycles consists of three phases. (1) During an earthquake, the megathrust fault ruptures within seconds to minutes, in which both the tectonic plates (subducting plate and upper plate) and the asthenospheric mantle deform elastically. (2) After the earthquake, parts of the fault may continue to creep (called afterslip), and viscoelastic relaxation of the stress induced in ductile rock by the earthquake rupture causes continuing deformation that lasts years to many decades. (3) Between earthquakes, the megathrust is locked, and strain is accumulated in the lithosphere in preparation for a future rupture. The three deformation phases are termed coseismic, postseismic, and interseismic phases, respectively, although the difference between the last two phases is not very distinct. The materials presented in this dissertation address one aspect for each of the three phases (Figure 1.1). The research method is exclusively numerical modelling. Model constraints are primarily geodetic measurements of crustal deformation but in some cases also include other geophysical or geological observations. The data are either provided by collaborating colleagues (coauthors) or obtained by synthesizing those available in the literature.

For the coseismic phase, the physical process is rather well understood. The observed deformation is consistent with the theory of elastic rebound, as has been reported by vast amounts of literature over the past century. Therefore, I do not further investigate the general deformation mechanism in the coseismic phase but only focus on explaining an intriguing set of geological observations from the Chile-Peru subduction zone indicating permanent surface deformation that appears to be inconsistent with elastic rebound. This is the subject of Chapter 2, which has been published as a paper in *Geophysical Research Letters* (Luo et al., 2019). In this study, I demonstrate that the elastic rebound theory is still valid at the crustal scale and that the observed permanent deformation is a result of

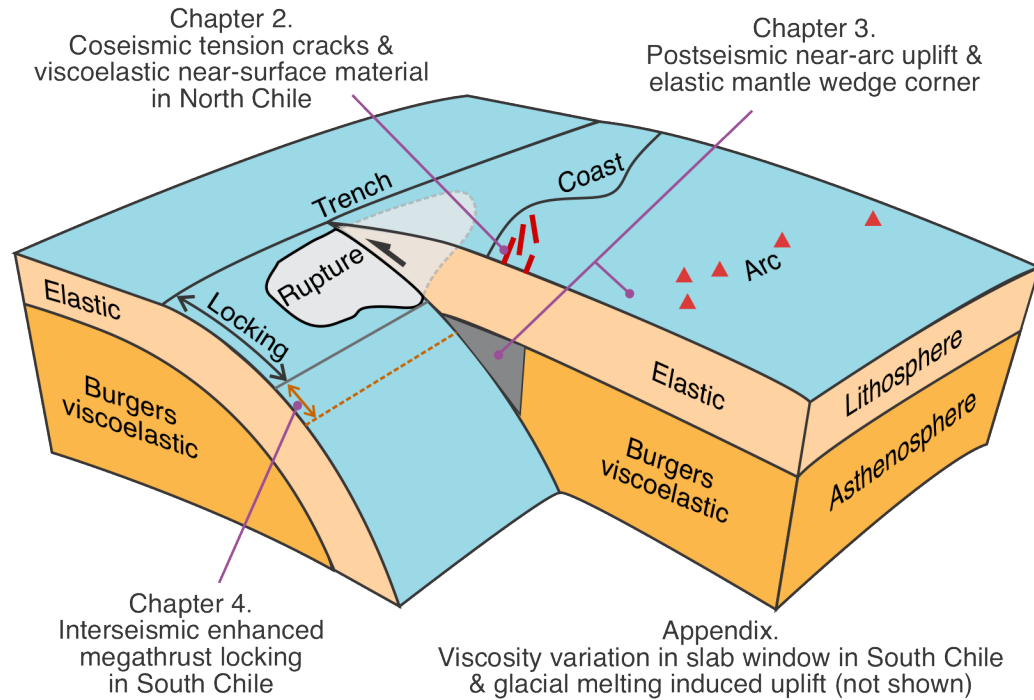


Figure 1.1. An overview of the research topics in this dissertation. The subduction-zone structure is modified from Wang et al. (2012).

the viscoelastic rheology of the near-surface material.

The study of the postseismic phase is the largest component of my PhD program. Geodetic and other geophysical measurements of the motions of Earth's crust in the 20th and 21st centuries have provided important observational constraints. The postseismic deformation in the horizontal direction is particularly well studied and understood (e.g., Wang et al., 2012; Moreno et al., 2012; Kogan et al., 2013; Sun et al., 2014, 2018; Govers et al., 2018). After a great subduction earthquake, postseismic horizontal deformation exhibits opposing motion in which the rupture area moves landward and the inland areas moves seaward, due mainly to the viscoelastic stress relaxation with the additional effects of afterslip. The vertical motion, however, is not as well understood for several reasons. First, observational uncertainties are much larger in the vertical dimension. Geodetic observation of earthquake deformation at subduction zones over the past two decades has relied predominantly on Global Navigation Satellite System (GNSS). It is well known that errors in GNSS measurements in the vertical direction are



larger by a factor of three than in the horizontal directions. Second, even for observations with adequately good signal-to-noise ratios, postseismic vertical deformation exhibits a pattern more complex than the horizontal component. Third, the vertical deformation which reflects tilting of the crustal surface is much more sensitive to structural and rheological heterogeneities than is the horizontal deformation which reflects straining of the crust (e.g., Wang and Tréhu, 2016; Wang et al., 2018). My PhD research on the postseismic phase places much greater emphasis on the less understood vertical component. This is the subject of Chapter 3, which is a paper published in *Nature Geoscience* (Luo and Wang, 2021). The study takes advantage of the structural and rheological sensitivity of vertical deformation and demonstrates that short-term (a few years) postseismic uplift near the volcanic arc provides diagnostic geodetic signature for the ubiquitous presence of a cold forearc mantle wedge in global subduction zones. The data used are synthesized from many publications reporting postseismic deformation for practically all magnitude  $\geq 7.8$  subduction megathrust earthquakes worldwide. The work contributes to the understanding of the thermal and petrologic structure of subduction zones.

The effect of the viscoelastic relaxation of the earthquake-induced stress mentioned above diminishes with time, and the crustal deformation gradually becomes dominated by the effect of fault locking and eventually features wholesale landward motion (Wang et al., 2012). The transition from opposing motion to wholesale landward motion vaguely defines the transition from the postseismic to the interseismic phase, with the timing and gradualness of the transition depending on the size of the earthquake (Sun et al., 2018). There is massive literature reporting the use of interseismic geodetic observations to infer kinematically the locking state of the megathrust. My contribution is to report a new phenomenon in interseismic locking. This is the subject of Chapter 4, which is a paper published in *Earth and Planetary Science Letters* (Luo et al., 2020). In this study, we report a premature and rapid reversal of crustal motion, from seaward to landward, half a century after the 1960  $M_w$  9.5 Chile earthquake in Southern Chile. We demonstrate that the rapid change indicates a sudden downdip widening of the zone of fault locking, for which the physical mechanism deserves new research. This is an international collaboration, and the GNSS data used in this study are provided by our U.S. and

European collaborators.

In addition to studying how Earth rheology controls the three phases of the earthquake cycle, a small part of my PhD research is on constraining mantle rheology in a subduction environment by modelling glacial isostatic adjustment. The paper that reports the results has been published in the journal *Geology* (Russo et al., 2021) and is included in this dissertation as an Appendix. By modelling the uplift rate associated with the recent mass loss of the Patagonian icefields, we are able to constrain significant lateral variations in viscosity. As the second author of this *Geology* paper, I conceived the main idea of the work and conducted all the modelling. This is a second component of the international collaboration that led to Chapter 4. The data used include new data provided by the same collaborators and additional data from the literature.

## **Chapter 2. Coseismic tension cracks in the Chile-Peru forearc reflecting viscoelastic behaviour of near-surface material**

This chapter addresses an important aspect of coseismic stress change associated with subduction earthquakes. The main body of this chapter consists of a published journal article [Luo et al., 2019]. The chapter consists of three sections, with Section 2.1 describing basic information of the article, Section 2.2 presenting the article itself, and Section 2.3 presenting the Supporting Information accompanying the published article. The data sets providing numerical values of model results in figures accompanying the published article are not presented here.

### **2.1. Article Information**

#### **2.1.1. Author and Coauthor Contributions**

The author of this dissertation H.L. carried out the modelling. Coauthor K.W. designed the study. Coauthor J.H. wrote the numerical code for the modelling and contributed to the construction of models. Coauthor H.S. provided information on the rheology of near-surface rocks. H.L. and K.W. wrote the manuscript and all authors contributed to the revision.

#### **2.1.2. Citation**

Luo, H., Wang, K., Sone, H., & He, J. (2019). A model of shallow viscoelastic relaxation for seismically induced tension cracks in the Chile-Peru forearc. *Geophysical Research Letters*, 46(19), 10773-10781. doi: 10.1029/2019GL084536

#### **2.1.3. Author's Names and Affiliations**

H. Luo<sup>1</sup>, K. Wang<sup>2,1</sup>, H. Sone<sup>3</sup>, and J. He<sup>2</sup>

<sup>1</sup>School of Earth and Ocean Sciences, University of Victoria, Victoria, British Columbia, Canada

<sup>2</sup>Pacific Geoscience Centre, Geological Survey of Canada, 9860 West Saanich Road, Sidney, British Columbia, Canada

<sup>3</sup>Department of Civil and Environmental Engineering, University of Wisconsin-Madison, Madison, WI, USA

Corresponding author: Kelin Wang (kelin.wang@canada.ca)

#### **2.1.4. Article Format**

The text and figures included in Section 2.2 are taken directly from the Geophysical Research Letters article. The Supporting Information published together with the article is given in Section 2.3. Sections and figures in the original article have been renumbered to be compatible with the chapter format of the dissertation. Words that used American spelling as required by the journal have been changed to Canadian spelling in this chapter. References cited in the article are included in the bibliography of the dissertation.

### **2.2. A model of shallow viscoelastic relaxation for seismically induced tension cracks in the Chile-Peru forearc**

#### **2.2.1. Abstract**

Tension cracks were generated by past megathrust earthquakes along the coastal forearc of Chile–Peru. To explain why elastic rebound in an offshore earthquake can cause widespread permanent deformation onshore, we propose a model in which the near-surface material exhibits viscoelastic behaviour, analogous to laboratory observed behaviour of petroleum reservoir rocks. Because of near-surface relaxation, interseismic deformation builds up stress only in the deeper crust. Elastic rebound of the deeper crust during an earthquake induces near-surface tension to generate cracks. We numerically demonstrate the proposed mechanism using hypothetical and real megathrust earthquakes. The location of the zone of peak tension, assumed to be responsible for the crack generation, is controlled by downdip rupture termination. A rupture farther downdip or terminating more gradually causes the zone of peak tension to be farther landward and broader. The tension cracks thus may contain important information on megathrust rupture dynamics.

### 2.2.2. Plain Language Summary

Earthquakes are the operation of elastic rebound. Tension cracks induced by megathrust earthquakes observed in Chile-Peru therefore require special explanation. In this work, we propose a testable model for these cracks. We propose that the cemented soil and the highly fractured shallow bedrock in this area exhibit a viscoelastic behaviour analogous to petroleum reservoir rocks. When the megathrust is locked in preparation for the next earthquake, the deeper crust is elastically shortened like a spring, but the shallow material deforms in a viscous fashion and does not store energy. During the megathrust earthquake, elastic rebound of the deeper crust induces tension in the shallow material, causing it to crack. If we assume that the observed crack distribution is controlled by the peak tension during the earthquake, it can be used to constrain how the megathrust rupture terminates in the deep end, which helps to understand the physics of earthquakes.

### 2.2.3. Introduction

Surface tension cracks have been widely observed in the coastal forearc of northern Chile – southern Peru (Baker et al., 2013; Loveless et al., 2016), where the Nazca plate is subducting beneath the South America plate producing  $M_w > 7$  megathrust earthquakes at century-scale intervals (Figure 2.1a). These cracks are particularly well preserved in cemented saline soils of the extremely arid Atacama Desert. They were generated by previous megathrust earthquakes, and some were newly created or reopened by the 1995  $M_w$  8.1 Antofagasta, 2007  $M_w$  7.7 Tocopilla, and 2014  $M_w$  8.1 Iquique (Pisagua) earthquakes (Baker et al., 2013; Scott et al., 2016; Loveless et al., 2005; 2016). Because they reflect broadly distributed permanent deformation, their association with earthquakes that are manifestations of elastic rebound is somewhat enigmatic.

Multiple factors may contribute to the coseismic formation of tension cracks. Margin-normal stretching exacerbated by a megathrust earthquake may cause permanent deformation dominated by normal faulting (Aron et al., 2013), but the observed are tension cracks limited to the top few meters. Gravitational collapse may occur during an earthquake where there is large topographic slope, but some of the cracks are in rather flat areas (Baker et al., 2013). Dynamic stressing by seismic shaking may generate some

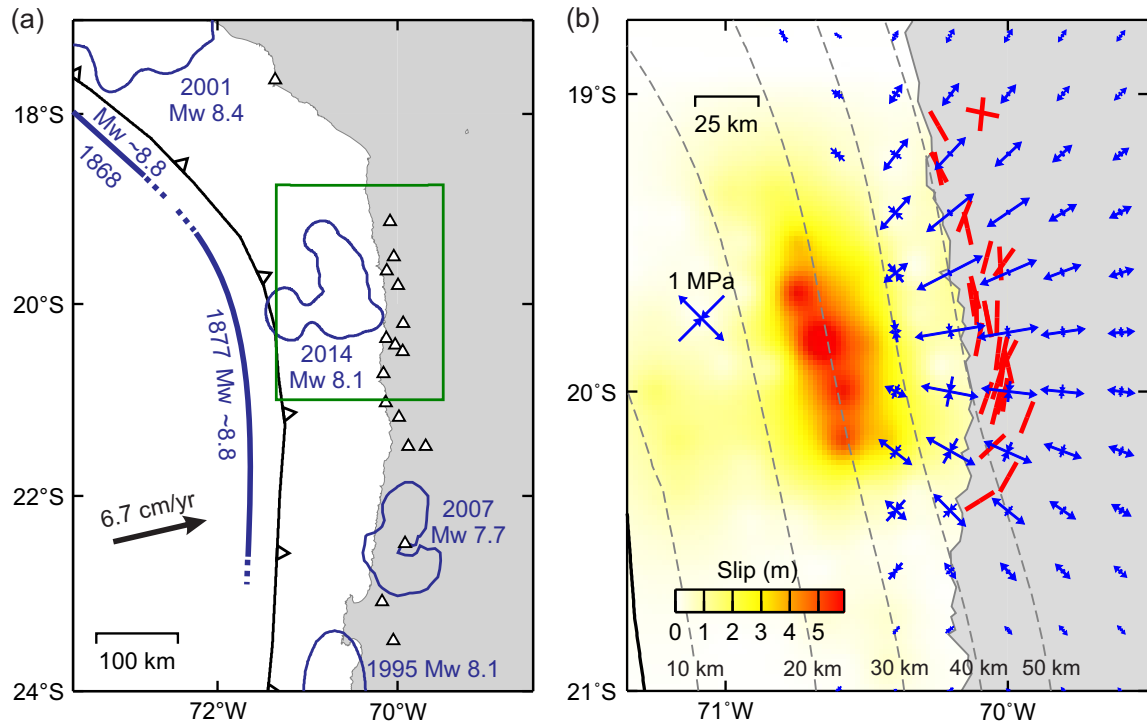


**Figure 2.1.** Reported surface cracks along the Chile–Peru forearc and association with megathrust rupture. (a) A regional view showing locations of surface crack observations (triangles) (Loveless et al., 2009), rupture zone of recent megathrust earthquakes (thin blue outlines), and the approximate along-strike extent of 1868 and 1877 events (trench-parallel thick blue line). The green box outlines the area shown in (b). (b) Smooth version of coseismic slip distribution of the 2014 Iquique earthquake reported by Gusman et al. (2015) and average orientations of surface tension cracks created or reopened by this earthquake at the shown locations (red bars) (Loveless et al., 2016; Scott et al., 2016). Diverging (converging) arrow pairs illustrate tensional (compressive) stress at surface induced by the coseismic slip, obtained using a 3D finite element model to be explained in Section 2.2.5.3.

surface cracks if there is local geometrical focusing of energy, but this cannot be the sole mechanism given the broad along-strike distribution and limited margin-normal distribution of the cracks (Scott et al., 2016). Because the observed cracks are located where coseismic tension is expected to be the largest and are oriented sub-perpendicular to the direction of tension (Figure 2.1b), static stress change during earthquakes must have played a dominant role (Baker et al., 2013). By assuming the spatial density of the cracks to be proportional to the magnitude of earthquake-induced static stress, Loveless et al. (2016) was actually able to invert the stress magnitude at multiple crack sites to infer the slip distribution of the 2014 Iquique earthquake.

In the absence of surface slope and in a purely elastic system, the energy released by an earthquake cannot exceed the strain energy that is available to cause the earthquake. In the interseismic period, megathrust locking causes elastic shortening of the forearc to accumulate energy. If all this energy is spent by a megathrust earthquake, the rock would return to a state of no shortening. Further stretching to cause permanent tensile failure would require more energy. Baker et al. (2013) reasoned that for the coseismic cracks to form, some permanent interseismic shortening is required. They also argued that the deeper crust may well be elastic throughout the earthquake cycles. Following this line of reasoning, we propose a testable model on the basis of recently reported observations in the petroleum engineering industry. In this model, the near-surface material undergoes viscoelastic relaxation thus permanent shortening (creep) during interseismic deformation but sufficient tension during an earthquake to cause tensile failure. At the crustal scale, the earthquakes still operate as elastic rebound.

## **2.2.4. Basic Concepts and Modelling Strategy**

### **2.2.4.1. Near-surface Viscoelasticity**

It is well known that the mantle's viscoelastic behaviour governs regional-scale crustal deformation in subduction earthquake cycles (Wang et al., 2012). It is less known that many shallow earth materials also exhibit viscoelasticity as demonstrated by studies of petroleum reservoir rocks (e.g., de Waal and Smits, 1988; Dudley et al., 1998; Hagin and Zoback, 2004a; Chang and Zoback, 2009; Sone and Zoback, 2013). In laboratory creep experiments on these reservoir rocks with a wide range of cementation and consolidation states, the samples continue to deform under constant stress due to time-dependent compaction. Since compaction is the dominant mechanism for such creep, porosity is a first-order control on the viscoelastic behaviour. As such, high-porosity (~30%) reservoir sands creep more than low-porosity (2-10%) shale gas reservoir rocks, by an order of magnitude or more, signifying the greater importance of viscoelastic deformation at shallower depths. These studies have also shown that creep strain can be described as a power-law function of time (Dudley et al., 1998; Hagin and Zoback, 2004b; Sone and Zoback, 2014). Unlike linear viscoelasticity, such power-law behaviour

exhibits a broad distribution of relaxation times (Findley et al., 1976; Dudley et al., 1998). For unconsolidated sands, the relaxation time could amount to hours to decades (Hagin and Zoback, 2004b). More recent laboratory experiments indicate that fractured basement rocks can exhibit similar creep behaviour due to shear-enhanced compaction facilitated by frictional sliding along randomly oriented microcracks (e.g., Sone & Condor, 2017). Weathering will enhance such behaviour, especially if clay minerals are created in the weathering process.

#### **2.2.4.2. Conceptual Model for Forearc Cracks**

The tension cracks in the Chile-Peru forearc are observed mostly in saline soils in the top few meters. They are also seen to extend into the bedrock, although it is difficult to tell how common because of limited exposure of suitable outcrops. The soils are dry, moderately or firmly cemented, and rich in gypsum and anhydrite (Erickson, 1981; Rech et al., 2003). The shallow bedrock is commonly pervasively fractured and weathered by salt wedging processes (R. W. Allmendinger, personal communication, 2019). Although no laboratory experiments have been conducted on these materials, we expect that they exhibit viscoelastic behaviour similar to the reservoir material and fractured rocks studied in the industry. If so, the near-surface compressive stress due to megathrust locking is being relaxed at the same time causing permanent shortening, while the deeper material is elastically shortened (Figure 2.2a). During a large megathrust earthquake, elastic rebound of the deeper material induces tensile stress near the surface. Because the near-surface material was relaxed prior to the earthquake, it experiences absolute tension as a result of coseismic deformation (Figure 2.2a), which may reach its tensile strength to generate mode-I cracks.

Stress changes due to an earthquake in both the near-surface and deeper materials are schematically illustrated in Figure 2.2b using the Griffith-Mohr-Coulomb failure criterion. The Andersonian stress condition assumed for this illustration is very reasonable for the flat shallow forearc areas some distance away from the megathrust rupture zone. The earthquake causes the horizontal stress  $\sigma_H$  to be less compressive in the deeper crust but changes it from being compressive or null to tensional and brings it to



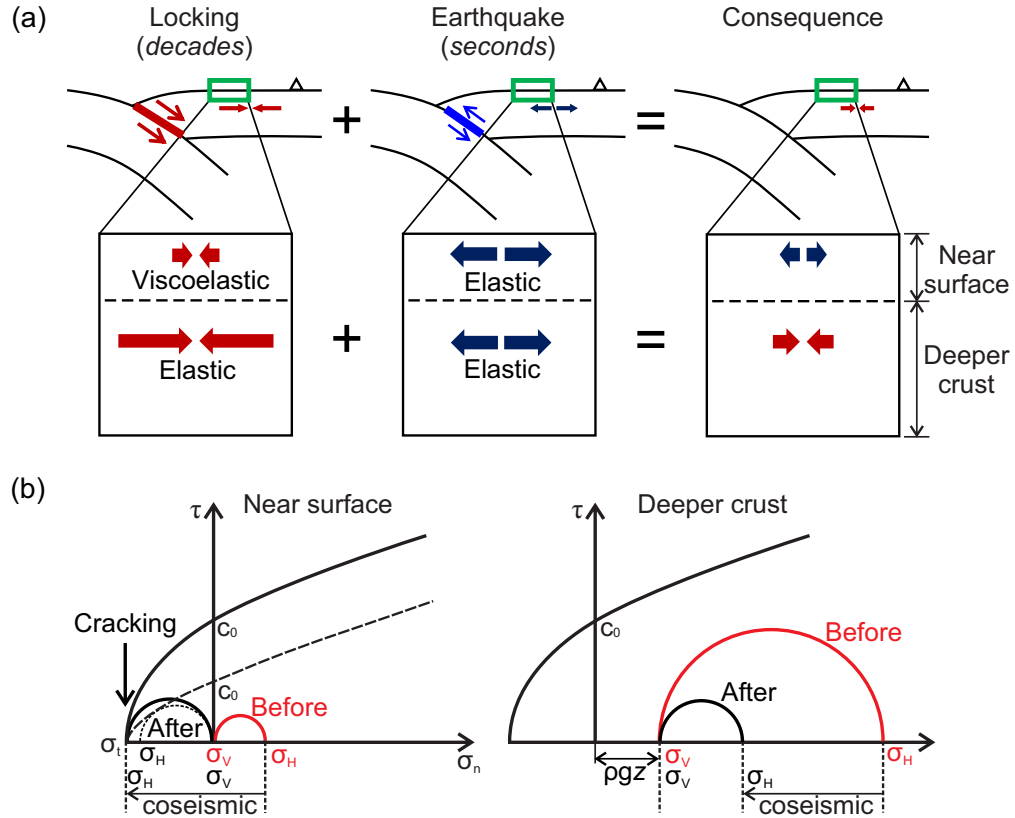


**Figure 2.2.** Conceptual model. During the interseismic period, stress is built up in the elastic deeper crust but not in the creeping viscoelastic near-surface material. During a megathrust earthquake, elastic rebound of the deeper crust induces tension in itself and in the near-surface material. As a consequence, the near-surface material is under tension after the earthquake. (b) Mohr-circle illustration of the state of stress in the near-surface and deeper parts of the crust in accordance with the conceptual model in (a). In the near-surface panel,  $\sigma_t$  and  $c_0$  are the tensile strength and cohesion of the near-surface material. The dashed yield envelope and Mohr circle show that shear failure may take precedence if  $c_0$  is too small.

tensile strength  $\sigma_t$  near the surface. Here we assume that the shallow material is adequately cohesive, consistent with the cemented state of the saline and gypsiferous soil hosting the cracks. If the cohesion ( $c_0$  in Figure 2.2b) is small, such as for the Coulomb failure criterion represented by the dashed line in Figure 2.2b, differential stress  $|\sigma_H - \sigma_V|$  may become large enough to cause shear failure (normal faulting) before  $\sigma_H$  reaches the level of  $\sigma_t$  thus pre-empting the formation of tension cracks. Mixed-mode cracking has been occasionally observed (Loveless et al., 2005) and may indicate locally low  $c_0$ .

### **2.2.4.3. Numerical Model**

We use finite element models to illustrate the proposed process. The model is constructed in accordance with the slab geometry in northern Chile – southern Peru (Hayes et al., 2012), such that the predicted stresses are comparable to the observed crack distribution. For simplicity, the rigidities of the upper plate, lower plate, and asthenospheric mantle are assumed to be 40, 48, and 64 GPa, respectively, and the Poisson's ratio is assumed to be uniformly 0.25. The model does not include gravity as a body force, although it does include the large-scale effect of gravity as a restoring force (Wang et al., 2012). Other technical details of the modelling are very similar to those in Sun and Wang (2015). We first use a plane-strain two-dimensional (2-D) model to illustrate the basic concepts and then use a three-dimensional (3-D) model to simulate static stress induced by a real earthquake.

The key element of the proposed process is viscoelastic relaxation (creep) of near-surface material over the interseismic period, including both the saline soil and the top part of the underlying weathered bedrock. To focus on this key element, we invoke a veneer of Maxwell viscoelastic material along the top of the overriding plate in an otherwise purely elastic subduction zone earthquake model. The thickness and viscosity of the top layer are assumed to be 10 m and  $10^{19}$  Pa s, respectively. With a rigidity of 40 or 20 GPa, its Maxwell relaxation time is about 8 or 16 years, comparable to the timescale of the relaxation of some of the reservoir materials inferred from laboratory experiments and field data (Hagin and Zoback, 2004b). Obviously, the exact thickness and relaxation time of the near-surface material and whether the viscoelasticity is linear or nonlinear are unimportant, as long as significant relaxation takes place within a fraction of the recurrence interval of megathrust earthquakes. For example, a viscosity of  $10^{18}$  Pa s will yield nearly identical results.

## **2.2.5. Model Results**

### **2.2.5.1. Reference Model**

The results of our 2D reference model are summarized in Figure 2.3, with a fuller cross-section view illustrated in Figure 2.5. In this model, the elastic upper plate has accumulated several megapascals (MPa) of compressive  $\sigma_H$  before the earthquake (Figure 2.3a, 15 m depth), accomplished by locking the megathrust for 100 years, with the accrued slip deficit shown in Figure 2.3b. However, because of viscoelastic relaxation,  $\sigma_H$  in the surface layer is close to 0 (Figure 2.3a, 5 m depth). It is not exactly zero because (1) there is still ongoing shortening due to plate convergence, and (2) we have added lithostatic pressure before plotting the results. To simulate earthquake-induced stress, we prescribe a bell-shaped coseismic slip distribution using a slip function given in Wang et al. (2013). With a peak slip value of 5 m (Figure 2.3b), this represents an  $M_w \sim 8.1$  earthquake if the strike length of the rupture is 150 km.

The model earthquake induces incremental tension throughout the upper plate landward of the peak slip (Figure 2.3c). Nearly identical tension is induced near the surface and deeper in the crust, but it results in contrasting stresses after the earthquake because of their different pre-earthquake stresses (Figure 2.3a). After the earthquake, the deeper crust (15 m) is still in compression, but the surface layer is under tension in two areas, with one of them coinciding with where the tension cracks would be distributed in the Chile-Peru forearc (Figure 2.3a). An expanded view of the area of interest is shown in Figure 2.3d. Note that both the before- and after-earthquake stresses shown in Figures 2.3a and 3d include lithostatic pressure. Here we do not scrutinize the stress distribution offshore around the rupture zone, because it depends sensitively on the details of coseismic slip that the model is not designed to portray, and there is currently no information regarding the presence or absence of similar tension cracks offshore.

The model shown in Figures 2.3 and 2.5 is purposely designed to be very simple, but it explains the most important aspect of the proposed process. A few additional points are worth mentioning. (1) The model does not directly include plastic yielding, but it demonstrates that large enough tension can be induced by an earthquake to generate the surface cracks in the right area. Tensile stress of 1 – 2 MPa (Figure 2.3d) exceeds the tensile strength of cemented soils and can cause mode-I cracking as shown in Figure 2.2b. (2) The proposed mechanism does not exclude additional dynamic forcing by passing-by seismic waves which may also contribute to the generation of the cracks

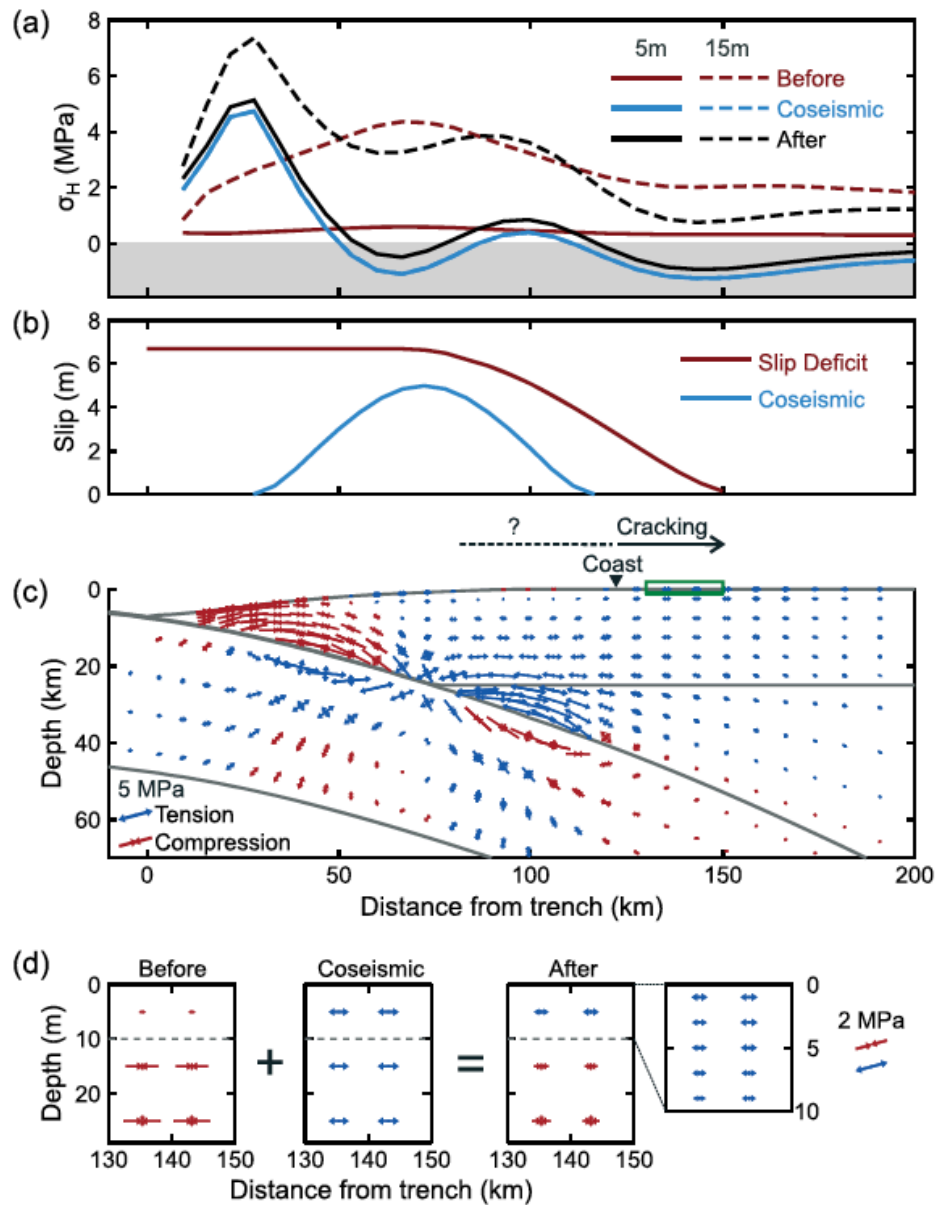


**Figure 2.3.** The 2D reference model. Horizontal stress  $\sigma_H$  near the surface (5 m depth) and deeper crust (15 m) (tension shaded). The earthquake-induced stress (Coseismic) is the same at both depths. (b) Slip deficit before the earthquake responsible for the before-earthquake stress and coseismic slip responsible for the earthquake-induced stress. (c) Cross section view of earthquake-induced stress. Those before and after the earthquake are shown in Figure 2.5. The green box marks the region shown in (d). Dashed line and question mark signify lack of knowledge of the presence and distribution of cracks offshore. (d) Expanded view of the green box area in (c), showing near-surface tension after the earthquake. For stresses before and after the earthquake in (a) and (d), lithostatic stress is included assuming rock density of 2500 kg/m<sup>3</sup> and gravity 9.8 m/s<sup>2</sup>.

(Baker et al., 2013). (3) Viscous creep (relaxation) of reservoir rocks includes a volumetric component (Dudley et al., 1998; Hagin and Zoback, 2004a; Sone and Zoback, 2013), but in our simplified model, as in nearly all viscoelastic models in geodynamics, the creep occurs only as shear strain. The neglect of the volumetric creep in no way hinders the illustration of the main physical process. (4) The model simulates the stresses associated with subduction earthquake cycles, ignoring the background tectonic stress. In subduction zone forearcs, the tectonic stress is very low (e.g., Wang et al., 2019). Near the surface, because of viscoelastic relaxation, the tectonic stress is even less important. (5) Mantle viscoelasticity is not included in the reference model. If we use a more realistic subduction earthquake cycle model (Figure 2.6) in which the upper mantle has a bi-viscous transient viscoelastic rheology similar to that of Wang et al. (2012), the results in our region of interest are only slightly modified but still demonstrate the same fundamental process (Figure 2.7).

#### **2.2.5.2. Testing the Role of Downdip Rupture Termination**

The location and abruptness of the downdip termination of coseismic slip exerts primary control on the location of peak surface tension induced in the coastal forearc by the earthquake. Assuming the peak tension controls the occurrence of the cracks, we explore the effects of the rupture termination using two sets of 2-D models and comparing their results with the reference model (Figure 2.4).

It is important to emphasize the similarity between the earthquake-induced stress (at both shallow and deeper depths) and the after-earthquake stress near the surface (Figures 2.3a and 3d). The similarity occurs if the near-surface stress has been relaxed to nearly zero before the earthquake. It justifies the practice of directly comparing the earthquake-induced stress with the observed cracks, even if the former is obtained with a purely elastic model (Loveless et al., 2016). Otherwise such a direct comparison would be invalid. Here and in Section 2.2.5.3, we make this direct comparison. Because we are only examining coseismic stress, the presence or absence of the viscoelastic shallow layer and the process of interseismic stress buildup are computationally irrelevant. For both test sets, the downdip limit of rupture termination is represented by a spatial range defined by

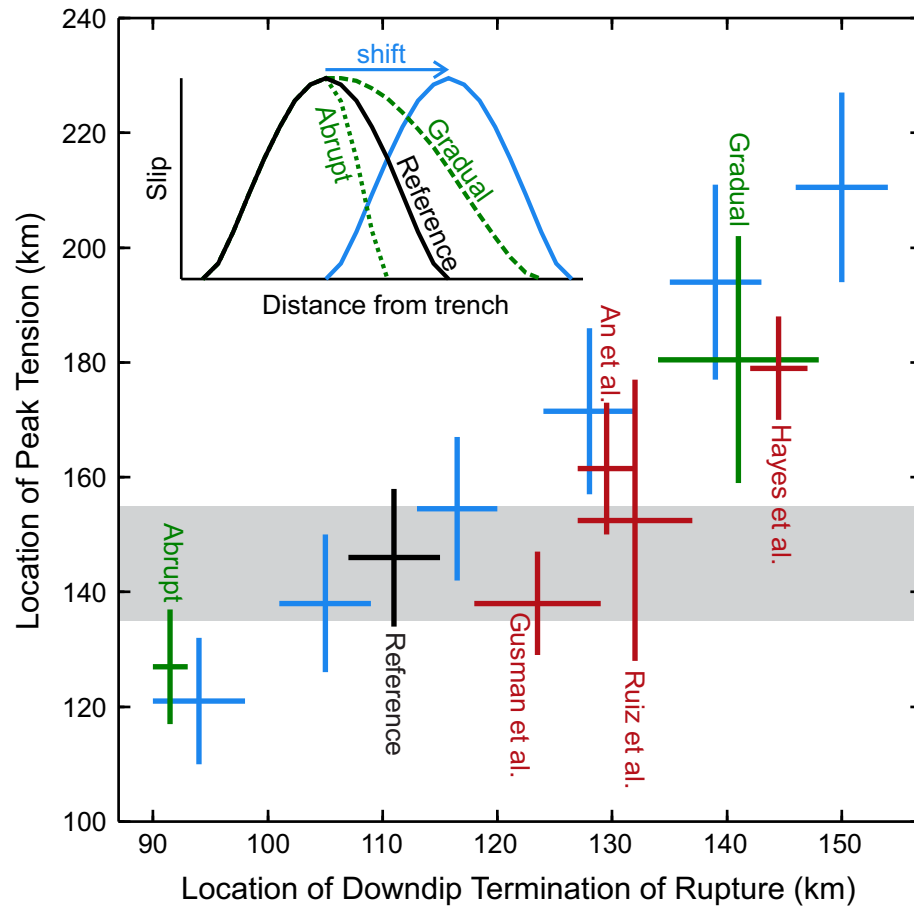


**Figure 2.4.** Controlling effects of downdip rupture termination. The grey-shaded area approximately represents the observed span of crack distribution. The zone of peak tension is defined as the area where earthquake-induced  $\sigma_H$  at 5 m depth is between 90% and 100% of the peak value in coastal forearc. Details of the 2-D reference model (black) are shown in Figure 2.3. The effects of the location (blue) and abruptness (green) of the downdip rupture termination are shown with 2D model results. For 2-D models, rupture termination is shown using the spatial range where coseismic slip is 0–1 m. For the four published rupture models for the 2014 Iquique earthquake (red), the models are 3-D, the values shown are derived along a profile crossing the rupture zone (Figure 2.8), and rupture termination is shown using the spatial range where coseismic slip is 0.5–1 m (Figure 2.9).

the location where the model coseismic slip is 0–1 m, and the zone of peak tension is defined as the surface land area where horizontal tensile stress at 5 m depth is 90–100% of the peak tension (minimum  $\sigma_H$  in Figure 2.3a).

In one test set, we shift the megathrust rupture in the dip direction without changing

its shape (Figure 2.4, inset). A deeper rupture causes the zone of peak tension to be farther landward and generally more broadly distributed (Figure 2.4, blue bars). In these 2D models, if the rupture is terminated less than 100 km or greater than 120 km from the trench, the predicted zone of peak tension will not be compatible with the observed cracks. In the other test set, we change the gradient of the slip decrease by uniformly scaling the deeper half of the bell-shaped slip distribution of the reference model (Figure 2.4 inset). If the slip decrease is too abrupt or too gradual, the predicted zone of peak tension is not compatible with the observed cracks (Figure 2.4, green bars). There is some trade-off between the effects of the location and abruptness of the rupture termination, but the results in Figure 2.4 adequately demonstrate what the observed crack distribution may tell us about the downdip dimension of megathrust rupture.

### 2.2.5.3. Application to the 2014 Iquique Earthquake

Finally, we apply the model to the 2014  $M_w$  8.1 Iquique megathrust earthquake using a 3-D model. In terms of structure, the 3-D model is a simple expansion of the 2-D model in the strike direction except for minor along-strike variations in slab geometry (Hayes et al., 2012). A number of rupture models for this event have been derived by different research groups by inverting geodetic, seismological, and tsunami data (An et al., 2015; Bai et al., 2014; Duputel et al., 2015; Gusman et al., 2015; Hayes et al., 2014; Jara et al., 2018; Lay et al., 2014; Liu et al., 2015; Ruiz et al., 2014; Schurr et al. 2015; Yagi et al., 2014). Some of these models assume a piecewise planar fault. We map their slip distributions to our curved megathrust following the procedure described in Brown et al. (2015). Some of the models, especially those that included tsunami data in the inversion (e.g., An et al., 2014; Gusman et al., 2015), feature rather large (e.g., 20 km  $\times$  20 km) uniform-slip planar sub-faults, and we interpolate the sub-fault values to derive a smooth version of their slip distributions to be imported into our model. The interpolated slip distribution of Gusman et al. (2015) is already shown in Figure 2.1b, together with the incremental stress induced by it as predicted with our 3D model. In Figure 2.8, we also show seven other published slip distributions with model-predicted stresses. This representative selection serves to reflect the similarities and differences between different rupture models for this event.

All the published rupture models fit the specific data that had been used to derive them, but they differ in rupture location or abruptness of termination and therefore lead to different locations of the zone of peak tension. In Figure 2.4 (red bars), for four of the slip distributions, we show the location of rupture termination and model-predicted zone of peak tension along a profile through the peak slip zone and oriented roughly in the direction of maximum induced tension in the coastal area (Figure 2.8). Again, we directly compare the earthquake-induced stress with crack observations (Figure 2.4). Here rupture termination is defined by the spatial range over which coseismic slip is 0.5–1 m; slip values < 0.5 m are likely within errors, and zero slip cannot be meaningfully defined (Figure 2.9b). The definition of the zone of peak tension is the same as for the 2-D models, except that  $\sigma_H$  is measured along the profile (Figure 2.9a).

Figures 2.4 and 2.8 indicate that the observed tension cracks contain important information on the nature of the megathrust rupture. Rupture models that have the peak slip area located too far south yield stress predictions less consistent with crack orientations in the south (Figure 2.8), demonstrating that the along-strike distribution of cracking can also provide information about the details of the rupture. Rupture models that have a shallower slip termination, more consistent with what Loveless et al. (2016) directly inferred from the crack observations, tend to agree better with the crack distribution (Figure 2.4). Some of the models do not feature prominent local peak tension landward of the rupture zone but mostly a monotonic landward decrease, likely because the rupture termination is too gradual (Figure 2.9), and hence are not included in Figure 2.4. The abruptness of rupture termination may help us better understand rupture dynamics and is worth further investigation.

### 2.2.6. Conclusions

To explain how coseismic static stress may have induced surface tension cracks in the Chile-Peru coastal forearc, we proposed a model of shallow viscoelastic relaxation by drawing analogy with reservoir rocks observed in engineering laboratory experiments. The model is testable by conducting similar experiments on the materials hosting the cracks. The model can be revised or improved if offshore observations of the presence or



absence of similar cracks become available. From our modelling and discussion, we draw the following conclusions.

1. If a surface viscoelastic layer relaxes in the interseismic period, it undergoes coseismic tension because of the rebound of the elastic deeper crust, regardless of the thickness of the layer and details of the viscoelastic rheology.
2. Because of the very low pre-earthquake near-surface stress, earthquake-induced tension is similar to absolute tension, causing permanent failure. This similarity enables an otherwise invalid direct comparison of the earthquake-induced stress with observed cracks, even if the stress is calculated using a purely elastic model.
3. If the crack distribution is assumed to reflect the zone of peak coseismic tension, it contains important information on megathrust rupture. A deeper rupture with a gradual termination causes the zone of peak tension to be farther inland and more broadly distributed, and vice versa. For the 2014  $M_w$  8.1 Iquique earthquake, some of the published rupture models are more consistent than others with observed crack distribution.
4. For tensile cracking to be the main mode of permanent failure under coseismic tension, the near-surface material must be adequately cohesive. Otherwise, shear failure may take precedence.

#### **2.2.7. Acknowledgements**

Reviews by R. W. Allmendinger and J. P. Loveless improved the paper. No samples are used in this work. The crack distribution data shown in Figure 2.1b and used in other figures are from online Supporting Information of Loveless et al. (2016). H. L. was supported by a Bob Wright Graduate Scholarship, a Jarmila Vlasta Von Drak Thouvenelle Graduate Scholarship, University of Victoria Fellowships and Graduate Awards, and a Discovery Grant to K. W. from the Natural Sciences and Engineering Research Council of Canada.

### 2.3. Supporting Information

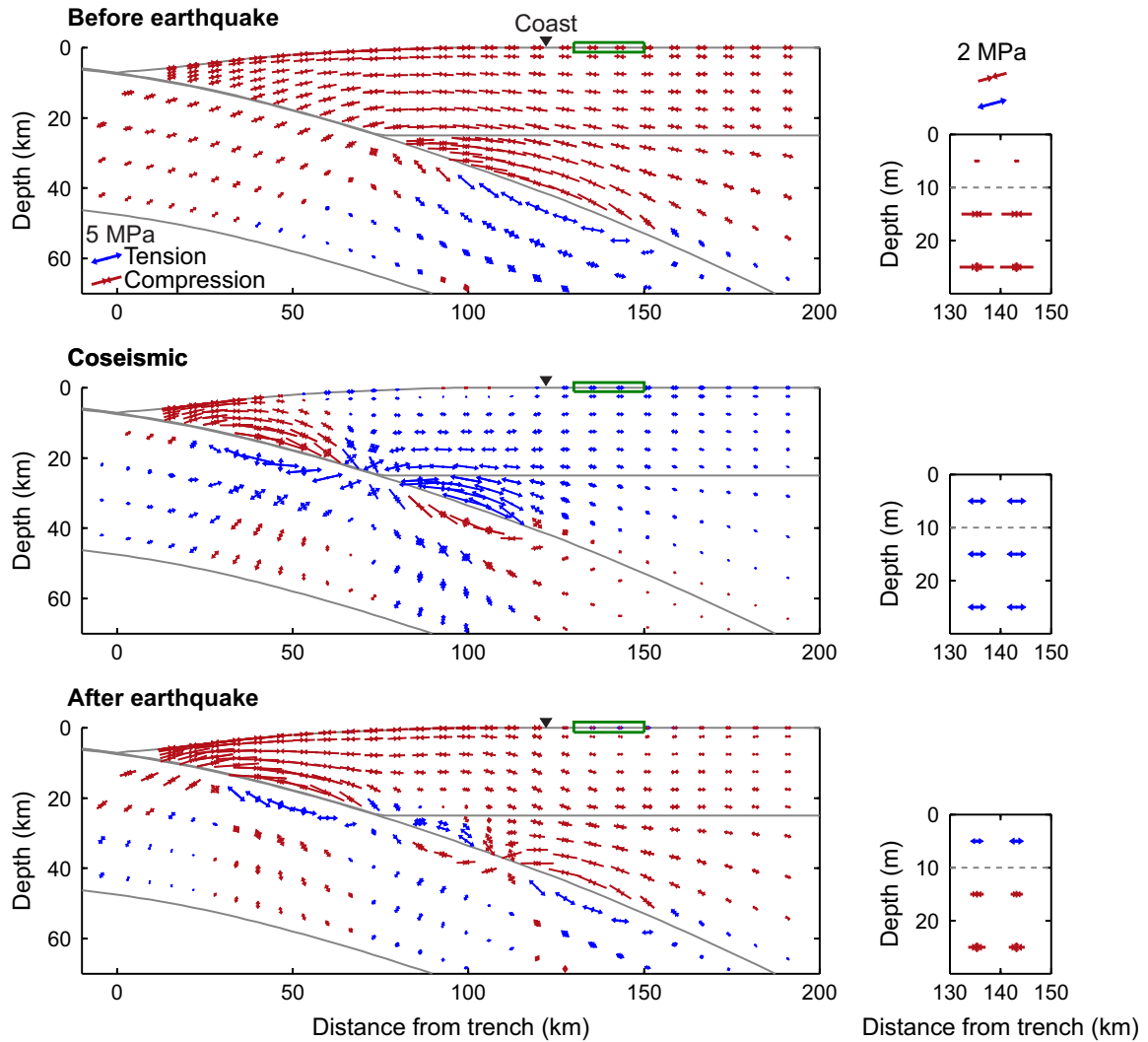


**Figure 2.5.** Cross-section view of the reference 2-D model of stress change summarized in Figure 2.3. The model is elastic except for the 10 m thick viscoelastic layer along the top of the upper plate. Model parameters are explained in Section 2.2.4.3. The “Coseismic” panel shows the stress induced by the earthquake and is the same as in Figure 2.3c. The “After earthquake” results are the combination of the “Before earthquake” and “Coseismic” results. In each panel, the area marked by the green box is shown to the right in expanded view. In the expanded view, lithostatic stress has been added to the stresses before and after the earthquake assuming rock density  $2.5 \text{ g/cm}^3$  and gravity  $9.8 \text{ m/s}^2$ .

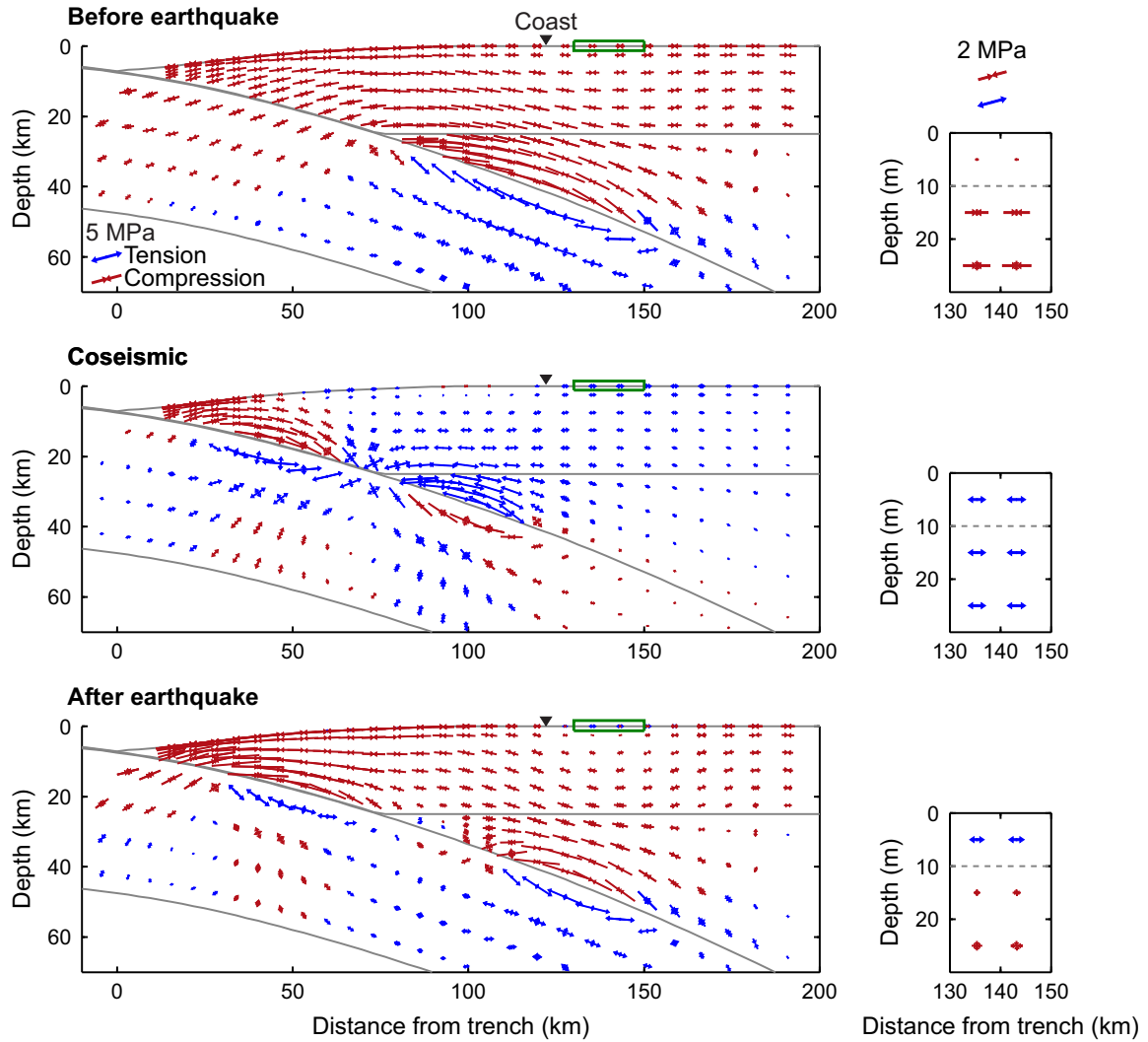


**Figure 2.6.** Similar to Figure 2.5 but for a model in which the mantle exhibits bi-viscous transient viscoelastic rheology similar to Wang et al. (2012). For the mantle wedge, the Kelvin component has a viscosity of  $10^{18}$  Pa s and rigidity of 48 GPa, and the Maxwell component has a viscosity of  $10^{19}$  Pa s and rigidity of 64 GPa. In the oceanic mantle, the rigidity values are the same as in the mantle wedge, but the viscosity values are one order of magnitude higher.

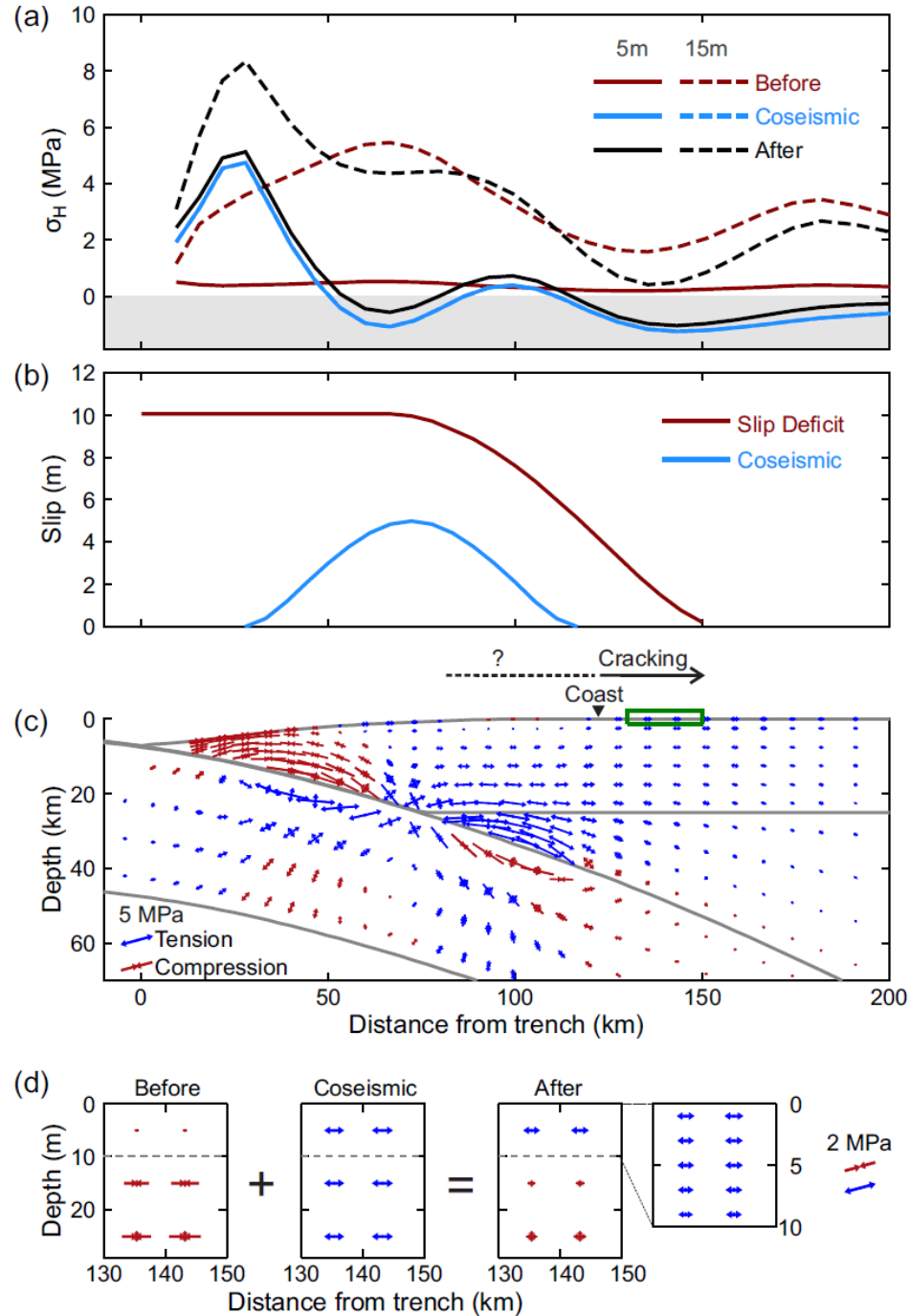


**Figure 2.7.** Similar to Figure 2.3 but for the model shown in Figure 2.6. In a 2-D model with a viscoelastic mantle, loading the coastal forearc to the same pre-earthquake stress as in the elastic model requires a greater slip deficit along the megathrust. Local balance of slip budget would require multiple earthquake cycles and along-strike variations in locking and creep behaviour.

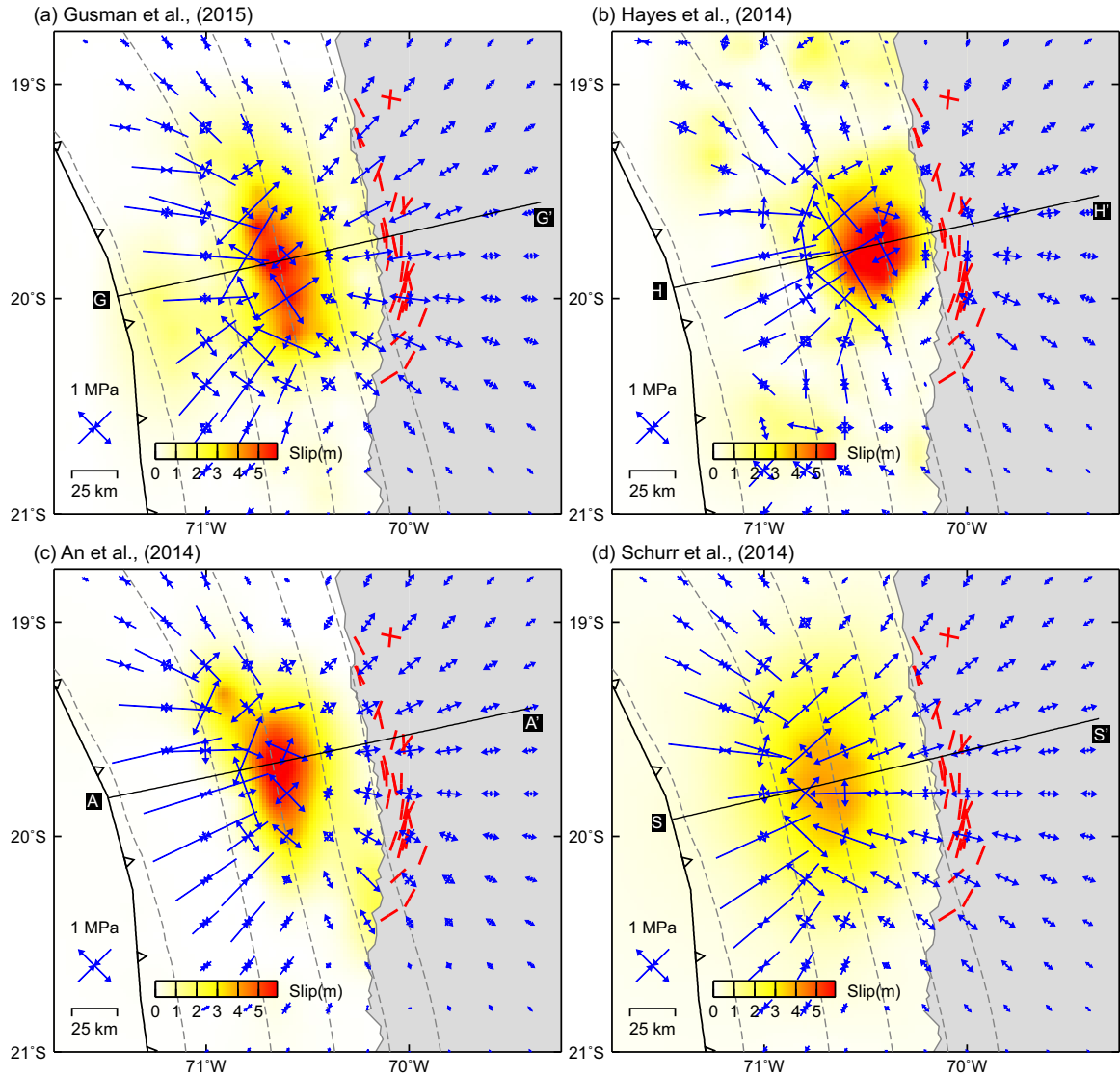


**Figure 2.8.** Coseismic slip of the 2014 Iquique earthquake and surface stresses induced by it. The publication that reported the shown slip distribution is shown at the top of each panel. A diverging (converging) arrow pair illustrates tensional (compressive) stress at the surface induced by the coseismic slip, obtained using the 3D finite element model explained in Section 2.2.4.3. Red bars show the average orientation of surface tension cracks created or reopened by this earthquake at the shown locations (Loveless et al., 2016). Slip distribution and stresses along the profile crossing the rupture area are shown in Figure 2.9.

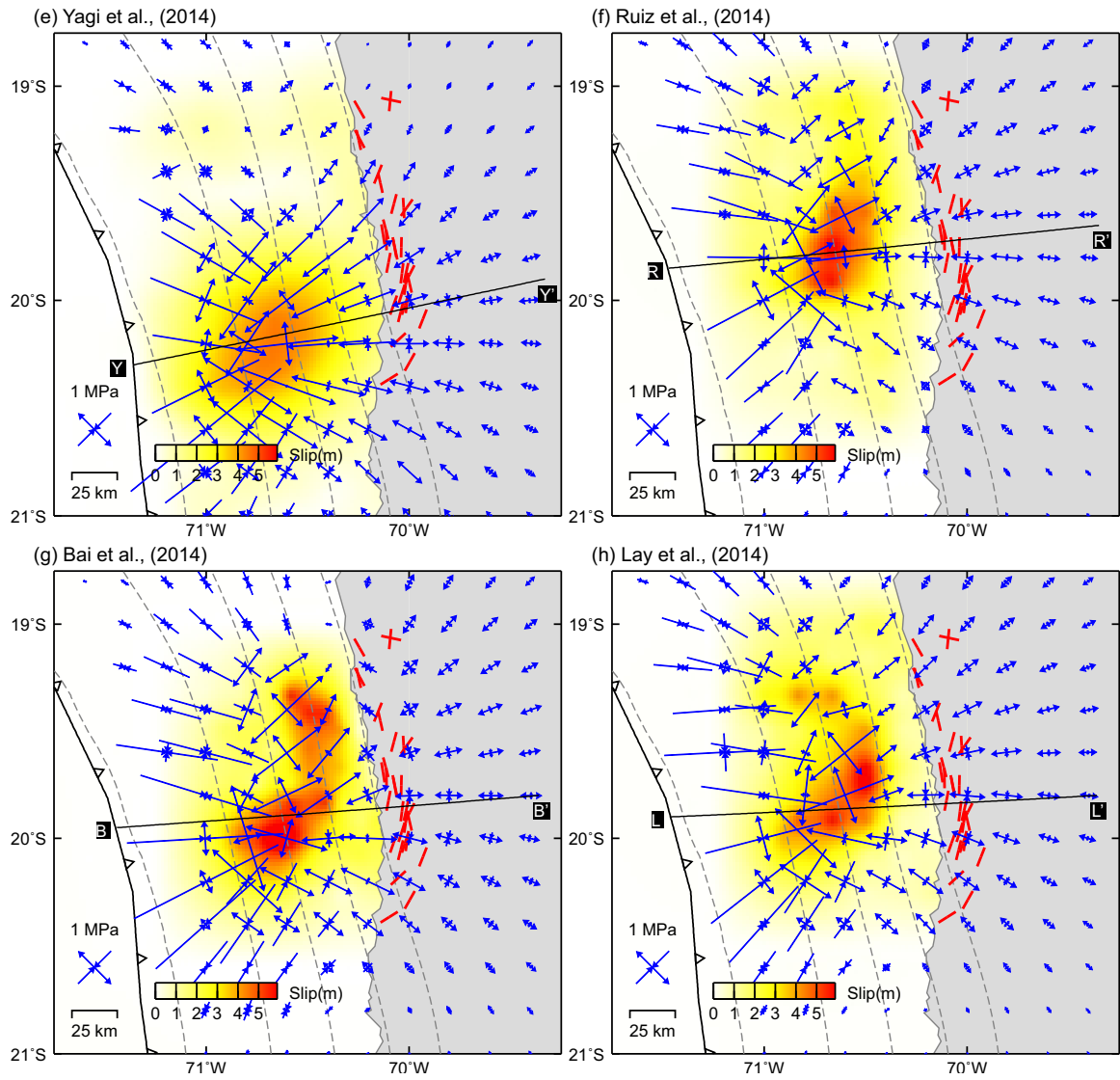


**Figure 2.8.** (Continued from last page)

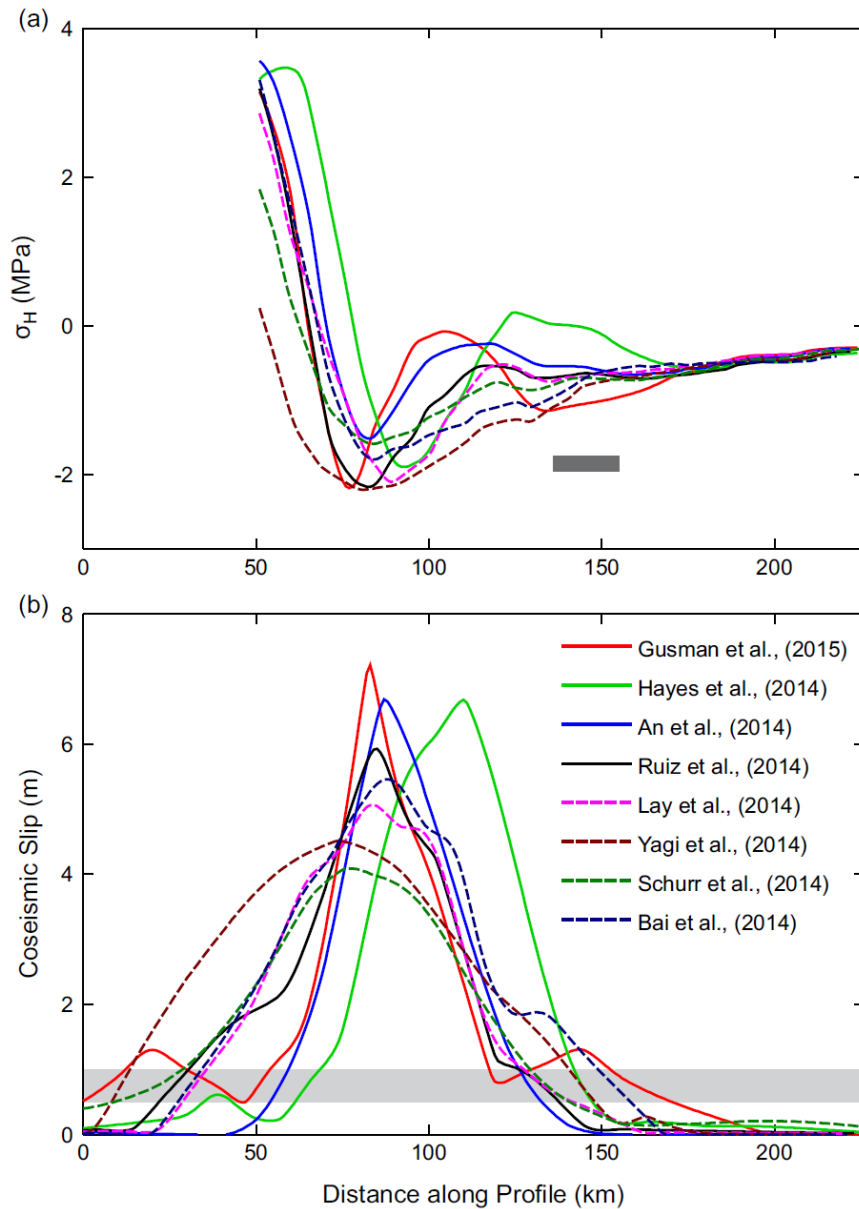


**Figure 2.9.** Megathrust slip and crustal stress along the profile shown in Figure 2.8 for each of the eight rupture models. (a) Horizontal stress  $\sigma_H$  along the profile. The area of observed tension cracks is approximately represented using a grey bar. (b) Slip distribution along the megathrust imported or interpolated from the shown references. Downdip rupture termination is defined using the spatial range where slip is 0.5–1 m (grey area). Models shown with solid lines are included in Figure 2.4.

## **Chapter 3. Postseismic uplift near the volcanic arc as a geodetic signature of cold mantle wedge corner**

This chapter explains what has been learned about subduction zone rheology from observations of postseismic vertical deformation just seaward of the volcanic arc. The main body of this chapter consists of a published journal article [Luo and Wang, 2021]. The chapter consists of three sections, with Section 3.1 describing basic information of the article, Section 3.2 presenting the article itself, and Section 3.3 providing the Extended Data accompanying the published article.

### **3.1. Article Information**

#### **3.1.1. Author and Coauthor Contributions**

The author of this dissertation H.L. made the reported discovery, carried out data synthesis and analyses, and conducted the numerical modelling. H.L. and coauthor K.W. together wrote the paper.

#### **3.1.2. Citation**

Luo, H., & Wang, K. (2021). Postseismic geodetic signature of cold forearc mantle in subduction zones. *Nature Geoscience*, 14(2), 104-109. doi: 10.1038/s41561-020-00679-9.

#### **3.1.3. Author's Names and Affiliations**

Haipeng Luo<sup>1</sup> and Kelin Wang<sup>2,1</sup>

<sup>1</sup>School of Earth and Ocean Sciences, University of Victoria, Victoria, British Columbia, Canada

<sup>2</sup>Pacific Geoscience Centre, Geological Survey of Canada, 9860 West Saanich Road, Sidney, British Columbia, Canada

Corresponding authors:

Haipeng Luo (hpluo@uvic.ca), Kelin Wang (kelin.wang@canada.ca)



### 3.1.4. Article Format

The text and figures included in Section 3.2 are taken directly from the Nature Geoscience article. The Extended Data for the article is given in Section 3.3. Sections, figures in the original article have been renumbered to be compatible with the chapter format of the dissertation. The width of the two tables in the Extended Data of the original publication exceeded the page width of the dissertation. In order to meet the dissertation format requirement, here each of the two tables is separated into parts A and B sharing the same first column. References cited in the article are included in the bibliography of the dissertation.

## 3.2. Postseismic geodetic signature of cold forearc mantle in subduction zones

### 3.2.1. Abstract

A sharp thermal contrast between the cold forearc and the hot arc and backarc is considered fundamental to various subduction-zone processes. However, direct observational evidence for this contrast is rather limited. If this contrast is present, it must cause a rheological contrast in the mantle wedge: elastic in the forearc and viscoelastic in the arc and backarc for the timescale of earthquake cycles. Here we demonstrate that postseismic deformation following large subduction earthquakes provides independent evidence for the thermally controlled rheological contrast. Specifically, we show that seaward postseismic motion is deflected upward at the edge of the cold forearc mantle wedge, causing diagnostic uplift just seaward of the volcanic arc. From numerical simulations of postseismic deformation following the 2011 moment magnitude ( $M_w$ ) 9 Tohoku-oki, 2010  $M_w$  8.8 Maule, 2007  $M_w$  8.4 Bengkulu and 1960  $M_w$  9.5 Chile earthquakes, together with a global synthesis of postseismic uplift measurements, we find that cold forearc mantle is present irrespective of the diversity in tectonic settings. Our findings also indicate that field surveys eight years after the 1960 Chile earthquake provided some of the earliest evidence for viscoelastic postseismic deformation. We suggest that the established link between long-term thermal processes and short-term earthquake cycle deformation is important to understanding subduction-zone dynamics.

### 3.2.2. Introduction

A thermal contrast between the cold forearc and the hot arc and backarc is considered fundamental to subduction-zone dynamics (Wada and Wang, 2009; Syracuse et al., 2010). The contrast reflects a downdip transition of kinematic coupling along the subduction interface (Wada and Wang, 2009). Shallower than 70–80 km depths, mantle-wedge material does not travel with the subducting slab (decoupled). Farther downdip, mantle material travels with the slab at the subduction rate (coupled) (Figure 3.1a). The shallow decoupling results in a stagnant and cold mantle-wedge corner referred to as the ‘cold nose’ that provides a condition for the formation of serpentine and other hydrous minerals by incorporating aqueous fluids from the dehydrating subducting slab (Hyndman and Peacock, 2003; Krawczyk et al., 2006). The deep coupling results in viscous mantle-wedge flow to supply heat for melt generation and arc volcanism (Agard et al., 2018; Figure 3.1a). The decoupling–coupling transition and the associated thermal contrast is also inferred to govern the evolution of the subduction interface in the dip direction (Gao and Wang, 2017; Barbot, 2020). The coldest shallow part of the decoupled interface hosts great megathrust earthquakes. Along the coupled interface beneath the hot arc and backarc, the interface becomes a broad zone of viscous shear and does not host earthquakes (Wada and Wang, 2009).

However, despite the geodynamic importance of the thermal contrast, observational evidence is limited. The most direct evidence is forearc heat-flow measurements (e.g., Furukawa, 1993; Lewis et al., 1988; von Herzen et al., 2001), but very few subduction zones have adequate heat-flow coverage (Wada and Wang, 2009). Even for one of the best-studied subduction zones, the Japan Trench, uncertainties in heat-flow observations can allow arguments against the presence of the cold nose (Horiuchi and Iwamori, 2016). Indirect evidence for the cold nose includes low seismic attenuation (high seismic quality factor ( $Q$ )) (e.g., Tsumura et al., 2000; Wang, Z., et al., 2017; Wei and Wiens, 2018) and geophysical imaging from a few relatively warm subduction zones supporting the presence of serpentinization (e.g., Bostock et al., 2002; Abers et al., 2017), but the coverage and resolution of the geophysical data are both limited. In this work, we present unique evidence using what may seem to be unrelated observations: geodetic measurements of vertical postseismic deformation following great subduction

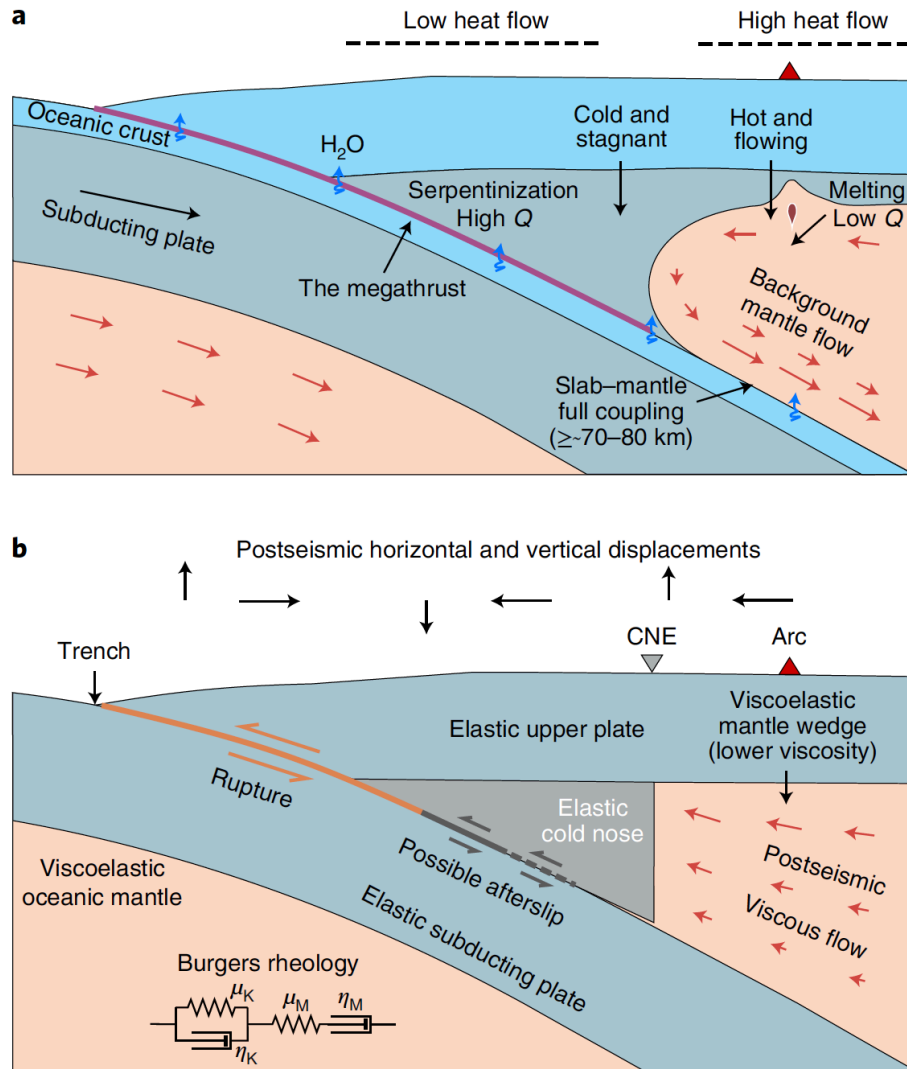


**Figure 3.1.** Schematic illustration of thermal and rheological structure in subduction zones. (a) Thermal structure. The sharp contrast between cold forearc and hot arc–backarc is inferred from limited heat-flow data and seismic attenuation (high or low  $Q$ ). (b) Rheological structure. The cold nose exhibits elastic behaviour in earthquake cycles.  $\eta$  and  $\mu$  are viscosity and rigidity, respectively, and subscripts M and K denote Maxwell and Kelvin, respectively. The postseismic viscous flow in (b) is induced by megathrust rupture, but the background mantle flow in (a) is driven by the subducting plate.

earthquakes. The key point is that the thermal contrast, if present, must lead to a rheological contrast affecting postseismic deformation in a viscoelastic Earth (Figure 3.1b). The cold nose should have a very high viscosity and behave elastically in megathrust earthquake cycles. The hot arc and backarc should have a much lower viscosity and feature fast viscoelastic relaxation.

### 3.2.3. Postseismic uplift due to viscoelastic stress relaxation

Before we lay out geodetic evidence for this process, we first explain the mechanism using a simple two-dimensional (2D) finite-element model of postseismic deformation with a rheological structure similar to that in Figure 3.1b. The modelling strategy and the choice of parameters are similar to previous subduction-zone postseismic deformation models (Wang et al., 2012; Sun et al., 2014; 2018), and details are given in Methods. Two of the three models summarized in Figure 3.2a do not have an elastic cold nose, but the other one does as shown in Figure 3.2b. The three models all show that postseismic stress relaxation gives rise to a seaward viscous flow in the mantle wedge (Figure 3.2b) and a landward flow in the oceanic mantle (not displayed). Note that this postseismic viscous flow is a perturbation field added to, and not to be confused with, the long-term background mantle flow (Figure 3.1a). The postseismic mantle flow leads to an opposing motion of the near-trench area and the area farther landward (Figure 3.2a, b), which has been emphasized in previous models (Sun et al., 2014; 2018; Freed et al., 2017). But the horizontal deformation is insensitive to the rheological contrast (Figure 3.2a), although the absence of the cold nose would necessitate the use of a higher mantle-wedge viscosity to produce similar horizontal velocities.

By contrast, the short-term vertical deformation is strongly affected by the rheological contrast (Figure 3.2a). Without the cold nose, the model predicts no or little uplift landward of the rupture zone. With the cold nose, there is uplift around its landward edge with a rate observable with geodetic measurements. The reason for the strong signature of the rheological contrast in the uplift pattern is that the postseismic seaward motion of the mantle wedge and upper plate is deflected upwards upon encountering the elastic cold nose (Figure 3.2b). An enlarged view in Figure 3.2c shows the absence of this deflection in models that do not include the cold nose. As shown by a suite of sensitivity tests (Figure 3.2d), the wavelength of the uplift zone and the location of the peak uplift are controlled by the size of the cold nose. If the cold-nose edge (CNE) extends farther landward, the zone of uplift is also farther landward and is broader.

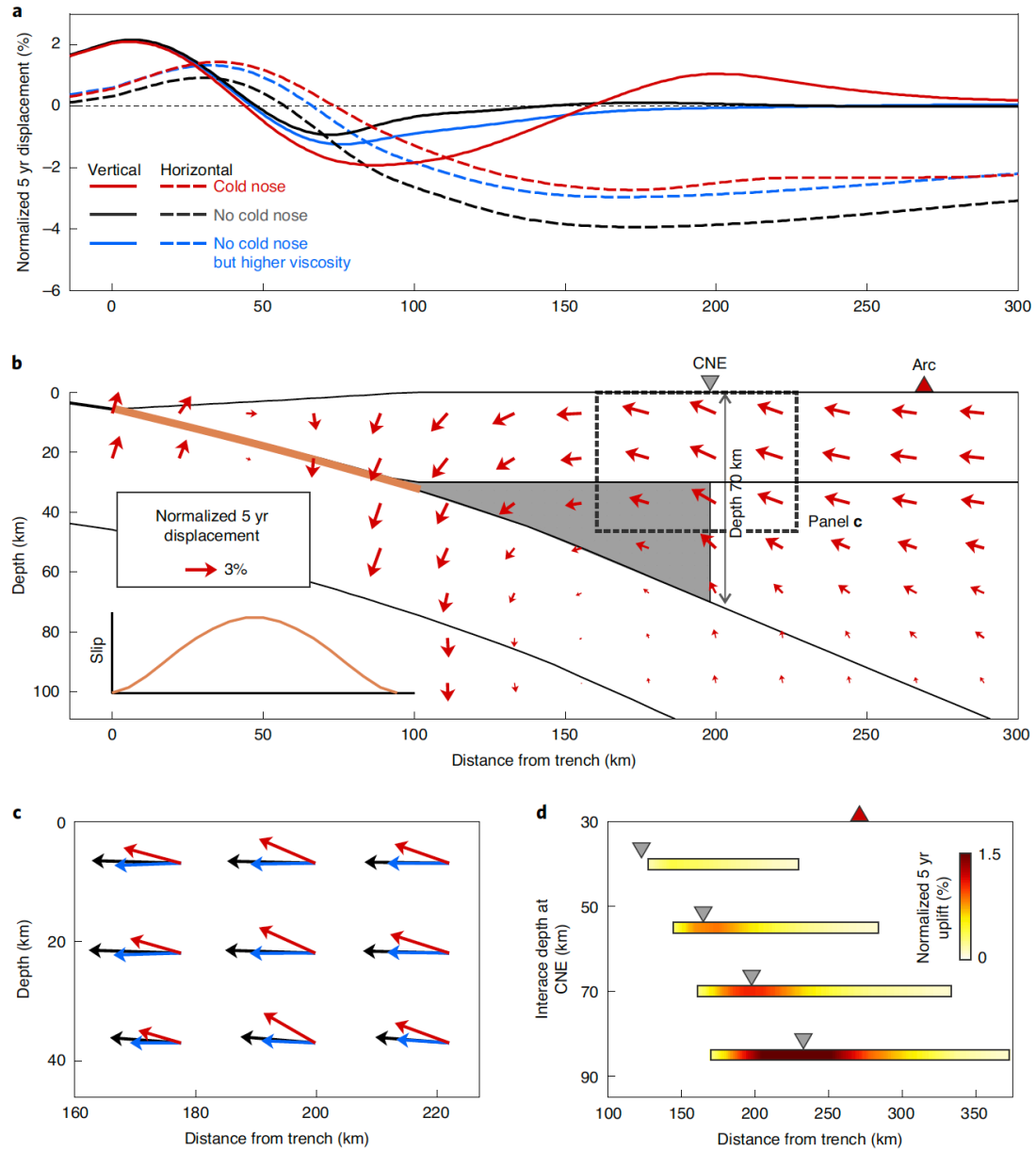


**Figure 3.2.** 2D models of postseismic deformation to illustrate the physical process discussed in this paper. (a) Vertical and horizontal postseismic displacements (normalized by peak coseismic slip value) five years after an earthquake for three models. Only the model including an elastic cold nose features pronounced uplift around the CNE. (b) Cross-section view of postseismic displacement field of the cold-nose model. The postseismic motion is deflected upwards by the cold nose. Inset shows coseismic slip distribution along the megathrust for all the models in (a). (c) Enlarged view of the rectangular area in (b) comparing displacement directions in the three colour-coded models in (a). (d) Sensitivity tests showing that the size of the elastic cold nose controls the postseismic forearc uplift.

### 3.2.4. Modelling modern geodetic postseismic observations

We have conducted a global synthesis of observations of short-term vertical deformation in the forearc region following great or large (moment magnitude ( $M_w$ )  $\geq 7.8$ ) subduction earthquakes (Figures 3.5–3.11, Table 3.1) with the results summarized in Table 3.1. For most events that occurred in this century, continuous Global Navigation Satellite System (GNSS) observations were available, but very few had dense spatial coverage just seaward of the volcanic arc. For some earlier events such as the 1946 Nankai, 1957 and 1965 Aleutian, and 1960 Chile earthquakes, vertical postseismic deformation was constrained by limited levelling, tide gauge or coastal field observations (Plafker and Savage, 1970; Thatcher, 1984; Wahr and Wyss, 1980). The quantity and quality of the observations vary tremendously between events, but postseismic uplift just seawards of the volcanic arc is observed or inferred wherever relevant data are available. Even for an event that occurred in the seventeenth century (southern Kuril), available palaeo-postseismic data show pronounced postseismic uplift in the region where the plate interface depth is 60–80 km (Sawai et al., 2004). It is important to note that the postseismic uplift supporting the presence of the rheological contrast is irrespective of the thermal state of the subduction zone, which depends mainly on the age of the subducting plate (Figures 3.5, Table 3.1). In the absence of other complications, the forearc uplift in the postseismic period is expected to be offset by later interseismic subsidence (Nishimura, 2004; Li et al., 2020). Here, however, we focus only on the postseismic uplift.

We choose four of the events summarized in Table 3.1 to construct 3D postseismic deformation models for a more quantitative analysis. The four events represent a wide range of data type, data quality, event size, and the age and hence thermal state of the subducting plate. We use a spherical-Earth finite-element modelling code that employs bi-viscous Burgers rheology (Figure 3.1b; e.g., Bürgmann and Dresen, 2008; Pollitz, 2019), and we invoke the actual slab geometry (Hayes et al., 2012) and coseismic slip distribution previously inferred from geodetic, seismic and tsunami observations (details in Methods and Table 3.2). In real Earth, the rigidity of the cold nose may be influenced by the temperature field, and the definition of the CNE is not as ideal as shown in

Figures. 3.1b and 3.2b, although fine details may not be resolvable by present geodetic observations. For simplicity, in modelling the four earthquakes, we assume that the CNE is located where the depth of the subduction interface is 70 km, consistent with the thermal argument of Wada and Wang (2009).

The main results along a margin-normal corridor are summarized in Figure 3.3 compared with observations. A map view of the observations and model results for the largest of the four events, the 1960  $M_w$  9.5 Chile earthquake, is shown in Figure 3.4. Map views of model-predicted postseismic deformation of the other three events compared with GNSS observations are shown in Figures 3.6, 3.8 and 3.10. Postseismic displacement time series from our models are compared with GNSS observations in Figures. 3.7, 3.9 and 3.11. Details for the four events and their models are described as follows.

Among all the events examined (Table 3.1), the 2011  $M_w$  9 Tohoku-oki earthquake yielded the highest-quality coseismic and postseismic deformation data. Japan Trench that hosted this event is about the coldest subduction zone examined, for its old subducting plate ( $\sim 130$  Ma) and fast subduction rate ( $> 8$  cm yr $^{-1}$ ). Over 40 coseismic slip distribution models have been obtained for this earthquake by inverting various coseismic observations (Wang et al., 2018). For our modelling, we use a slip distribution that is an average of 19 of these models that included seafloor GNSS measurements in the inversion (Table 3.2). The postseismic deformation following this earthquake was recorded by a dense land-based GNSS network and some seafloor sites (Ozawa et al., 2012; Yokota et al., 2018) (Figures 3.6 and 3.7). The landward motion of the near-trench area that opposes the seaward motion of the rest of the network and its geodynamic implications were studied by Sun et al. (2014). Important to the theme of this paper is the pronounced uplift just seawards of the volcanic arc extending to the outer coast (Figure 3.3). Five years after the earthquake, the peak uplift is  $\sim 0.4$  m and is located around the coastline where the plate interface depth is  $\sim 60$ – $70$  km (Figure 3.6). Our model that includes the cold nose readily explains this uplift (Figure 3.3). The model-predicted postseismic deformation near the volcanic arc is not sensitive to details of the coseismic slip distribution because the area is quite far from the main rupture zone.

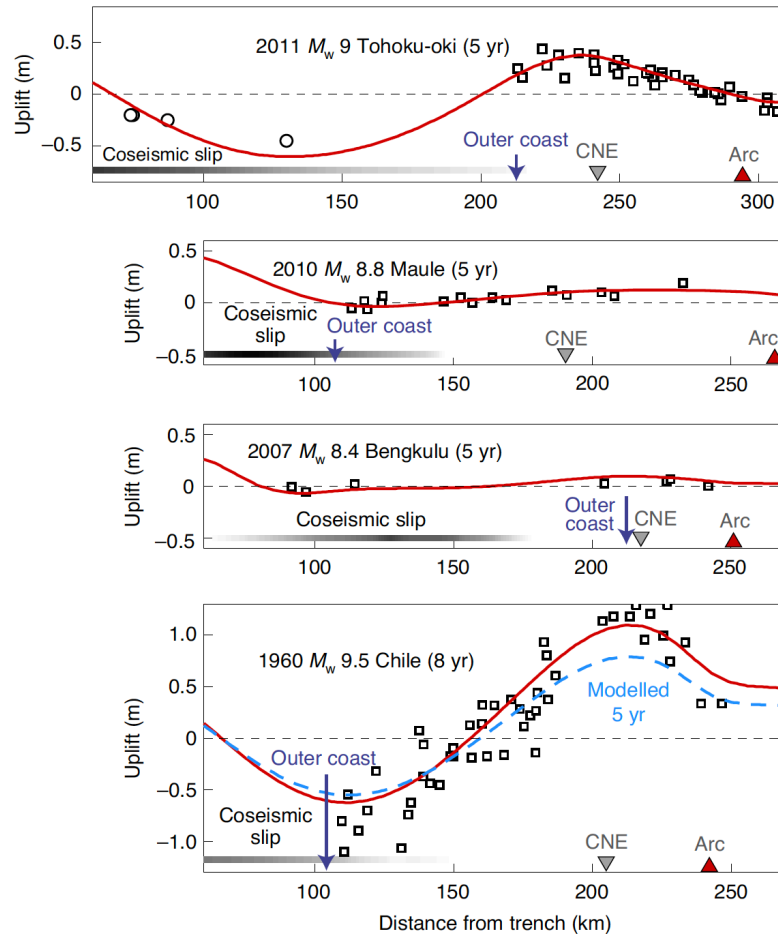


**Figure 3.3.** Model postseismic vertical deformation for four subduction earthquakes compared with observations. See Table 3.1 for data type and sources and Table 3.2 for model parameters. For the Chile event, only 8 yr postseismic data are available, but model uplift for 5 years after earthquake is also shown for comparison. Map views of model results, postseismic observations, coseismic slip distribution and location of the display profile are shown in, from top to bottom, Figures 3.6, 3.8, 3.10 and 3.4. Data (symbols) shown here are from within 200 km of display profile for the 2007 Bengkulu earthquake but 100 km for other events. Circles for the Tohoku-oki event are seafloor GNSS measurements. Model-predicted displacement time series are compared with GNSS observations in Figures 3.7, 3.9 and 3.11.

Postseismic deformation following the 2010  $M_w$  8.8 Maule earthquake was also recorded by a large number of GNSS sites (Figures 3.8 and 3.9). Compared with the Japan Trench, the central Chile subduction zone has a much younger subducting plate ( $\sim 33$  Ma), slightly slower subduction rate ( $6.6 \text{ cm yr}^{-1}$ ) and thus a warmer thermal regime. The coseismic slip had been determined in a number of studies by inverting



GNSS and other data. From the many published slip models, we use the average of nine of them that included GNSS data in the inversion (Table 3.1). Five years after the earthquake, GNSS measurements show broad uplift where the plate interface depth is around 80 km (Li et al., 2018; Figure 3.8). Our model results show that this uplift is consistent with the presence of the cold nose (Figures 3.3, 3.8 and 3.9). The presence of the cold nose was also inferred by Weiss et al. (2019), who directly inverted the Maule postseismic geodetic data to estimate mantle rheology.

The North Sumatra subduction zone has a slow margin-normal convergence rate (75% of  $\sim 5.9 \text{ cm yr}^{-1}$  oblique convergence) and a moderate slab age ( $\sim 69 \text{ Ma}$ ). The 2007  $M_w$  8.4 Bengkulu earthquake is an example of a smaller event recorded by sparse measurements. Despite the limited data coverage, the smaller size of the earthquake and the many tectonic differences from the other examples in Figure 3.3, postseismic uplift was systematically observed at GNSS sites just seaward of the volcanic arc (Feng et al., 2015). Again, our model readily explains this uplift by invoking the cold nose (Figures 3.3, 3.10 and 3.11). The more-complex uplift and subsidence pattern closer to the trench and away from our region of interest can be explained by having local afterslip (Figure 3.10).

### **3.2.5. Postseismic deformation of the 1960 giant Chile earthquake**

The most remarkable example is the 1960  $M_w$  9.5 Chile earthquake, by far the largest instrumentally recorded earthquake, which involved the warmest subduction-zone segment studied here (Table 3.1). G. Plafker (Plafker and Savage, 1970) conducted a geological field survey of the rupture area in 1968, eight years after the earthquake and two decades before the birth of GNSS. In terms of constraining earthquake deformation, these geological data are equivalent to campaign-style geodetic measurements. The uplift and subsidence pattern mapped by Plafker led to the recognition of the subduction megathrust being the source of the rupture and hence became a landmark in the advancement of the plate tectonics theory. However, the belt of uplift sandwiched between the main zone of coseismic subsidence and the volcanic arc (Figure 3.4) has been enigmatic for the past five decades.

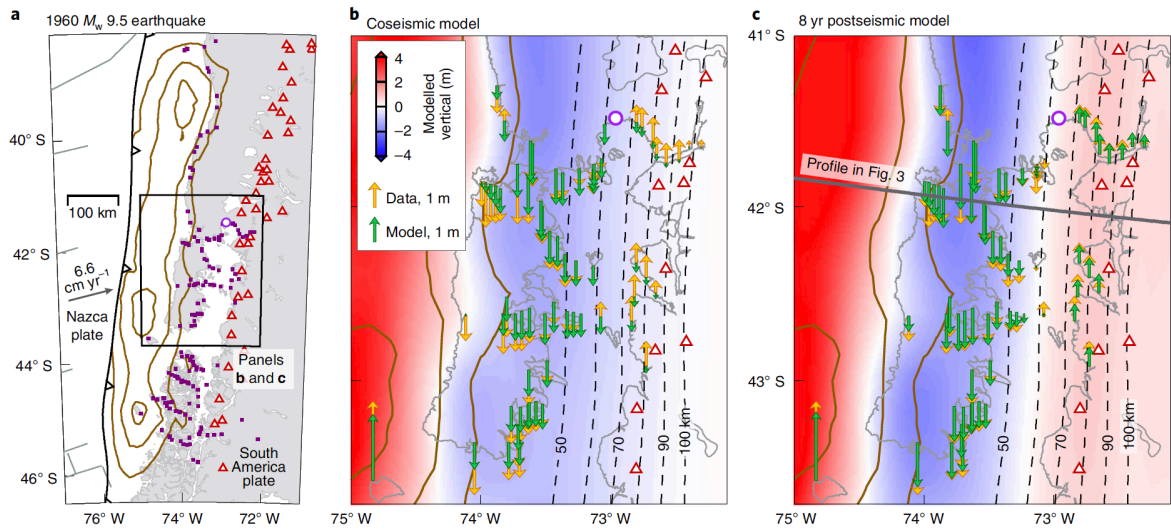


**Figure 3.4.** Observed and modelled deformation associated with the 1960  $M_w$  9.5 Chile earthquake. (a) Distribution of the Plafker measurements (purple squares) (Plafker and Savage, 1970) and coseismic slip distribution contoured at 10 m intervals (Ho et al., 2019). Red triangles represent locations of volcanoes. The purple circle marks the location of the tide gauge at Puerto Montt. (b) Comparison of Plafker measurements (orange arrows) with coseismic deformation (green arrows and background colour) modelled using the shown coseismic slip distribution (same contours as in (a)). (c) Similar to (b), but the model deformation is for eight years after the earthquake.

The uplift in this belt peaks to  $\sim 1$  m where the slab interface depth is  $\sim 70$ – $80$  km (Figure 3.4b). Plafker’s observations were meant to delineate coseismic deformation, but no rupture models can explain such a large uplift so far away from the rupture zone (Plafker and Savage, 1970; Moreno et al., 2009; Ho et al., 2019), unless physically implausible, exceedingly deep slip is invoked (Barrientos and Ward, 1990). The most recent rupture model predicts coseismic subsidence in this area (Figure 3.4b). However, we should recall that Plafker’s measurements were made eight years after the earthquake and thus must contain substantial postseismic deformation signal. On the basis of the mechanism of postseismic deformation illustrated in Figure 3.2, we can firmly conclude that this uplift is primarily viscoelastic postseismic deformation in the presence of the cold nose (Figures 3.3 and 3.4). Therefore, these measurements provided some of the earliest evidence for postseismic deformation and the presence of the cold nose.

Independent evidence for the postseismic uplift here came from tide gauge measurements

at Puerto Montt (Barrientos et al., 1992), the location of which is shown in Figure 3.4. Modern GNSS measurements indicate that the uplift is continuing today but at a diminished rate (Wang et al., 2007; Luo et al., 2020).

### 3.2.6. Other contributing factors

Some of the uplift signals summarized in Table 3.1 were previously noticed by other researchers. In the past, the uplift was attributed to frictional slip (Linde and Silver, 1989; Muto et al., 2019), or almost equivalently postseismic shear of a thin zone of extremely low viscosity (Klein et al., 2016), at depths as large as 70 to >100 km. The very deep frictional or viscous slip of the subduction interface is less compatible with the full coupling of the slab and mantle wedge at such depths required by the presence of the hot sub-arc mantle wedge (Wada and Wang, 2009; Syracuse et al., 2010; Abers et al., 2017) (Figure 3.1).

The mechanism discussed in this paper is based on geologically reasonable structural conditions. Similar postseismic uplift may be produced in some models without invoking the cold nose of the forearc mantle wedge if less-reasonable conditions are introduced. For example, if one assumes a very thick elastic upper plate in the arc and backarc area by neglecting its very warm thermal condition, minor uplift occurs near the volcanic front in a model without the cold nose (Figure 3.12a) unless the coseismic slip of the megathrust is assumed to be deeper (Figure 3.12b).

Some recent postseismic deformation models used temperature-dependent rock rheology (Peña et al., 2019; 2020; van Dinther et al., 2019). By invoking subduction-zone thermal structures similar to those in Wada and Wang (2009), Syracuse et al. (2010) and Abers et al. (2017), these models all included the mantle-wedge cold nose (Figure 3.1), and they all predicted postseismic uplift near the volcanic area qualitatively similar to our models. Although these previous studies did not recognize the importance of the cold nose but speculated on other mechanisms to cause the uplift (Peña et al., 2019) or even assumed it to be coseismic (van Dinther et al., 2019), their results in effect corroborate our findings. More important, these results also demonstrate the robustness of the role of

the elastic cold nose in controlling postseismic deformation regardless of parametric details of fault and rock rheology.

### 3.2.7. Methods

To model postseismic deformation, we use the spherical-Earth finite-element code PGCviscl-3D developed by J. He at the Pacific Geoscience Centre, Geological Survey of Canada. The model includes elastic plates and viscoelastic mantle with the bi-viscous Burgers rheology. The Burgers body is composed of a Kelvin solid (rigidity  $\mu_K$  and viscosity  $\eta_K$ ) in series with a Maxwell fluid (rigidity  $\mu_M$  and viscosity  $\eta_M$ ), representing the transient and steady-state rheology, respectively (Figure 3.1b). We assume a uniform rock density and Poisson's ratio of  $3,300 \text{ kg m}^{-3}$  and 0.25, respectively, and rigidity values of the elastic plates and viscoelastic mantle of 48 GPa and 64 GPa, respectively. The mantle-wedge viscosity is assumed to be an order of magnitude lower than the oceanic mantle, to account for the higher temperature and the presence of fluids from the subducting plate and melts (Wang et al., 2012), similar to many other subduction-zone earthquake cycle deformation models (e.g., Moreno et al., 2011; Freed et al., 2017; Suito, 2017; Sun et al., 2018). Coseismic slip and afterslip are assigned using the split-node method (Melosh and Raefsky, 1981). The effect of gravity is approximated using the stress-advection approach (Peltier, 1974; Wang et al., 2001).

The geometry of the slab in the 2D models shown in Figure 3.2 is designed to represent a typical subduction zone. In these models, the thicknesses of the subducting and upper plates are 40 and 30 km, respectively. The Maxwell ( $\eta_M$ ) and Kelvin ( $\eta_K$ ) viscosities are  $5 \times 10^{19}$  and  $5 \times 10^{18}$  Pa s, respectively, for the oceanic mantle, and  $5 \times 10^{18}$  ( $\eta_M$ ) and  $5 \times 10^{17}$  ( $\eta_K$ ) for the mantle wedge. In the cold-nose model, the cold nose extends to where the depth of the subduction interface is 70 km except for those shown in Figure 3.2d for sensitivity tests. In the model without the cold nose but with a higher mantle-wedge viscosity (Figure 3.2a),  $\eta_M = 1 \times 10^{19}$  Pa s.

The models of the four great earthquakes summarized in Figure 3.3 each require site-specific 3D geometry of the subducting plate and parameter values. We employ the slab geometry of slab 1.0 (Hayes et al., 2012) except for the 2011  $M_w$  9 Tohoku-oki

earthquake, in which the slab geometry is smoothed from Sun et al. (2014). The viscosity values vary slightly between models to fit surface observations (Table 3.2). Unlike the 2D models shown in Figure 3.2, where we purposely leave out afterslip to focus on the main physical process, we include afterslip for the 3D real-earthquake models wherever observational constraints are adequate. However, our results indicate that its effect is minor. We incorporate a thin layer of  $\sim 3\text{--}5$  km between the slab and the cold nose in the depth range of  $\sim 55\text{--}70$  km, with the same viscosity as the rest of the viscoelastic mantle wedge, to simulate the viscous or semi-viscous shear of materials in postseismic deformation (e.g., Sun et al., 2014; Hu et al., 2016). We use a thinner upper plate at the volcanic arc to represent lower stiffness in this area (Hu et al., 2014; Itoh et al., 2019a). The location and width of the thinner part of the upper plate are based mainly on the distribution of arc volcanoes. Postseismic observations for these earthquakes and the other earthquakes that are not modelled but are shown in Figure 3.5 are summarized in Table 3.1 (Bevis et al., 2020; Delouis et al., 2010; Hergert and Heidbach, 2006; Ioki and Tanioka, 2016; Itoh et al., 2019b; Kogan et al., 2011; 2013; Lin et al., 2013; Lorito et al., 2011; Luttrell et al., 2011; Moreno et al., 2012; Müller et al., 2008; Nicolsky et al., 2016; Plafker, 1969; Pollitz et al., 2011; Tong et al., 2010; Vigny et al., 2011; Yue et al., 2014).

### **3.2.8. Acknowledgements**

We thank X. Zhou for discussion. H.L. was supported by a James A. & Laurette Agnew Memorial Award, a University of Victoria Graduate Award, Graduate Support from Ocean Networks Canada, and Discovery Grant RGPIN-2016-03738 to K.W. from the Natural Sciences and Engineering Research Council of Canada. This is Geological Survey of Canada contribution 20200524.

### 3.3. Extended Data

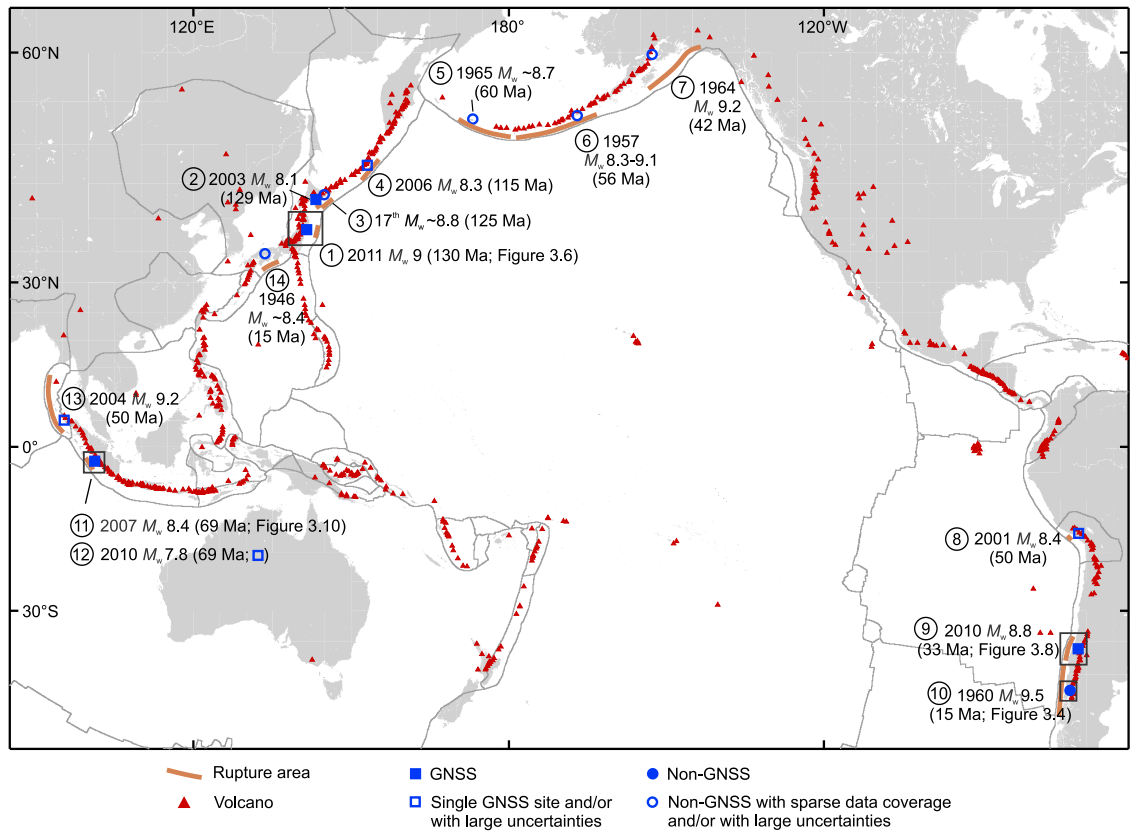


**Figure 3.5.** Global synthesis of postseismic uplift following subduction earthquakes observed in the forearc near the volcanic arc. Events are labelled with index numbers (circled) as listed in Table 3.1, year of occurrence, moment magnitude, and age of the subducting plate at trench. Black-solid line boxes approximately outline the map areas of Figures 3.4c, 3.6, 3.8, and 3.10. Plate boundaries (grey lines) are from Bird (2003). Locations of volcanoes are from Aster Volcano Archive (NASA, METI; <https://gbank.gsj.jp/vsldb/image/>).

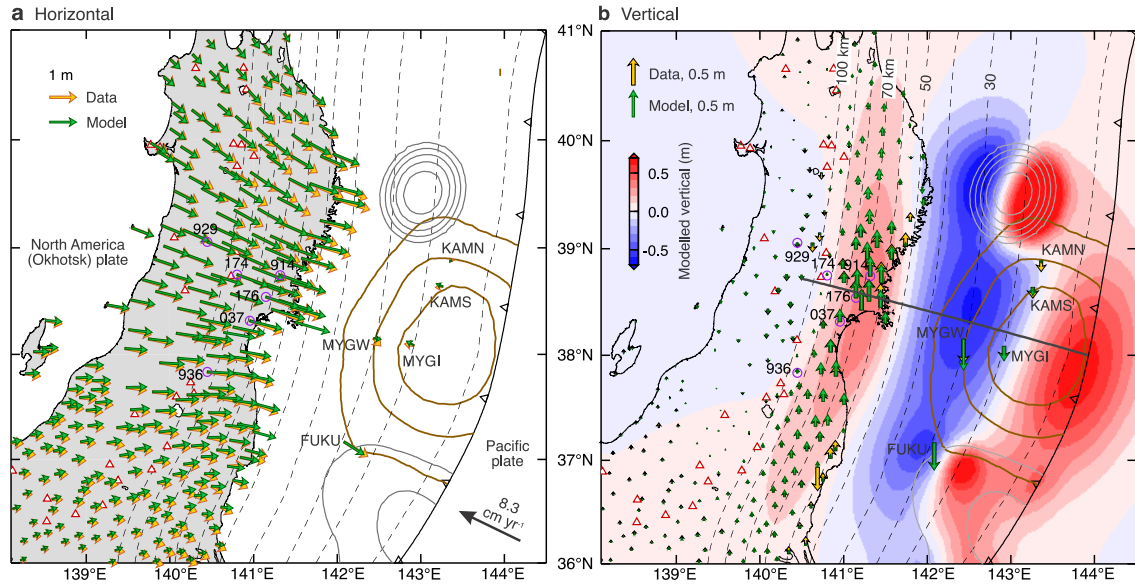


**Figure 3.6.** Map view of observed and modelled postseismic deformation 5 years after the 2011  $M_w$  9 Tohoku-oki earthquake. (a) Horizontal component. Coseismic slip distribution (Table 3.2) is contoured at 10 m interval (copper lines). Cumulative afterslip, contoured at 1 m interval (grey lines), is slightly modified from Wang et al., (2018). (b) Vertical component. The black solid line shows the location of the corridor in Figure 3.3. Land GNSS data are based on GNSS daily solutions from the Geospatial Information Authority of Japan (GSI) (Ozawa et al., 2012; Nakagawa, 2009), and seafloor GNSS data are from Japan Coast Guard (Yokota et al., 2018). Time series of the labelled land and seafloor GNSS sites are shown in Figure 3.7. In these and other map view figures in Figure 3.4 and Extended Data, plate interface depth is contoured using dashed lines, and locations of volcanoes from Aster Volcano Archive (NASA, METI; <https://gbank.gsj.jp/vsldb/image/>) are indicated using red triangles.

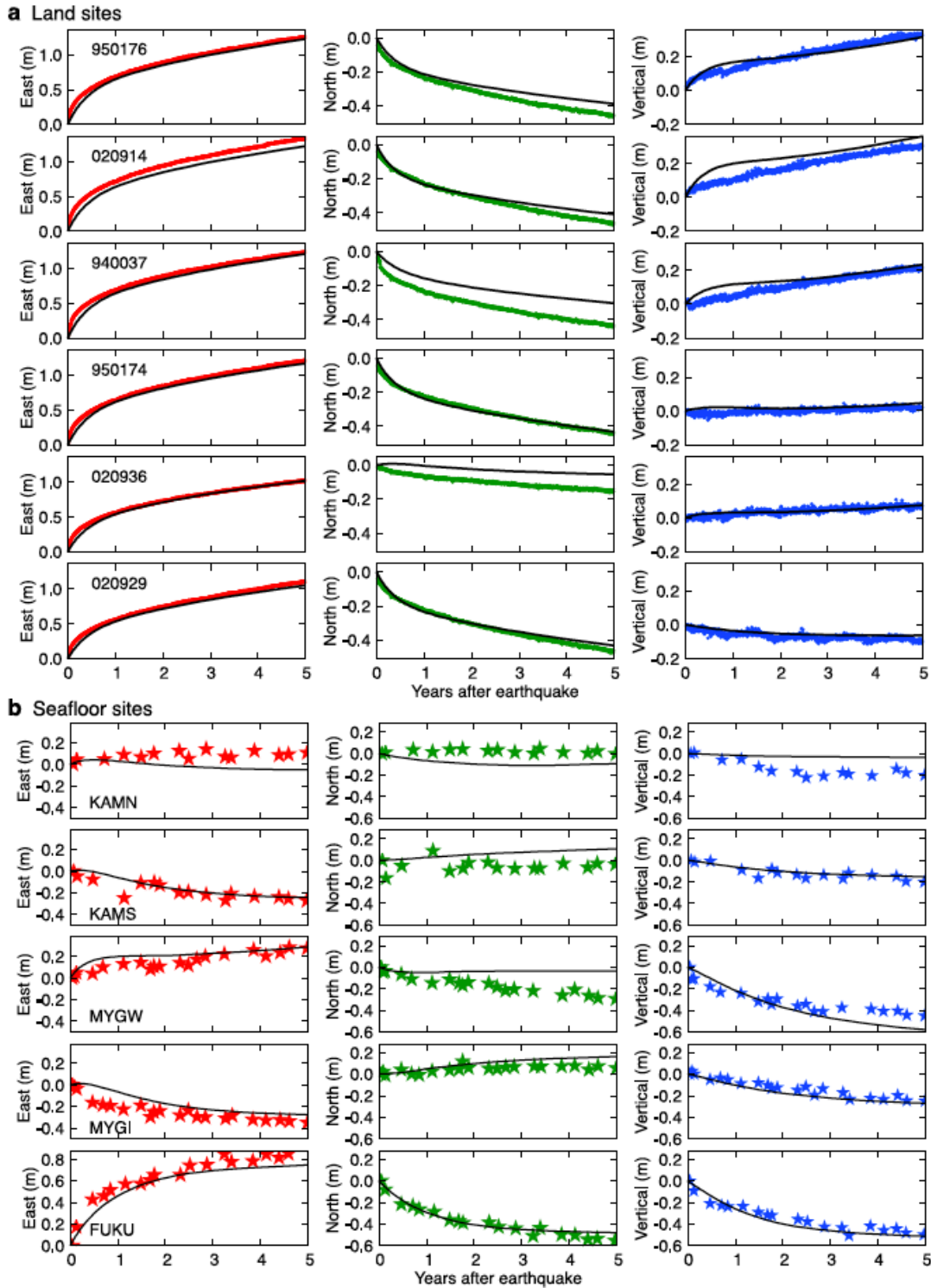


**Figure 3.7.** Observed (colour symbols) and modelled (black curves) time series of GNSS sites after the 2011  $M_w$  9 Tohoku-oki earthquake. From left to right: east, north, and vertical components. Site locations are shown in Figure 3.6. (a) Land sites. (b) Seafloor sites.



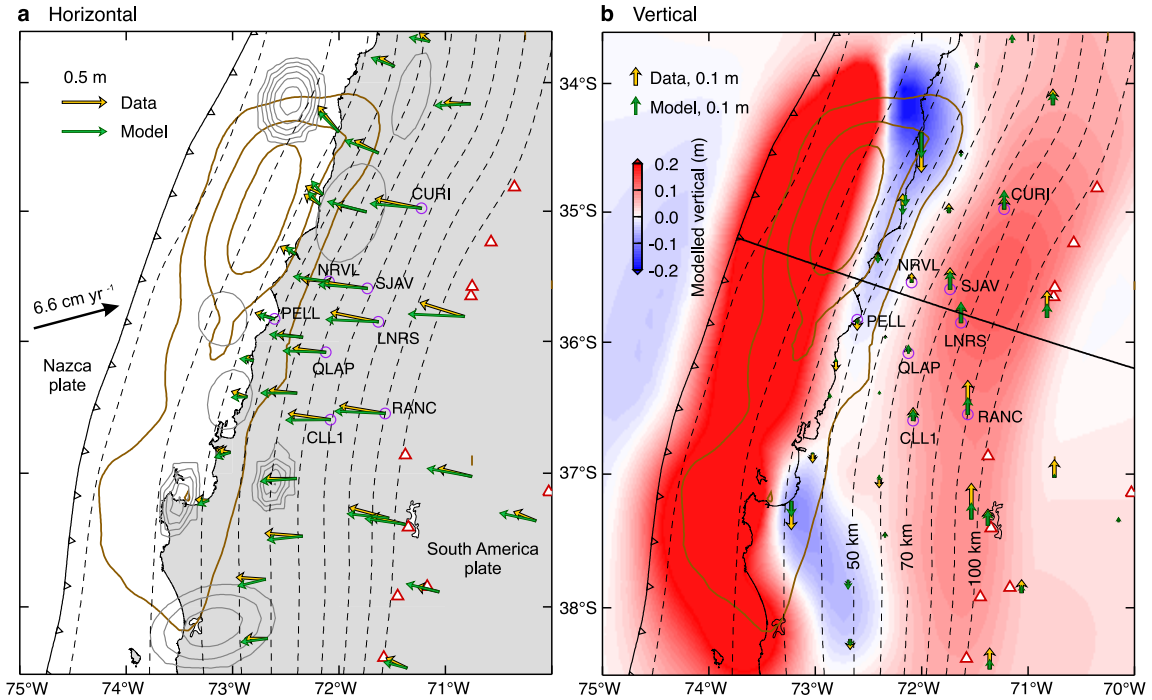


**Figure 3.8.** Map view of observed and modelled postseismic deformation 5 years after the 2010  $M_w$  8.8 Maule earthquake. (a) Horizontal component. Coseismic slip distribution (Table 3.2) is contoured at 4 m interval (copper lines). Cumulative afterslip, contoured at 0.3 m interval (grey lines), is modelled using the method of Sun et al. (2018). (b) Vertical component. The black line shows the location of the corridor in Figure 3.7 GNSS data are from Li et al. (2018). Time series of the labelled GNSS sites are shown in Figure 3.9.

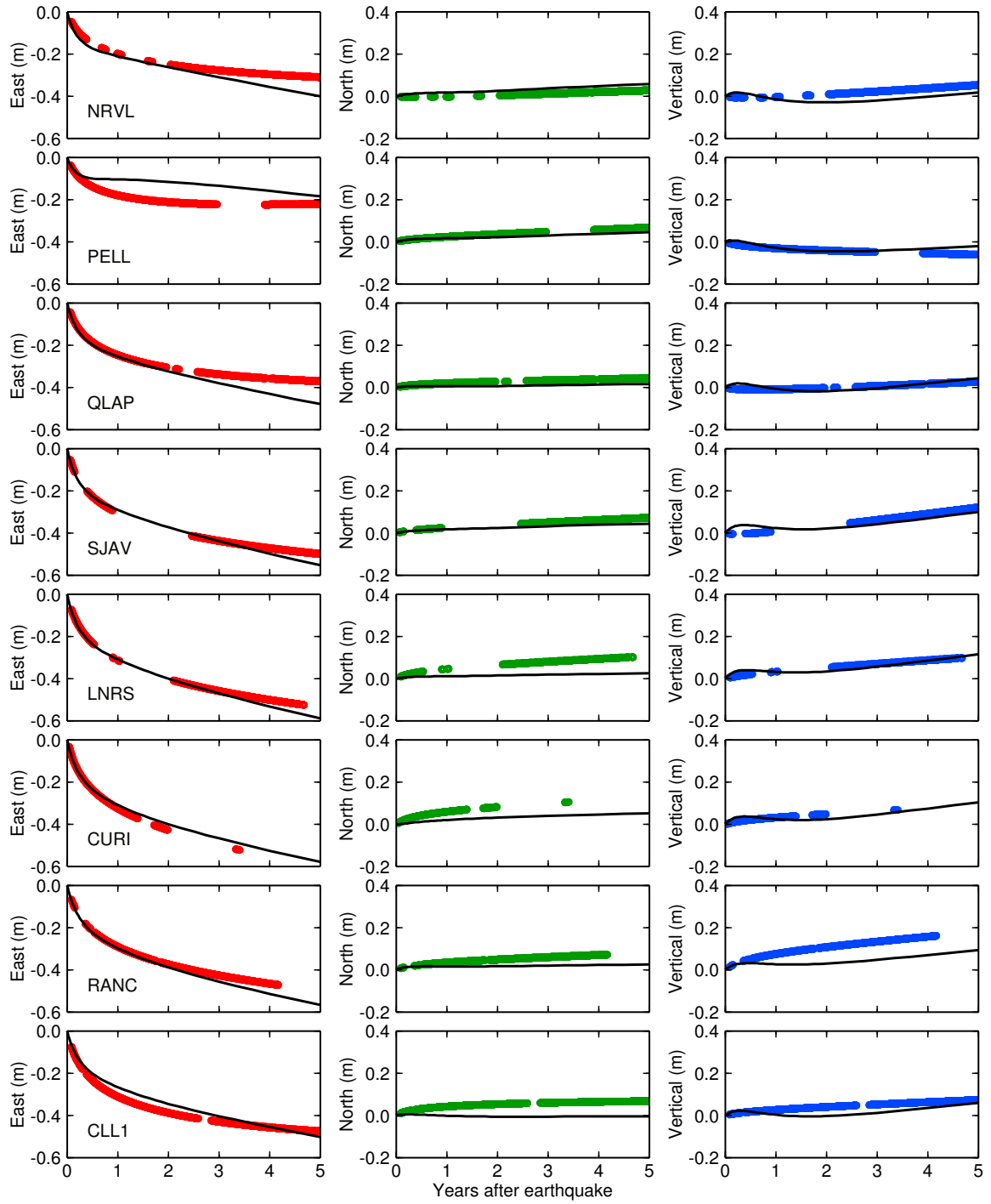


**Figure 3.9.** Observed (colour symbols) and modelled (black curves) time series of GNSS sites after the 2010  $M_w$  8.8 Maule earthquake. From left to right: east, north, and vertical components. Site locations are shown in Figure 3.8.

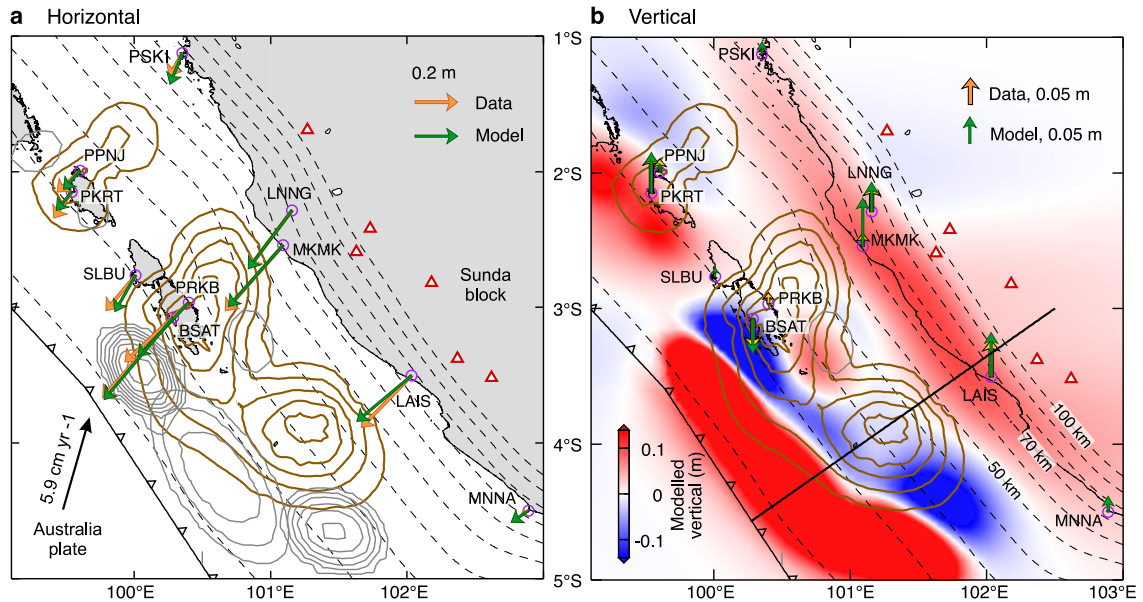


**Figure 3.10.** Map view of observed and modelled postseismic deformation 5 years after the 2007  $M_w$  8.4 Bengkulu earthquake. (a) Horizontal component. Coseismic slip distribution is contoured at 1 m interval (copper lines; Tsang et al., 2016). Cumulative afterslip, contoured at 0.4 m interval (grey lines), is modelled using the method of Sun et al. (2018). (b) Vertical component. The black line shows the location of the corridor in Figure 3.3. GNSS data are from Feng et al. (2015). Time series of the labelled GNSS sites are shown in Figure 3.11.

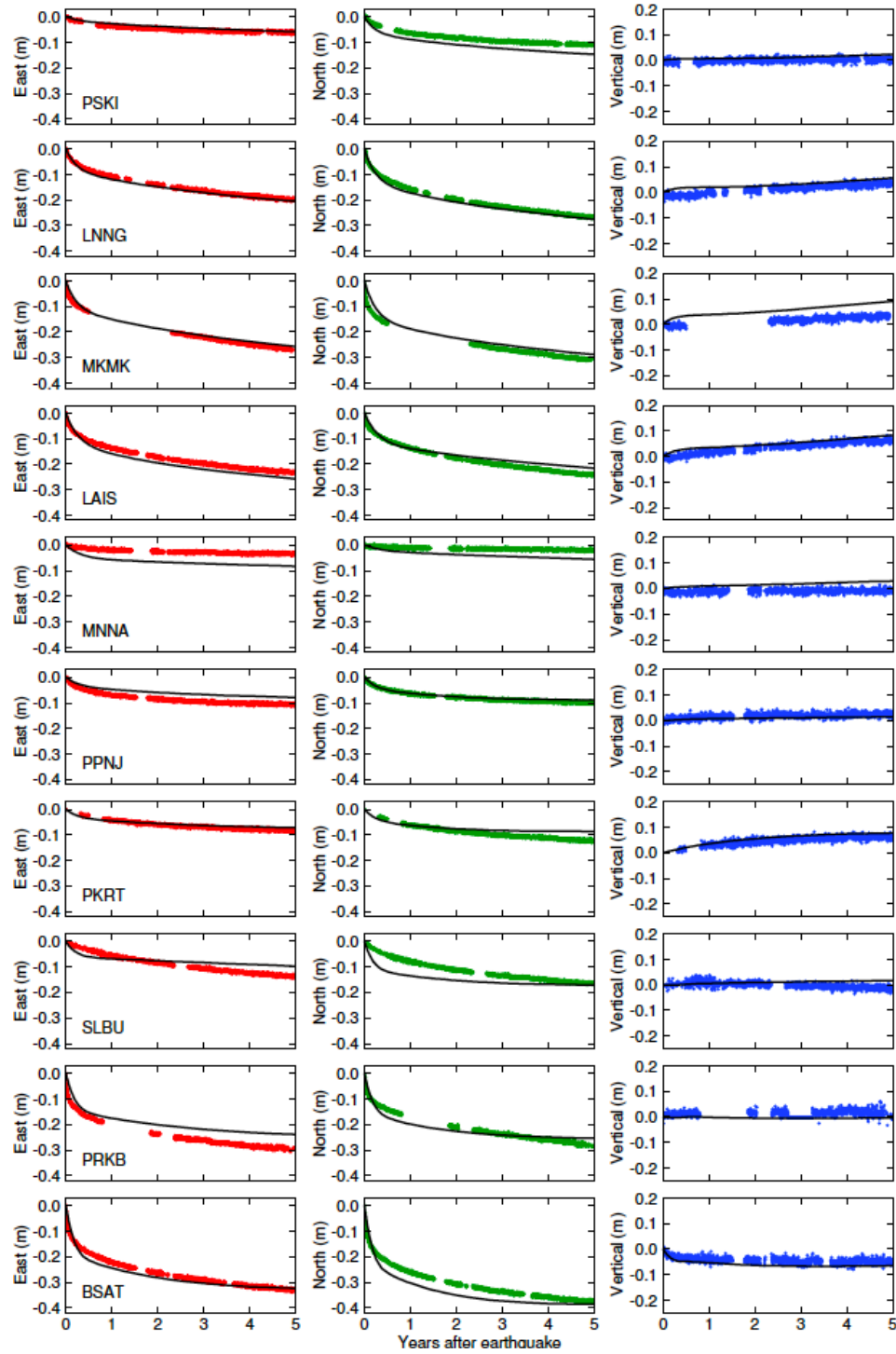


**Figure 3.11.** Observed (colour symbols) and modelled (black curves) time series of GNSS sites after the 2007  $M_w$  8.4 Bengkulu earthquake. From left to right: east, north, and vertical components. Site locations are shown in Figure 3.10.

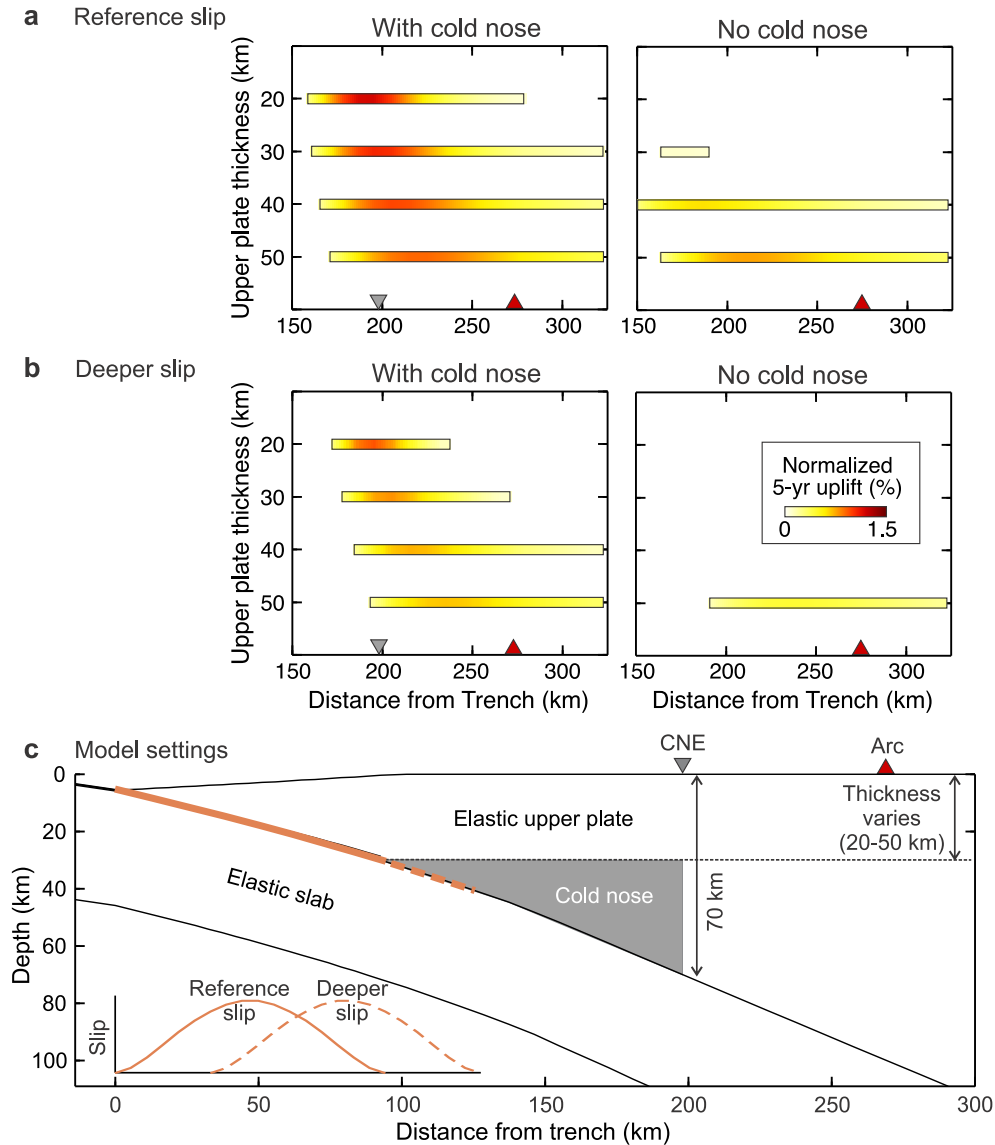


**Figure 3.12.** 2-D Models of postseismic deformation to test the effects of upper plate thickness. The model setup is identical to that in Figure 3.2 (Methods), except for the use of different upper plate thicknesses and/or coseismic slip depths in different simulations. Shown cumulative postseismic displacements are 5 years after an earthquake, normalized by peak coseismic slip. (a) Model tests showing how the upper plate thickness affects postseismic forearc uplift with or without the elastic cold nose. Minor uplift in the area of interest may occur without the cold nose if the upper plate in the warm arc and backarc area is unreasonably thick (that is, 50 km). (b) Same as a except for deeper coseismic slip. c, Model structure and parameters. Inset shows coseismic slip distribution along the megathrust for the models in (a) (Reference) and (b) (Deeper).

**Table 3.1.** Summary of postseismic forearc uplift observations following subduction earthquakes. (Part A)

Index	Subduction zone	Subducting plate age at trench* (Ma)	Earthquake	$M_w$	Representative postseismic uplift $U_r^\dagger$ (m)	Time after earthquake of $U_r$ (yr)
1	Japan Trench	130	2011 Tohoku-oki	9	0.4	5
2	S Kuril	129	2003 Tokachi-oki	8.1	~0.1	7.5
3	S Kuril	125	17 <sup>th</sup> century giant Kuril	~8.8	~1	$\geq 27$
4	C Kuril	115	2006 Kuril	8.3	~0.03	3
5	Aleutians	60	1965 (Rat Islands) Andreanof Islands	~8.7	~0.2	5
6	Aleutians	56	1957 Andreanof Islands	8.3-9.1	~0.15	5
7	Alaska	42	1964 Alaska	9.2	~0.3	~1
8	S Peru	50	2001 Peru	8.4	~0.035	5
9	SC Chile	33	2010 Maule	8.8	~0.1	5
10	S Chile	15	1960 Chile	9.5	~1	8
11	N Sumatra	69	2007 Bengkulu	8.4	0.07	5
12	N Sumatra	69	2010 Mentawai	7.8	~0.007	5
13	N Sumatra	50	2004 Sumatra	9.2	~0.18	5
14	Nankai	15	1946 Nankai	~8.4	~0.02	13

\* From Müller et al. (2008).

† If there is only a single observation, that value is used for  $U_r$ .

**Table 3.1. (Part B)**

Index	Approximate subduction interface depth at $U_r$ (km)	Approximate distance to trench at $U_r$ (km)	Postseismic observation method	References for postseismic observations	Notes
1	70	240	GNSS	GSI (Ozawa et al., 2012; Nakagawa, 2009)	Figures 3.3, 3.6 and 3.7
2	75	210	GNSS	Itoh et al. (2019b)	Uplift reported for 1667-1694. $M_w$ from Ioki and Tanioka (2016)
3	60-80	150-200	Estimates using diatom assemblages	Sawai et al. (2004)	
4	85	190	GNSS	Kogan et al. (2011; 2013)	
5	65	150	Tide gauge	Wahr and Wyss (1980)	Single tide gauge ATTU
6	75	290	Tide gauge	Wahr and Wyss (1980); Nicolsky et al. (2016)	Two tide gauges UNALASKA (Dutch Harbour) and ADAK
7	95	400	Eyewitness accounts	Plafker (1969)	Uncertainty reported ~0.1 m
8	100	175	GNSS	Hergert and Heidbach (2006); Bevis et al. (2020)	Single GNSS site AREQ
9	75	205	GNSS	Li et al. (2018)	Figures 3.3, 3.8 and 3.9
10	80	220	Field survey of land-level change	Plafker and Savage (1970)	Field survey by G. Plafker in 1968; Figures 3.3 and 3.4
11	80	230	GNSS	Feng et al. (2015)	Figures 3.3, 3.10 and 3.11
12	80	250	GNSS	Feng et al. (2015)	Single GNSS site UMLH
13	75	270	GNSS	Feng et al. (2015)	
14	80	350	Levelling	Thatcher (1984)	Survey (levelling line “H”) taken in 1951-1964

**Table 3.2.** Parameters for the postseismic deformation models of the four earthquakes shown in Figure 3.3.\* (part A)

Earthquake	Subduction zone	Coseismic slip model reference	Mantle wedge		Oceanic mantle	
			viscosity		viscosity	
			(10 <sup>18</sup> Pa s)		(10 <sup>18</sup> Pa s)	
			$\eta_M$	$\eta_K$	$\eta_M$	$\eta_K$
2011 $M_w$ 9 Tohoku-oki	Japan Trench	Wang et al. (2018) <sup>‡</sup>	4.5	1	50	5
2010 $M_w$ 8.8 Maule	SC Chile	Average of 9 models <sup>§</sup>	3	0.5	22	2.5
2007 $M_w$ 8.4 Bengkulu	N Sumatra	Tsang et al. (2016)	3	0.5	40	4
1960 $M_w$ 9.5 Chile	S Chile	Ho et al. (2019)	3	0.5	20	2

\*Map views of the model results for the Tohoku-oki, Maule, and Bengkulu earthquakes are shown in Figures 3.6, 3.8 and 3.10, respectively. Those for the Chile earthquake are shown in Figure 3.4.

<sup>‡</sup> An average of 19 published slip models summarized in Figure 8 of Wang et al. (2018).

<sup>§</sup> The 9 models are from Delouis et al. (2010), Lin et al. (2013), Lorito et al. (2011), Luttrell et al. (2011), Moreno et al. (2012), Pollitz et al. (2011), Tong et al. (2010), Vigny et al. (2011) and Yue et al. (2014).



**Table 3.2.** (Part B)

Earthquake	Subducting plate thickness (km)	Upper plate thickness (km)	Upper plate thickness at arc (and range) (km) <sup>†</sup>
2011 $M_w$ 9 Tohoku-oki	45	30	20 (100-110)
2010 $M_w$ 8.8 Maule	30	50	30 (110-130)
2007 $M_w$ 8.4 Bengkulu	40	30	15 (95-105)
1960 $M_w$ 9.5 Chile	30	35	15 (90-110)

<sup>†</sup> Numbers in parentheses show depth range of the subduction interface beneath the thinner part of the upper plate.

## **Chapter 4. Landward increase in GNSS velocities in South Chile indicating enhanced interseismic megathrust locking**

This chapter presents and explains a unique new observation of interseismic deformation. The main body of this chapter consists of a published journal article [Luo et al., 2020]. The chapter consists of three sections, with Section 4.1 describing basic information of the article, Section 4.2 presenting the article itself, and section 4.3 providing the Appendices accompanying the published article.

### **4.1. Article Information**

#### **4.1.1. Author and Coauthor Contributions**

This paper is a product of an international collaboration involving scientists from five different countries. The author of this dissertation H.L. did the modelling. H.L. and Coauthor B.A. drafted the figures. Coauthor R.M.R. led the collaboration. Coauthor M.B. initiated an early phase of the collaboration and independently processed the COYQ data for calibration. Coauthor B.A. processed all the GNSS data. Coauthors V.M., R.M.R., R.F., and B.A. carried out field work. All the authors contributed to the writing of the paper.

#### **4.1.2. Citation**

Luo, H., Ambrosius, B., Russo, R. M., Mocanu, V., Wang, K., Bevis, M., & Fernandes, R. (2020). A recent increase in megathrust locking in the southernmost rupture area of the giant 1960 Chile earthquake. *Earth and Planetary Science Letters*, 537, 116200. doi: 10.1016/j.epsl.2020.116200.

#### **4.1.3. Author's Names and Affiliations**

Haipeng Luo<sup>1</sup>, Boudewijn Ambrosius<sup>2</sup>, Raymond M. Russo<sup>3</sup>, Victor Mocanu<sup>4</sup>, Kelin Wang<sup>5,1\*</sup>, Michael Bevis<sup>6</sup>, Rui Fernandes<sup>7</sup>

<sup>1</sup>School of Earth and Ocean Sciences, University of Victoria, Victoria, British Columbia, Canada

<sup>2</sup>Faculty of Aerospace Engineering, Delft University of Technology, Kluyverweg 1, 2629 HS, Delft, the Netherlands

<sup>3</sup>Department of Geological Sciences, University of Florida, Gainesville, FL, 32608 USA

<sup>4</sup>Department of Geophysics, University of Bucharest, 6 Traian Vuia Street, RO-020956, Bucharest, Romania

<sup>5</sup>Pacific Geoscience Centre, Geological Survey of Canada, 9860 West Saanich Road, Sidney, British Columbia, Canada

<sup>6</sup>School of Earth Sciences, Ohio State University, 125 South Oval Mall, Columbus, OH 43210, USA

<sup>7</sup>University of Beira Interior, Instituto D. Luiz, Rua Marquês d'Ávila e Bolama, 6201-001 Covilhã, Portugal

Corresponding author: Kelin Wang (kelin.wang@canada.ca)

#### **4.1.4. Article Format**

The text and figures included in Section 4.2 are taken directly from the Earth and Planetary Science Letters article. The Appendices for the article are reformatted as Supplementary Material and are given in Section 4.3. Sections, figures and tables in the original article have been renumbered to be compatible with the chapter format of the dissertation. The width of Table 4.2 in the Appendices of the original publication exceeded the page width of the dissertation. To fit the dissertation format, here the table is separated into parts A and B sharing the same first column. References cited in the article are included in the bibliography of the dissertation.

## **4.2. A recent increase in megathrust locking in the southernmost rupture area of the giant 1960 Chile earthquake**

### **4.2.1. Abstract**

After a great subduction earthquake, viscoelastic stress relaxation causes prolonged seaward motion of inland areas of the upper plate, as was observed around the turn of the century in the area of the 1960  $M_w$  9.5 Chile earthquake with Global Navigation Satellite System (GNSS) measurements. However, recent GNSS observations during 2010–2019 indicate a systematic decrease in the velocity of the seaward motion over a region covering the latitudinal range of the southern half of the 1960 rupture. Data from the only long-lived continuous site in this region (COYQ since 1997), situated over 200 km away from the trench, suggest that the decrease in the seaward velocity (or increase in the landward velocity) occurred within a few years prior to 2010. This rapid and regional change cannot be explained by viscoelastic relaxation. We thus propose that the change was caused by a relatively sudden downdip widening of the zone of locking along the megathrust. Using three-dimensional finite element modelling, we find that the observed velocity change cannot be otherwise explained, although the amount of the increase in locking cannot be uniquely determined because of trade-offs between, and uncertainties in, the various parameters involved. For example, the degree of the increase in locking is affected by the value of coseismic slip in 1960 in the southernmost part of the rupture zone. A postseismic deformation model with greater coseismic slip in accordance with the most recent coseismic slip model in the literature better fits COYQ data prior to 2005 and requires greater locking increase afterwards. A model with less coseismic slip requires less locking increase but an additional long-term slow slip event prior to 2005. The rapid surface velocity change and the inferred increase in megathrust locking several decades after a great earthquake present new challenges to the understanding of fault mechanics and subduction zone dynamics.

### **4.2.2. Introduction**

The geodetically observed evolution of crustal deformation following a subduction earthquake is understood to be controlled by the combined effects of viscoelastic mantle

rheology, fault creep such as afterslip, and relocking of the megathrust. Immediately after a great earthquake, the trench area and areas farther landward exhibit opposing motion, as illustrated by the motion of sites A and B at stage  $t_1$  in Figure 4.1. This is mostly a consequence of viscoelastic relaxation of the stress induced by the earthquake (Sun et al., 2014; Sun and Wang, 2015), although afterslip downdip of the rupture zone can also play an important role (Pritchard and Simons, 2006). As the effect of the viscoelastic relaxation diminishes with time and the effect of fault locking becomes more dominant, the boundary dividing the regions of opposing motion gradually migrates landward, eventually leading to wholesale landward motion of the upper plate (Wang et al., 2012) (Figure 4.1). The time it takes to complete the process of motion reversal depends on the magnitude of the earthquake, as demonstrated by Sun et al. (2018) using geodetic observations and viscoelastic deformation models of great subduction earthquakes worldwide. For events of moment magnitude ( $M_w$ ) 8, the reversal takes about a decade or so; for  $M_w > 9$  events, this process can take an order of magnitude longer.

The largest magnitude earthquake yet recorded instrumentally, the  $M_w$  9.5 1960 Chile earthquake, ruptured the Nazca-South America subduction interface over a distance of  $920 \pm 100$  km, from Valdivia in the north to the Nazca-Antarctica-South America triple junction in the south (Cifuentes, 1989), with coseismic slip estimates up to 40 m (Plafker and Savage, 1970; Barrientos and Ward, 1990; Moreno et al., 2009). Recent analysis of the records of the tsunami generated by this earthquake confirmed the large coseismic slip (Ho et al., 2019).

Analyses of Global Navigation Satellite Systems (GNSS) measurements four decades after the 1960 Chile earthquake (Klotz et al., 2001; Khazaradze et al., 2002; Wang et al., 2007; Moreno et al., 2011) showed opposing motion at campaign GNSS sites some 200–300 km from the Nazca trench (Figure 4.2), much like the  $t_2$  stage in Figure 4.1a. The research groups that made the GNSS observations shown in Figure 4.2 each used a slightly different definition of the South America (SA) reference frame, but the resultant differences in the derived velocities are negligibly small for the purpose of studying regional postseismic and interseismic deformation. The observed deformation pattern is reasonably well explained as a snapshot of a deformation history predicted using a spherical-Earth viscoelastic finite element model (Sun et al., 2018) (Figure 4.2). The

viscoelastic modelling shows that the westward (trenchward or seaward) motion of the area 200–300 km east of the trench and farther away is not expected to diminish or to reverse direction until 90–100 yrs post coseismic rupture ( $\sim$  mid 21st C.) (Hu et al., 2004; Wang et al., 2012; Sun et al., 2018). However, we show in this paper that more recent GNSS observations made in the early 21st century indicate unexpectedly early deceleration of seaward velocities or even reversal of crustal motion in this area, indicating an earlier than expected transition from the  $t_2$  to  $t_3$  stages illustrated in Figure 4.1a.

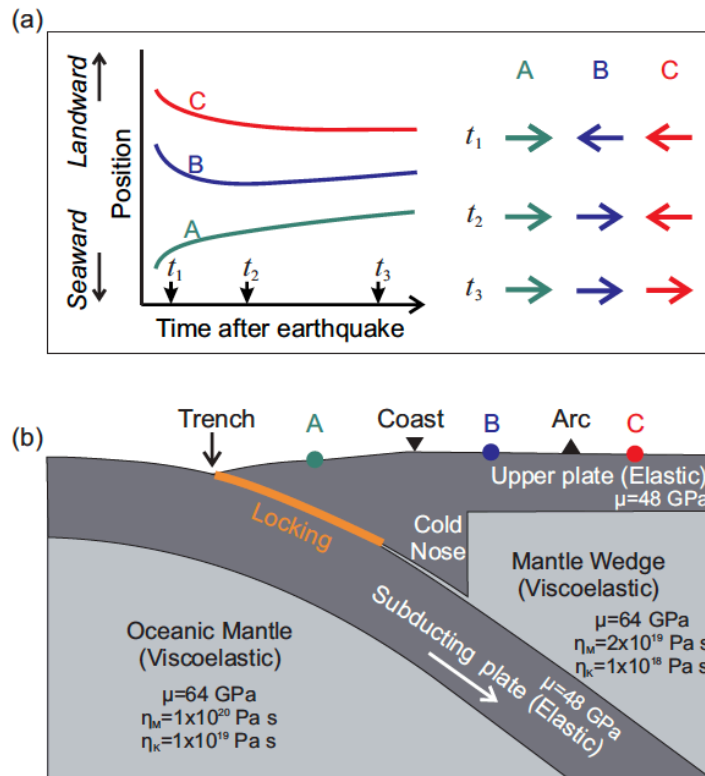


**Figure 4.1.** Schematic illustration of postseismic deformation of subduction earthquakes. (a) Modified from Sun et al. (2018). Left: Evolution of postseismic displacement at the three sites marked in (b). Right: Velocity direction of the three sites at three stages of the postseismic deformation, showing landward migration of the dividing boundary of opposing motion. (b) Structure and parameter values of the numerical model used in Sun et al. (2018) and this work to model the postseismic deformation of the 1960 Chile earthquake. Here  $\mu$  and  $\eta$  are rigidity and viscosity, respectively, and subscripts K and M denote the Kelvin and Maxwell components of the bi-viscous transient rheology. The Poisson's ratio is assumed to be uniformly 0.25.

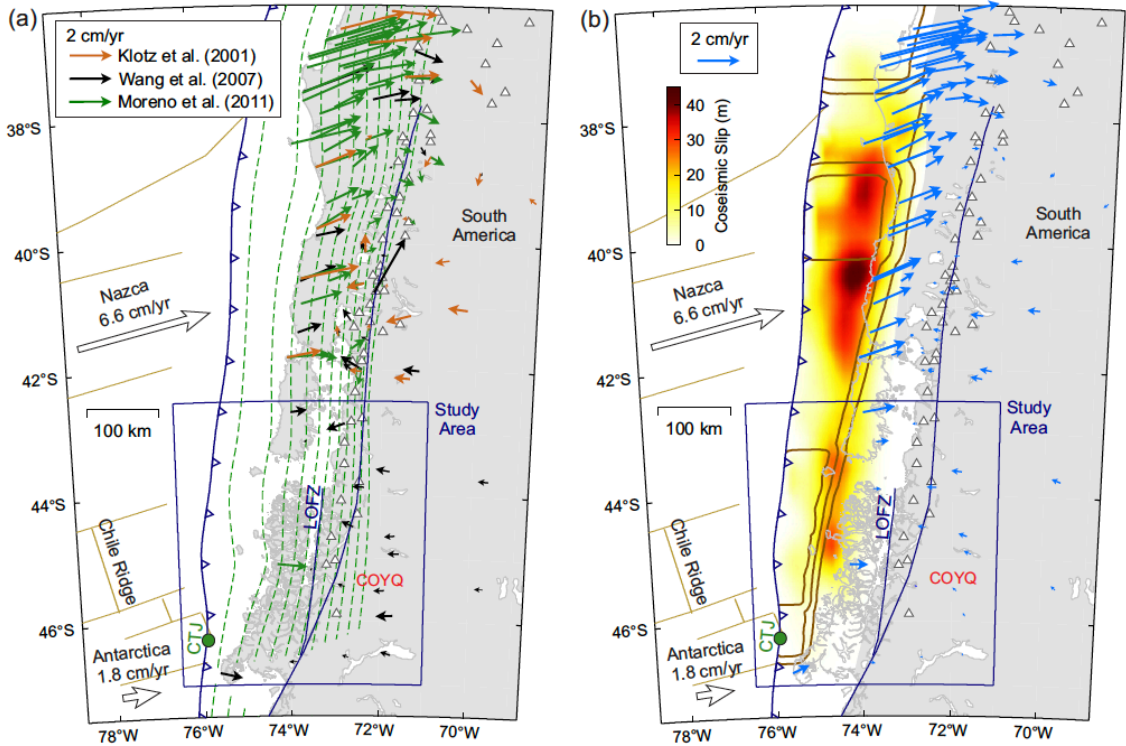


**Figure 4.2.** Observed and model-predicted GNSS site velocities. (a) GNSS velocities based on campaign surveys of 1994–1996 (Klotz et al., 2001), 1994–2005 (Wang et al., 2007), and 2002–2009 (Moreno et al., 2011). Displacement time series of site COYQ (red labelled) are shown in Figure 4.3. LOFZ, Liqueñe-Ofqui fault zone (Cembrano et al., 2002). CTJ, Chile triple junction. Sites west of LOFZ have been corrected for strike-parallel sliver motion following Wang et al. (2007). (b) Velocities 40 years after the 1960  $M_w$  9.5 Chile earthquake predicted by the postseismic deformation model of Sun et al. (2018). The 1960 coseismic slip distribution employed by this model was estimated by Moreno et al. (2009). In this figure and other map view figures in this paper, depth below sea level of the megathrust (interrupted by a slab window in the south) is contoured using dashed green lines at 10 km intervals, and slip deficit rates (Sun et al., 2018) are contoured using brown solid lines at 2 cm/yr intervals.

### 4.2.3. Geodetic Observations

#### 4.2.3.1. Two-decade displacement history at site COYQ

The GNSS velocities shown in Figure 4.2a were obtained with campaign measurements. There were few continuously monitoring stations in the 1990's and 2010's in South America in the latitudinal range of the 1960 Chile earthquake. Within our study area (south of 42.5°), COYQ was the only continuous station until 2009. The westward motion of COYQ since its establishment in 1997 is consistent with the general

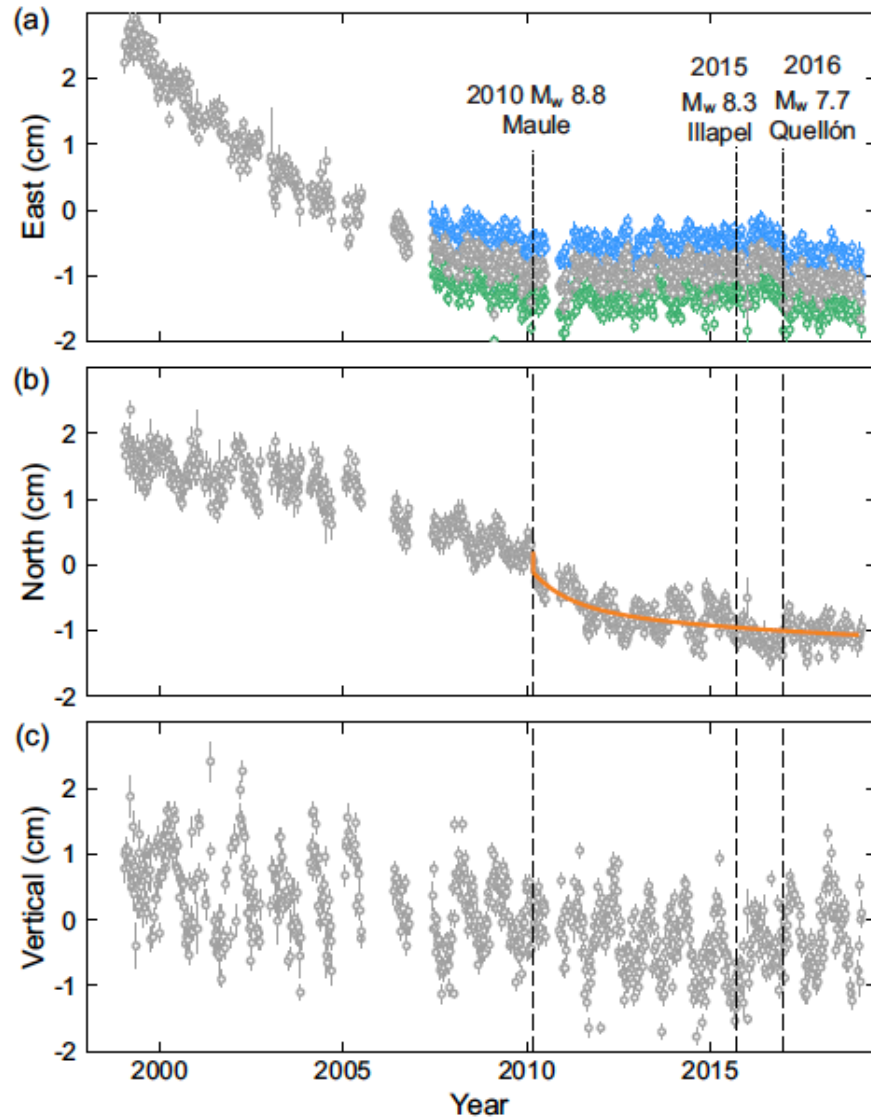
pattern of postseismic deformation of giant subduction earthquakes outlined in the Introduction. However, the temporal changes in its velocity have presented surprises.

Figure 4.3 shows weekly position solutions of COYQ over the past 20 yrs relative to the SA reference frame defined by minimizing the motion of the seven continuous GNSS sites shown in Figure 4.4. For data processing, we employ the GIPSY-OASIS v.6.4 software and use the precise point positioning (PPP) strategy (Zumberge et al., 1997) to generate daily position solutions. We use the Jet Propulsion Laboratory (JPL), Pasadena, orbits and clocks, as well as the widelane ambiguity products, to invoke single station ambiguity fixing (Bertiger et al., 2010). The resultant non-fiducial position solutions are then transformed into the ITRF2014 International Terrestrial Reference Frame, using a global Helmert seven-parameter transformation also provided by JPL along with the orbits and clocks. We have combined the daily solutions into weekly position estimates for Figure 4.3. One of us (MB) independently processed the same data using a procedure as previously described in Kendrick et al. (2001) and Brooks et al. (2003) and obtained nearly identical results. The most intriguing signal in the COYQ time series is the rapid deceleration of westward motion which began before 2010 (Figure 4.3a).

The COYQ site position time series shown in Figure 4.3 exhibit long-term trends with clear seasonal variations that are common in time series solutions of GNSS stations. Because the primary deformation signals examined in this work vary on a timescale of several years or decades, we choose to show the original time series in Figure 4.3 without removing the seasonal variations. The seasonal variations can be crudely quantified using sinusoidal functions as discussed in section 4.3.1, with parameters given in Table 4.1.

The motion of COYQ was affected by the coseismic and/or postseismic deformation of the 2010  $M_w$  8.8 Maule, 2015  $M_w$  8.3 Illapel, and the 2016  $M_w$  7.7 Quellón earthquakes to variable degrees ranging from negligible to significant. These three earthquakes were megathrust rupture events along the Nazca-South America subduction zone (Figure 4.4). As explained in section 4.3.1, we quantify coseismic jump and postseismic motion of COYQ caused by these events by fitting step and exponential functions to the time series, with parameters given in Table 4.1. For the purpose of this study, we focus on the east-west component, which is noticeably affected only by the





**Figure 4.3.** Time history of weekly position of GNSS site COYQ relative to the SA reference defined in this work (Figure 4.4) showing rapid velocity change in the early 21st century. Error bars represent 3 standard deviations. Locations of the three marked earthquakes are shown in Figure 4.4. For this display, no corrections are applied for seasonal variations and perturbations caused by the shown earthquakes (section 4.3.1). (a) East component, which is the focus of this work. Data after site repair in 2007 are shown in blue, grey, and green for three possible offset values 0, -4, and -8 mm, respectively, as explained in Section 4.2.3.1. (b) North component. Orange line highlights coseismic and postseismic effects of the 2010 Maule earthquake (Section 4.3.1). (c) Vertical component.

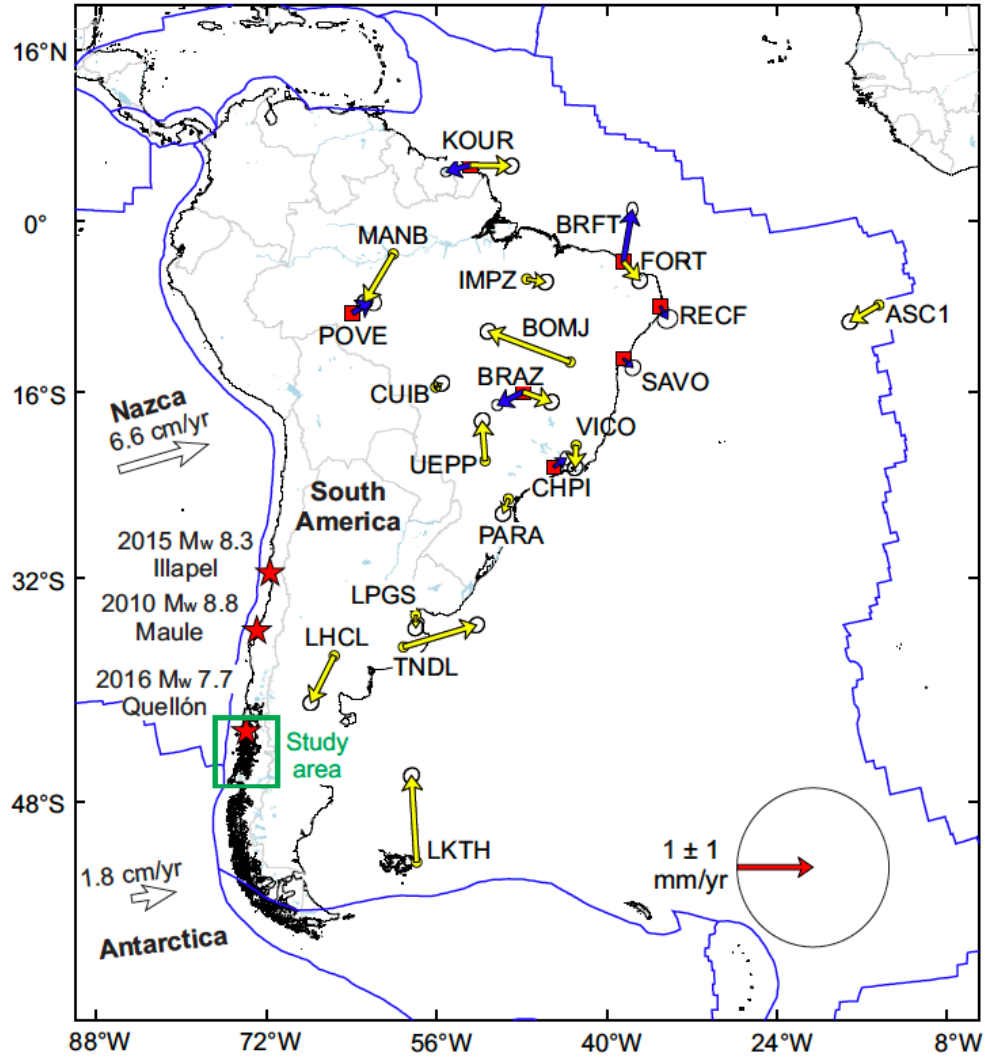


**Figure 4.4.** Definition of the South America (SA) reference frame. Red squares show stations used to define the SA reference in this work, and blue arrows show their motion in this reference frame. For comparison, stations used to define the SA reference by Wang et al. (2007) and their motion in that reference frame are shown with yellow circles and arrows, respectively. Blue lines outline plate boundaries, and light grey lines show international boundaries. Nazca and Antarctica plate velocities are from Argus et al. (2010). The three earthquakes marked with stars affected the COYQ time series to different degrees (Figure 4.3).

nearby 2016  $M_w$  7.7 Quellón earthquake. The earthquake caused a 3.85 mm coseismic westward jump of COYQ (Figure 4.3a and Section 4.3.1), but it has no impact on the main signal discussed in this paper, the deceleration of westward motion starting before 2010. The other two earthquakes occurred over 1000 km away. They had minor or negligible impact on the east-west component but somewhat greater impact on the north-

south component, in particular postseismic motion following the 2010 Maule earthquake as highlighted in Figure 4.3b (Table 4.1).

Instrument failure in 2005 and 2007 caused data gaps (Figure 4.3). The ensuing station repair in 2007 gave rise to the possibility of a phase centre shift. Upon visual inspection of the original east-west time series, there appears to be an upward (east) shift of about 4 mm in 2007 (Figure 4.3a). Despite lack of detailed documentation of the station repair in 2007, we address the uncertainties in this possible offset: We show the east-west time series with downward (west) offsets of 0, 4, and 8 mm in Figure 4.3a. As explained in Section 4.2.4.2, these uncertainties slightly affect some of our interpretation.

At the location of COYQ, the strongest postseismic effect of the 1960 earthquake is in the margin-normal direction, manifested as long-lasting seaward (westward) motion. However, the velocity of the westward motion (general slope of the curve) decreased rather quickly from a few years before 2010 and then began to show some eastward motion. The aforementioned data gaps and station repair during 2005–2007 should not affect the velocity estimates before 2005 and after 2007. There is indication that the southward motion of the site may have become slightly faster around 2005 (Figure 4.3b), but data gaps in 2005 and 2007 and the perturbation caused by the 2010 Maule earthquake make it difficult to decipher more quantitative information.

The velocity change at COYQ presents a serious scientific challenge. Viscoelastic earthquake cycle models based on realistic upper mantle viscosities predict that surface sites at distances of 200–300 km from the 1960 Chile earthquake rupture zone should continue to move trenchward (west) on a centennial time scale. Thus, in 2019, nearly 60 yrs post event, we would expect trenchward motion at COYQ to persist for three to four more decades. Furthermore, these models show that the eventual site velocity reversal from trenchward to landward should be very gradual (Hu et al., 2004; Wang et al., 2012; Sun et al., 2018). No reasonable model of viscoelastic stress relaxation can explain the observed early and rapid deceleration of trenchward motion and the apparent premature velocity reversal at COYQ.

#### 4.2.3.2. A regional increase in eastward velocity

Do the rapid deceleration and reversal of COYQ represent a regional change reflecting some actual subduction zone process or a local effect associated with site stability or small-scale geological processes? The question cannot be answered by observations from a single site. Therefore, we installed 4 new continuously recording GNSS stations in 2013–2015 (SAJA, BBAF, TRQ2, LSAR) (Figure 4.5a). The available data (with occasional gaps due to data dropouts) were processed until March 2019 (Table 4.2). We also processed daily position solutions computed by Blewitt et al. (2018) from 8 other stations in our study area (ESQU, FUTF, QLLN, RMBA, MELK, TPYU, BN11 and XPLO) (Figure 4.5a), spanning approximately 2010–2019 (Table 4.2). The data processing procedure for these 12 stations is the same as described in sections 4.2.3.1 and 4.3.1 for COYQ. We derived site velocities averaged over each station's data span using a simple linear model. In Figure 4.5, these new velocities are compared with the earlier velocities reported by Wang et al. (2007) based on campaign GNSS observations between 1994–2005.

Given variable data recording conditions that reflect differences in GNSS station equipment and monument design, the effects of large earthquakes in South America, different time spans of observation, and the crude manner by which dextral motion on the Liquiñe-Ofqui fault zone (LOFZ) was corrected (Wang et al., 2007), we refrain from detailed interpretations of the magnitudes and directions of individual velocity vectors shown in Figure 4.5a. However, it is remarkable that the 2010–2019 data collectively exhibit a regional increase in eastward velocity (or decrease in westward velocity) when compared to the 1994–2005 data (Figure 4.5c). Velocity values from individual sites that provided data during both time periods, or different sites from different periods but located at similar distances from the 1960 earthquake rupture zone, consistently show an increase in eastward velocity. Figure 4.5c only includes sites east of the 50 km depth contour of the plate interface (Hayes et al., 2012) for convenience of graphical display; however, stations west of the contour, such as MELK and QLLN, also show a similar eastward increase in site velocity. This systematic change strongly suggests that the striking velocity change visible in ~20 years of COYQ data (Figure 4.3a) reflects a regional increase in eastward velocity.

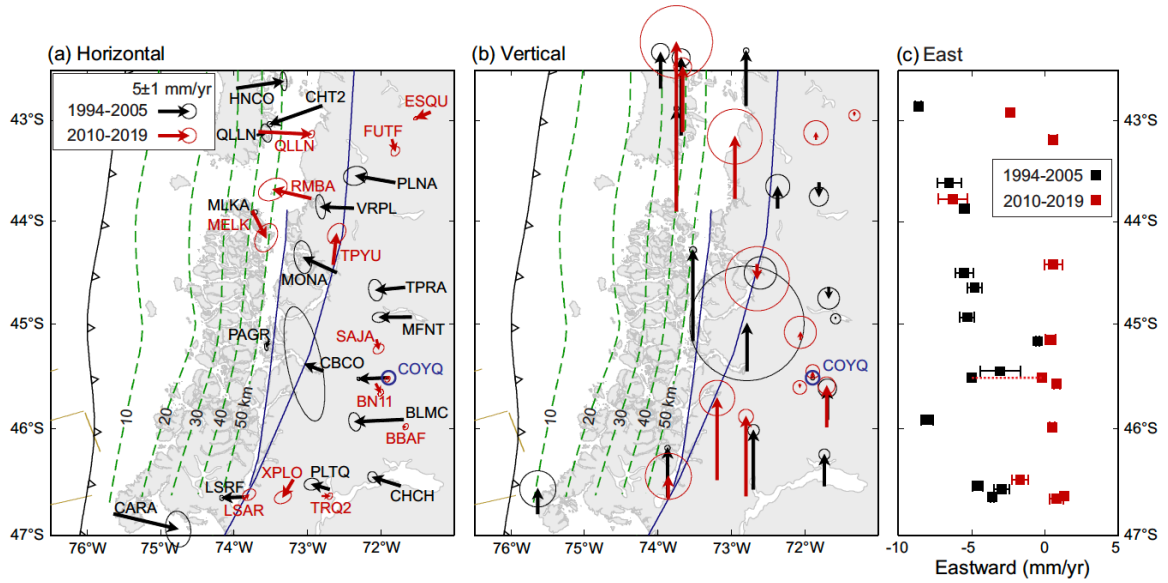


**Figure 4.5.** Regional change in GNSS velocity in the early 21st century. Error ellipse or bar represents 3 standard deviations. (a) New horizontal velocities (red) based on continuous GNSS data during 2010–2019 (Table 4.2) in comparison with the earlier velocities reported by Wang et al. (2007) based on 1994–2005 campaign data. At COYQ (blue circle), the earlier velocity was based on data until 2006, and the new velocity is based on data since 2013 after correction for the 2016 earthquake (Figures 4.3 and 4.6). As in Figure 4.2a, sites west of LOFZ (blue lines) have been corrected for strike-parallel sliver motion. (b) The vertical component. Same scale as in (a), with the error bar represented by a circle. (c) East component of the velocities as a function of latitude. The old and new COYQ values are connected with a red dotted line. For clarity, the plot only shows sites east of the 50 km depth contour of the plate interface.

The regional velocity change seen in Figure 4.5c cannot be an artefact due to differences between our stable SA reference frame and that of Wang et al. (2007). Most of the sites used by Wang et al. (2007) to define the SA reference are no longer operating, making it impossible to reproduce their results exactly. However, the comparison in Figure 4.4 demonstrates that their SA reference is practically identical to the SA reference we have defined in this work. Figure 4.4 shows velocity residuals for our sites in our new reference frame and also for their sites in their reference frame; the residuals would be identically zero if all the sites were on an ideally rigid plate and the GNSS data were error free. For sites used by both groups (KOUR or BRAZ) or located not very far apart (BRFT and FORT or CHPI and VICO), the vectorial difference between the two residuals is well below 1 mm/yr, and the directional difference is random. Therefore, the

reference frame difference between our work and Wang et al. (2007) cannot possibly cause the systematic eastward velocity shift of around 5 mm/yr in our study area (Figure 4.5c).

The regional change in Figure 4.5c cannot be an effect of the 2010  $M_w$  8.8 Maule earthquake (Figure 4.4). First, the velocity change at COYQ mostly occurred before 2010, and it is difficult to credit the notion that the site motions in our area – some 1000 km from the Maule rupture zone – were a slow preparatory phase of the Maule event. Second, in our study area, the influence of the co- and post-seismic motions due to the Maule earthquake is mainly in the north-south direction (Figure 4.3b).

The regional change shown in Figure 4.5c cannot be associated with changes in surface loading due to non-tectonic processes. Seasonal and multi-year surface and ground hydrological changes are known to induce both vertical and horizontal crustal motion (Amos et al., 2014; Kreemer and Zaliapin, 2018), commonly with much stronger effect on vertical than horizontal motions. Some of the GNSS sites in Figure 4.5, especially those near the coast and in the southern part of the study area, indeed exhibit faster vertical than horizontal motion. However, the velocity difference between the two measurement periods for nearby sites is generally much smaller on the vertical velocity component. If hydrological loading in this area (e.g., Rodell et al., 2018) is responsible for the faster vertical motion, it must be operating at a timescale long enough to affect both measurement periods similarly and cannot be the main cause for the rapid velocity change between the two periods which is predominantly horizontal. The effects of climatically induced changes in ice loading are more important south of our study region (Dietrich et al., 2010; Richter et al., 2016) and deserve more detailed research.

We thus must conclude that the sudden increase in eastward velocity in the early 21st century, both at COYQ and at a regional scale, is a true tectonic signal. Given reasonable ranges of mantle viscosity, it is not possible to explain either the rapidity of this velocity change, nor its early occurrence relative to modelling predictions, as part of the normal postseismic deformation process of the great 1960 Chile earthquake. We considered and dismissed as very unlikely complex transient or nonlinear Earth rheology that might be invoked to explain the observed rapid regional velocity change. The only remaining

possibility commensurate with the time scale of this observed velocity change is a change in the state of interplate locking. Thus, in the ensuing section we explore the effects of an increase in the degree of locking of the subduction megathrust in our study region that developed within a few years prior to 2010.

#### **4.2.4. Case for a recent increase in megathrust locking**

##### **4.2.4.1. The finite element model**

Our model builds on that of Sun et al. (2018) for the 1960 Chile earthquake, based on coseismic slip estimates from Moreno et al. (2009), except that we have slightly modified the model trench geometry to take advantage of a new algorithm we employ to generate the finite element mesh in the spherical Earth. However, we have also constructed a model that uses the newly published coseismic slip distribution of Ho et al. (2019) as detailed in the following section. We refer the reader to Sun et al. (2018) for model details but highlight the following points.

Our Earth model assumes that the mantle obeys the bi-viscous Burgers rheology and ignores along-strike variations associated with changes in the age and hence thermal state of the incoming plate. We also assume the viscosity values of the mantle wedge to be lower than those of the oceanic mantle by an order of magnitude to account for the presence of H<sub>2</sub>O and melts (Wang et al., 2012). Our mantle-wedge steady-state (Maxwell) viscosity is lower than that inferred by Lorenzo-Martín et al. (2006) mainly because of the presence of a subducting slab in our model. The material property values are shown in Figure 4.1b. The stagnant and cold part of the mantle wedge recognized in thermal and seismic studies (Wada and Wang, 2009; Abers et al., 2017) is represented by an elastic wedge corner (the “cold nose” in Figure 4.1b). The model accommodates actual fault and slab geometry and long-wavelength surface topography and approximately includes the effect of gravity using a prestress advection approach (Peltier, 1974).

#### 4.2.4.2. A model of enhanced locking

The rapidity and the spatial scale of the observed GNSS velocity change outlined in section 4.2.3 point to an increase in the locking of the megathrust, but the inferred degree of such an increase depends on the rate of crustal deformation prior to the increase. Models for the prior deformation rate are not very well constrained by the available sparse data, but they should fit the first few years of the east-west component of the observed COYQ time series (Figure 4.3a). We consider two options. First, in this section, we describe modelling of the prior crustal deformation rate using a postseismic deformation model based on the coseismic slip distribution of Ho et al. (2019). Second, in the next section, we describe modelling based on the slip distribution of Moreno et al. (2009) but also introduce a hypothetical slow slip event in order to match the prior rate of COYQ.

The great 1960 earthquake caused extensive crustal deformation and generated a large tsunami. Previous models of its coseismic slip distribution were based mainly on data reported by Plafker and Savage (1970) including field measurements of coastal uplift and subsidence and limited geodetic measurements (triangulation and levelling) before and after the earthquake. These models typically feature much less coseismic slip in the southern half of the rupture zone than in the northern half and very little slip near the trench (e.g., Moreno et al., 2009). Recently, Ho et al. (2019) incorporated numerous tsunami records in a new study of the 1960 earthquake slip and greatly improved offshore resolution. They reported that the northern and southern halves of the rupture zone underwent roughly the same amount of slip and that much slip occurred near the trench. We constructed a postseismic deformation model that invokes the coseismic slip distribution of Ho et al. (2019) but is otherwise the same as the model of Sun et al. (2018). Figure 4.6 shows postseismic deformation at COYQ predicted by this model, and Figure 4.7a shows its predicted regional deformation pattern, both in comparison to observations. We eschew a serious effort to fit GNSS site velocities near the southern boundary of the study area, where a slab window is well developed in association with the Chile ridge subduction (Russo et al., 2010a, 2010b) (Figure 4.7). Seismic velocities at asthenospheric depths in the slab window are  $\sim 3\%$  slower than expected, even relative to seismic velocity models that include a slow asthenosphere, indicating a warmer geotherm



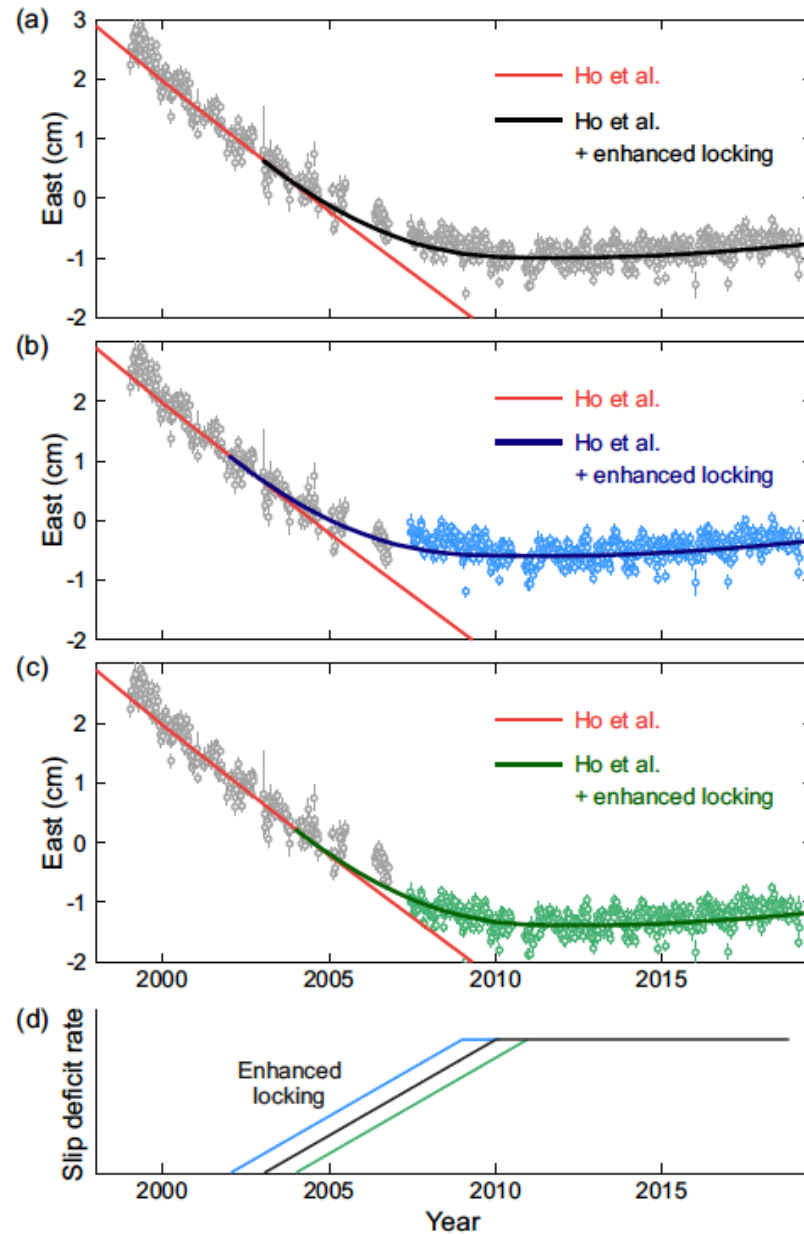


**Figure 4.6.** Rapid decrease in west velocity with respect to SA (Figure 4.4) at GNSS site COYQ in the early 21st century explained with a model of enhanced megathrust locking. The 3.85 mm offset caused by the 2016 earthquake visible in Figure 4.3a has been removed. The model-predicted site motion prior to the onset of the enhanced locking is based on a postseismic deformation model using the coseismic slip distribution of Ho et al. (2019) (Figure 4.7a). The distribution of enhanced locking is shown in Figure 4.7b. (a) Preferred model in which a 2007 correction of -4 mm is made to the GNSS data. (b) No 2007 correction is made. (c) The 2007 correction is -8 mm. (d) Schematic illustration of the event history and how the inferred onset time of the enhanced locking is affected by the 2007 correction. Blue, black, and green are for corrections 0, -4, and -8 mm, respectively.

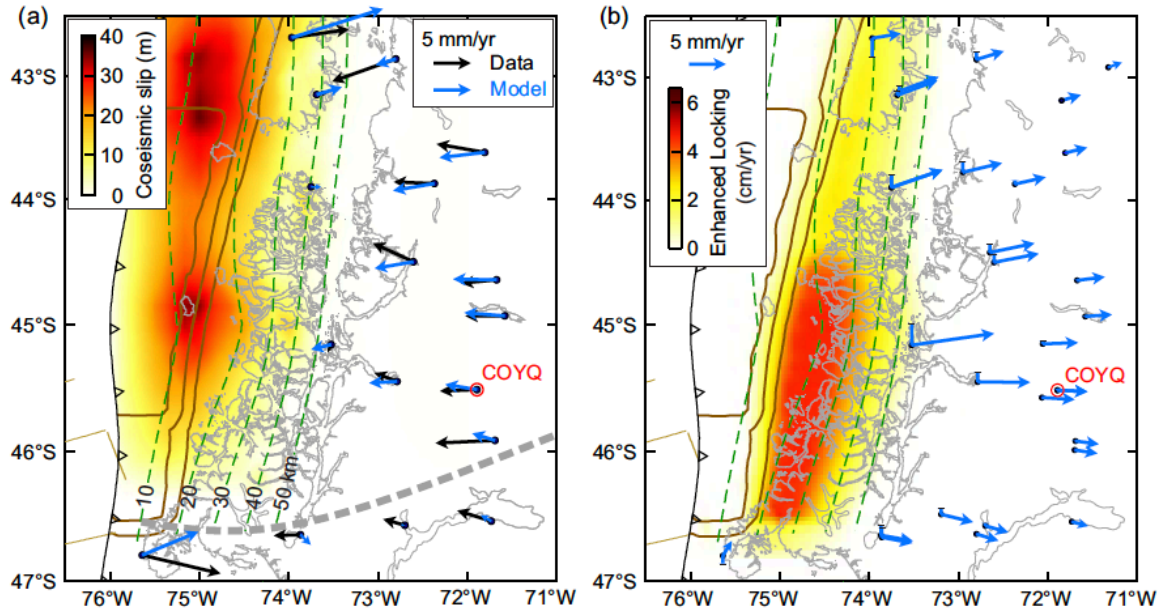


**Figure 4.7.** Regional map view of the enhanced locking model and site velocities prior to the locking increase. (a) Prior site velocities predicted by a viscoelastic postseismic deformation model that invokes the shown Ho et al. (2019) coseismic slip distribution but otherwise is the same as the model of Sun et al. (2018), in comparison with the 1994–2005 data. Large misfit at the southernmost sites is due to the use of a simplified model of along-strike uniform viscosity that ignores the presence of a slab window, of which the northern boundary is approximately delineated by the thick dashed line (Russo et al., 2010b). (b) Predicted velocity change, shown at all the GNSS sites, due to the assumed enhanced locking as seen in 2015 to explain the regional increase in eastward velocity shown in Figure 4.5c. The vertical component (bar at each site) is for visual comparison with the difference between the old and new values shown Figure 4.5b. See Figure 4.6 for possible onset times of the locking increase.

and lower viscosity. This lower viscosity associated with the slab window is most likely responsible for the observed high trenchward velocities of the southernmost GNSS sites. This effect cannot be addressed by our postseismic deformation model which for simplicity ignores along-strike viscosity variations, but it will be an important subject for future research.

The simplest way to introduce enhanced interplate locking is to assume that the locked zone of the megathrust became wider in the downdip direction during our observation period (Figure 4.7b). We assume that the degree of locking began to increase linearly with time in the first few years of the century (Figure 4.6) and reached a peak value  $> 50$  mm/yr in seven years in the southern portion of the study region (Figure 4.7b).

The enhanced locking (Figure 4.7b) can explain the regional increase in eastward velocity (Figure 4.5c). The incremental uplift predicted by this model (Figure 4.7b) is also consistent with the observed change (Figure 4.5b, the difference between the grey and red arrows). We do not attempt to fit the new velocity vectors shown in Figure 4.5a or the velocity change shown in Figure 4.5c site by site for the following reasons: (1) The distributions of GNSS stations that recorded the 1994–2005 and 2010–2019 velocities are different. (2) Most of the site velocities were based on observations of rather short time span (Table 4.2), and therefore uncertainties are large. (3) The GNSS stations were operational at different times, and thus site velocities are derived from somewhat different time periods between 2010–2019.

The regional data shown in Figure 4.5 illustrate the rapidity of the increase in eastward velocity but do not show when the increase began. The COYQ time series can provide information on the onset time of the enhanced locking, but the data suffers from uncertainties associated with the data gaps during 2005–2007. The offset correction added in 2007 (Section 4.2.3.1) affects the estimated onset time of the enhanced locking. Our preferred model shown in Figure 4.6a is based on adding an offset of 4 mm to the west (i.e., downward shift of the time series). In this model, the enhanced locking started in 2003. If the offset is zero or twice as large (Figure 4.3a), the model onset time will be 2002 (Figure 4.6b) or 2004 (Figure 4.6c), respectively. Regardless of the uncertainties in the onset time, enhanced downdip locking can readily explain the rapid increase in eastward velocity both at COYQ (Figure 4.6) and at the regional scale (Figures 4.5c and 4.7b).

#### **4.2.4.3. A model of slow slip followed by enhanced locking**

Given uncertainties in the coseismic slip models based on data prior to modern space geodesy, we also consider the postseismic deformation model of Sun et al. (2018) assuming validity of the coseismic slip distribution of Moreno et al. (2009). In this model, the westward velocity in the first few years of the century is smaller than observed at COYQ (Figure 4.8), but a higher velocity can be obtained by assuming that a slow slip event (SSE) occurred on the megathrust around the turn of the century. So-called long-

term SSEs lasting several years downdip of locked seismogenic zones have been detected in the Nankai, Mexico, Hikurangi, and Alaska subduction zones (e.g., Obara, 2011; Kostoglodov et al., 2010; Wallace and Beavan, 2010; Li et al., 2016). Low-frequency seismic tremor is usually abundant downdip of, but not in synchronization with, the long-term SSEs (Gao and Wang, 2017). We thus produced a model that includes such a long-term SSE just north of the CTJ, referred to as “Sun et al. + SSE” in Figure 4.8. The location of the assumed SSE slip patch is compatible with the tremor distribution during 2005–2007 determined by Ide (2012) using a method of envelope correlation (Figure 4.9a). Tremor sources during 2004–2007 had been determined by Gallego et al. (2003) using a source-scanning algorithm, although their location uncertainties are large (Figure 4.9a). The assumed SSE can produce a westward site velocity at COYQ prior to 2005 as high as observed.

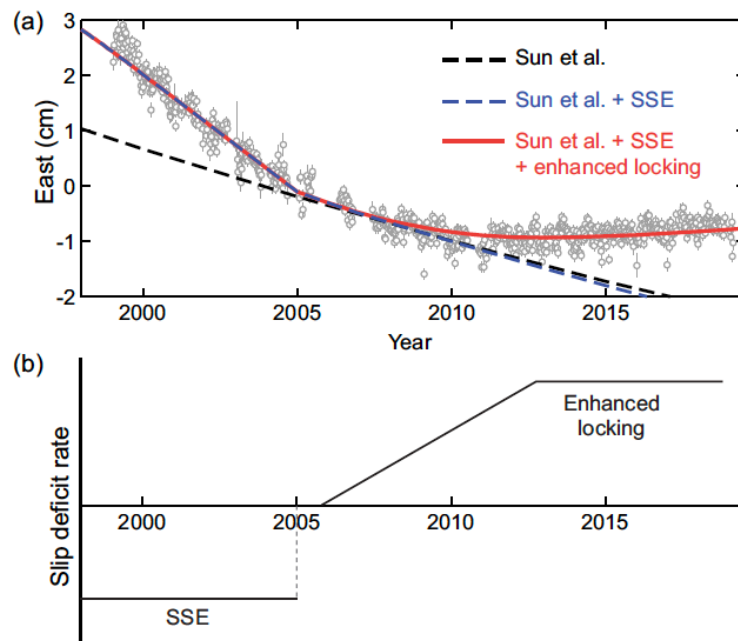


**Figure 4.8.** An alternative to the model of Figures 4.6 and 4.7 seen at COYQ: An SSE followed by enhanced locking. (a) Model predictions at COYQ in comparison with the time series shown in Figure 4.6a. The 1960 postseismic deformation model is that of Sun et al. (2018), but the faster motion before ~2005 is caused by an assumed slow slip event on the megathrust (Figure 4.9a). The distribution of locking increase is shown in Figure 4.9b. (b) Schematic illustration of the event history.

Our modelling shows that the termination of the SSE would not be sufficient to cause the observed regional increase in eastward site velocities shown in Figure 4.5c. It suffices to use one example, with an offset of 4 mm in 2007 as in Figure 4.6a, to illustrate this point. In this example, shown in Figure 4.8 as “Sun et al. + SSE + enhanced locking”, enhanced locking occurs after the SSE termination. Note that a fraction of the pre-2005 westward regional velocity is attributable to the SSE, and therefore the required increase in the degree of locking after SSE termination is less than that shown in the preferred model (Figure 4.6a). The distribution of the locking increase is shown in Figure 4.9b, together with resultant velocity increases in both the horizontal and vertical directions. Again, for reasons explained in Section 4.2.4.2, we focus on the overall pattern of the velocity increase but do not attempt to fit the observed values site by site.

#### **4.2.4.4. Discussion of enhanced locking**

A number of trade-offs are apparent even in our highly simplified modelling of the southern 1960 earthquake rupture region. For example, the assumption of a narrower zone of enhanced locking in the downdip direction would necessarily entail a large increase in slip deficit rate, and vice versa. If we invoke along-strike variations in mantle viscosity in the postseismic deformation model of the 1960 earthquake, we can obtain different background locking patterns for the megathrust. These trade-offs in model parameters are indicative of the non-uniqueness of the modelling results. Nonetheless, the range of results stemming from reasonable values of model parameters cannot explain our observations unless we introduce a sudden downdip increase in megathrust locking, regardless of other model details.

An increase in megathrust locking during postseismic or interseismic deformation is not an entirely novel concept. In fact, all SSEs must terminate by an increase in fault locking. However, our modelling demonstrates that the termination of a presumed SSE is insufficient – by itself – to cause the observed regional GNSS velocity change (Figure 4.8), and an additional increase in locking is required to match the observations (Figure 4.9).

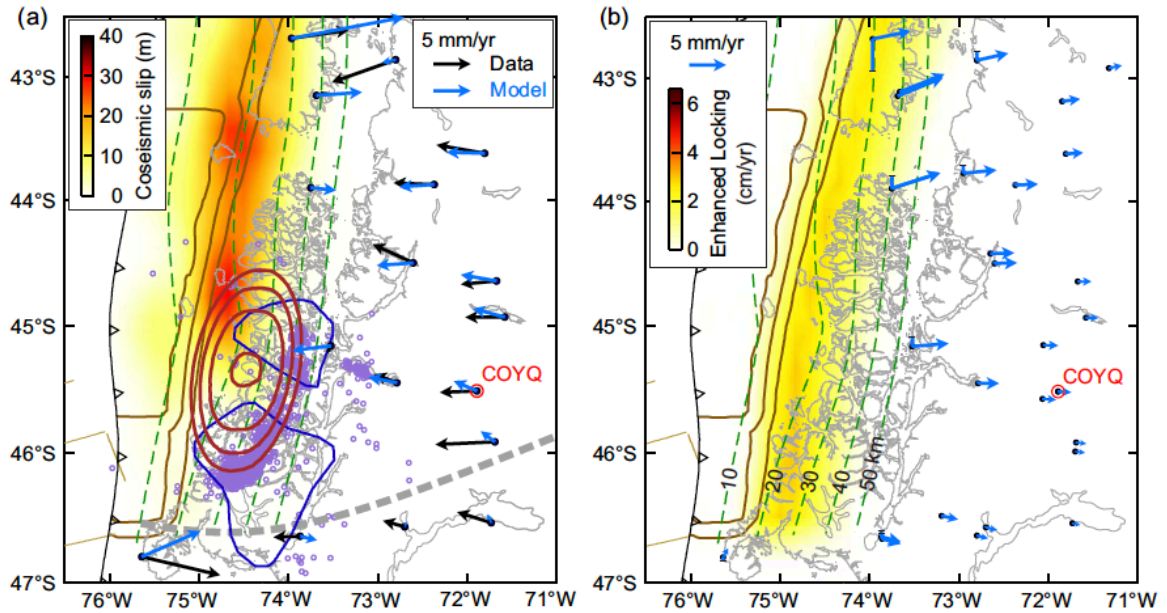


**Figure 4.9.** Regional map view of the model shown in Figure 4.8. (a) Velocities as seen in 2005 predicted with the Sun et al. model plus an elliptical SSE during 1998–2005, in comparison with the 1994–2005 data. Thick dashed line approximately delineates the northern boundary of a slab window (Russo et al., 2010b). Neglect of the slab window may explain the large misfit at the southernmost sites. The shown 1960 coseismic slip distribution is from Moreno et al. (2009) and was used in the Sun et al. (2018) model. The SSE (pure thrust) is contoured in red at 1 cm. Tectonic tremor sources during 2005–2007 reported by Ide (2012) are shown as purple circles, and the tremor areas for 2004–2007 reported by Gallego et al. (2003) are outlined using blue lines. (b) Similar to Figure 4.7b, but the enhanced locking is over a narrower depth range and assumed to have occurred after the SSE (Figure 4.8).

A sudden increase in landward GNSS velocities near a subduction zone has occasionally been reported elsewhere and interpreted to be caused by an increase in megathrust locking. The 2014  $M_w$  8.1 Iquique earthquake in northern Chile was reported to have increased GNSS velocities in an area south of the rupture (Hoffmann et al., 2018), although the velocity increase may alternatively be attributed to the diminishing viscoelastic postseismic deformation of the 2007  $M_w$  7.8 Tocopilla earthquake in the area. A small area in southernmost Cascadia was observed to accelerate after a nearby  $M_w$  6.8 earthquake in the incoming oceanic plate (Materna et al., 2019). In both cases, the GNSS velocity change is limited in the forearc area, and the inferred locking increase is thought to be a response to a preceding large earthquake. In contrast, the GNSS velocity change

reported in this paper extends far into the back arc, and there is no preceding large earthquake near the inferred zone of locking increase.

Enhanced downdip locking in our preferred model (Figures 4.6 and 4.7) can be viewed as a substantial deceleration of very long-lasting, slow, and deep afterslip following the 1960 earthquake. This is in contrast with a phenomenon recently observed at the Japan Trench subduction zone, where a large patch of the Pacific-Japan megathrust downdip of the then-future 2011  $M_w$  9 Tohoku-oki earthquake rupture exhibited accelerated slip for about a decade leading up to the 2011 earthquake (Mavrommatis et al., 2014; Yokota and Koketsu, 2015; Wang et al., 2018). The temporal changes in the megathrust locking state downdip of the main seismogenic zone without an apparent triggering mechanism seen in the Chile and Japan Trench subduction zones, either before or after a giant earthquake, presents new challenges to the understanding of fault mechanics and subduction zone dynamics. The spatial relationship between increased locking and tremor distribution (Figure 4.9) also deserves investigation.

Based on geological and geodetic observations around latitude 43.5°S, within the northern part of our study area, Melnick et al. (2018) proposed that the rupture zone of the 1960 earthquake in that area became increasingly locked from the time of the earthquake to 2005. If true, it can be regarded a slow healing process of the megathrust seismogenic zone. Our observation further south in the 1960 rupture region is an increase in megathrust locking that occurred further downdip and much later. Whether there is any tectonic link between the processes proposed in these two studies is a matter of conjecture.

#### 4.2.5. Conclusions

Viscoelastic relaxation of the stresses induced by the  $M_w$  9.5 1960 Chile earthquake causes geodetically observable deformation that may last a century. However, by analysing GNSS observations made 4 to 6 decades after the earthquake, we found a remarkable rapid change in site velocities in the early 21st century that cannot be explained by the viscoelastic postseismic deformation alone. We have thus proposed a conceptual model of enhanced megathrust locking and demonstrated the feasibility of the

concept using simple numerical models. The main conclusions of the work are as follows.

(1) A comparison of continuous GNSS data of 2010–2019 with campaign data of 1994–2005 reveals an unexpected systematic increase in landward (east) motion velocity over a large region covering the latitudinal range of the southern half of the great 1960 Chile earthquake rupture (Figure 4.5c). The only long-lived continuous GNSS site (COYQ), situated over 200 km from the 1960 rupture zone, indicates that this change rapidly occurred within a few years before 2010 (Figure 4.3a).

(2) The best, and likely the only, explanation for the rapid regional increase in the landward velocity is a widening of the megathrust locked zone in the downdip direction beginning around 2003 (Figures 4.6 and 4.7). The rapidity of the GNSS velocity change cannot be explained without invoking this increased locking, although details of the increase such as the width, magnitude, and along-strike distribution are affected by uncertainties in the 1960 earthquake coseismic slip model, mantle rheology, and the possible occurrence of SSEs. This temporal change in the megathrust locking state presents new challenges to the understanding of fault mechanics and subduction zone dynamics.

(3) The seaward (west) motion of COYQ, and to some degree of some other sites, prior to the enhanced locking is faster than predicted by previously published viscoelastic postseismic deformation models for the 1960 earthquake. The faster motion can be explained either by invoking greater coseismic slip in the southern part of the 1960 earthquake rupture area as recently reported by Ho et al. (2019) (Figure 4.6) or by assuming the occurrence of a long-term SSE (Figure 4.8). The latter is an arbitrary assumption but is compatible with observed distribution of tectonic tremor in this area (Gallego et al., 2013; Ide, 2012; Saez et al., 2019).

#### **4.2.6. Acknowledgements**

We thank Sergio Barrientos and Juan Carlos Baez of Universidad de Chile, for discussions and in-country support during fieldwork. Gonzalo Hermosilla of SERNAGEOMIN, Coyhaique, helped with field logistics. Sr. Pablo Keupuchur, Ian



Farmer, Don Gustavo, Senora Cristina López Quintana, and Sr. Raul Tarnovschi provided field support. Sra. Andreea Bahamonde Valenzuela, Sr. Adrián Escobar, and Sra. Gabriela Gomez, and the National Park Guards at Laguna San Rafael, all of the Chilean Corporación Nacional Forestal (CONAF), aided with permitting and logistics. Don Cirilo, Sr. Oscar Molinos, Sr. Artemio Perez, and Sr. Isidro Bastide Rivas gave permission to install and maintain GNSS stations on their properties. Hans van der Marel of TU Delft and George Slad, Greg Chavez, and Noel Barstow of IRIS PASSCAL helped design and operate station power setup. TUDelft provided equipment and most of the funding for the fieldwork. Reviewers Roland Bürgmann and Takeshi Sagiya provided valuable comments and suggestions.

### 4.3. Supplementary Material

#### 4.3.1. Decomposition of signals in COYQ time series

The COYQ time series displayed in Figure 4.3 include such signals as annual seasonal variations and earthquake perturbations that are largely extraneous to our results and do not affect our analysis. Nonetheless, for completeness, it is useful to quantify these signals. We use the following function to fit the COYQ position data to parameterize the various signals:

$$f(t) = C\sin(\theta) + D\cos(\theta) + \sum_{n=0}^N A_n + B_n(t - T_n) + E_n \left[ 1 - \exp\left(-\frac{t - T_n}{\tau_n}\right) \right] \quad (4.1)$$

where  $N$  is the total number of earthquakes considered ( $= 3$  in this work),  $C$ ,  $D$ , are amplitudes of the annual variations, and  $\theta$  includes time and the one-year period.  $T_n$  and  $A_n$  ( $n = 0, \dots, N$ ) are the time and value, respectively, of position reference or earthquake-induced offset, and  $E_n, \tau_n$ , are coefficients for the exponential term. The beginning phase of the time series is  $n = 0$ ; for example,  $T_0$  is the date of our first data point in 1999, and  $A_0$  is its reference position.  $n = 1, 2$ , and  $3$  denote the 2010 Maule, 2015 Illapel, and 2016 Quellón earthquakes, respectively. The signals most relevant to our purpose are represented mostly, but not fully, by the linear and exponential terms for  $n = 0$ .

Obviously, the geodynamic discussion in this paper is adequately based on the “raw” time series in Figure 4.3 and does not rely on any of the terms in the above function. A possible offset related to station repair in 2007 is not included in this function.

When fitting this function to the COYQ time series, we searched for the optimal values of  $\tau_n$  using an iterative scheme that minimizes the root-mean-square (RMS) misfit. We obtained the other parameters using a simpler least-squares fitting approach. The parameters thus determined are listed in Table 4.1. The only visually recognizable coseismic offset in Figure 4.3a is the westward jump  $A_3 = 3.85$  mm caused by the 2016 Quellón earthquake. It has been removed from the time series shown in Figures 4.6 and 4.8.

#### 4.3.2. GNSS Data

**Table 4.1.** Values of the parameters in equation 4.1 for the COYQ time series

$C$	$D$	$n$	$T_n$	$A_n$ (mm)	$B_n$ (mm/yr)	$E_n$ (yr)	$\tau_n$ (yr)
East component:							
0.1	-1.03	0	99JAN13	43.70	0.53	-43.70	5
		1	10FEB27	-0.80	0.22	0.20	0.5
		2	15SEP16	0.11	0.00	0.00	-
		3	16DEC25	-3.85	0.00	0.00	-
North component:							
0.85	1.37	0	99JAN13	0.00	-1.38	0.00	-
		1	10FEB27	-2.57	1.07	-6.42	0.5
		2	15SEP16	-2.82	0.00	0.00	-
		3	16DEC25	1.75	0.00	0.00	-
Vertical component:							
4.69	1.35	0	99JAN13	0.00	-0.58	0.00	-
		1	10FEB27	-1.91	0.00	0.00	-
		2	15SEP16	1.32	0.00	0.00	-
		3	16DEC25	3.27	0.00	0.00	-

**Table 4.2.** GNSS site velocities for the 2010–2019 measurements. (Part A)

Site	Lon (°)	Lat (°)	Height (m)	Rms_N (mm)	Rms_E (mm)	Rms_U (mm)	Vn (mm/yr)	Ve (mm/yr)	Vu (mm/yr)
BBAF	-71.7029	-45.9825	761.9	2	1.5	5.7	0.07	0.2	3.47
BN11	-72.0686	-45.572	308.2	2.8	2.2	5.8	-1.51	0.8	-0.63
COYQ	-71.8921	-45.5143	476.2	2	1.8	5.1	-0.29	-0.18	1.31
ESQU	-71.3234	-42.9171	589.4	2	2.1	5.8	-1.01	-2.39	-0.56
FUTF	-71.8484	-43.1905	381.9	1.6	1.6	6.2	-1.95	0.55	1.09
LSAR	-73.8586	-46.6617	28.2	2.5	2.4	10.1	4.24	0.76	3.71
MELK	-73.7492	-43.8967	20.1	2	1.1	7	2.05	2.27	27.84
QLLN	-73.6642	-43.1142	197.9	2.2	1.7	5.2	6.08	8.69	10.71
RMBA	-72.9533	-43.7751	30	2.5	3	5	7.99	-6.29	10.2
SAJA	-72.0604	-45.1498	461.8	1.6	1.6	7.4	-1.13	-0.38	-1.55
TPYU	-72.6481	-44.4209	28.9	1.9	1.8	7.7	5.08	0.56	-2.37
TRQ2	-72.8017	-46.6356	403.7	2	1.9	6.8	0.31	1.22	10.42
XPLO	-73.1948	-46.484	95.2	2.2	2.2	6.3	0.91	-1.7	13.5

**Table 4.2.** (Part B)

Site	SigVn (mm/yr)	SigVe (mm/yr)	SigVu (mm/yr)	CorNE	T_first (yymmdd)	T_last (yymmdd)	T_span (years)
BBAF	0.18	0.16	0.56	0.3	13-Feb-28	19-Mar-18	6.05
BN11	0.23	0.18	0.46	0.3	11-Jan-01	18-Jun-27	7.48
COYQ	0.19	0.18	0.45	0.3	13-Jan-03	19-Feb-11	6.11
ESQU	0.13	0.15	0.38	0.3	10-Feb-26	18-Sep-12	8.54
FUTF	0.32	0.3	0.82	0.3	15-Feb-20	18-Sep-12	3.56
LSAR	0.38	0.45	1.55	0.3	14-Apr-10	17-Jun-06	3.15
MELK	0.95	0.77	2.44	0.3	17-Jan-26	17-Dec-05	0.86
QLLN	0.26	0.22	0.6	0.3	13-Aug-01	18-Sep-12	5.12
RMBA	0.76	0.97	1.85	0.3	16-Feb-27	17-Jun-26	1.33
SAJA	0.29	0.29	1	0.3	15-Mar-11	18-Dec-04	3.74
TPYU	0.68	0.62	2.16	0.3	16-Mar-03	18-Apr-24	2.14
TRQ2	0.2	0.17	0.49	0.3	13-Mar-01	19-Mar-17	6.04
XPLO	0.44	0.57	1.19	0.3	16-Mar-09	18-Sep-12	2.51

## 5. Conclusions

This Ph.D. dissertation presents the results of several of my studies on earthquake cycle deformation in subduction zones. Through numerical modelling constrained by geodetic, geological, and other geophysical measurements, I investigate deformation processes in all three phases of subduction earthquake cycles, namely coseismic, postseismic and interseismic. The results provide new understanding of mantle rheology, effect of fault slip on crustal deformation, and heterogeneity in megathrust slip behaviour. A number of specific scientific conclusions for each study are already given in each chapter. Here I summarize the main scientific contributions as follows.

1. In Chapter 2, the intriguing observations of earthquake-induced tension cracks in the Chile-Peru forearc are explained by the viscoelastic rheology of near surface material that is reported in industrial studies. During the interseismic period, compressive stress is accumulated in the elastic upper plate but is relaxed in the near-surface material at the same time. Elastic rebound of the elastic upper plate during a great earthquake induces large tensile stress in the near-surface material exceeding its tensile strength and causes failure. The location of peak tensile stress is determined by the downdip termination of coseismic rupture. The permanent deformation represented by the tension cracks thus reflects heterogeneous crustal rheology and does not negate the elastic rebound theory.

2. Chapter 3 demonstrates that the commonly observed postseismic uplift near the volcanic arc is due to viscoelastic relaxation of earthquake-induced stress and is diagnostic of the presence of a cold and elastic forearc mantle wedge corner. Postseismic deformation models for the 1960  $M_w$  9.5 Chile, 2011  $M_w$  9 Tohoku-Oki, 2010  $M_w$  8.8 Maule, and 2007  $M_w$  8.4 Bengkulu earthquakes suggest that the presence of elastic wedge corner is irrespective of differences in the thermal regime. Because the presence of a cold mantle wedge corner strongly influences thermal and petrologic processes, the finding reported in this chapter makes a fundamental contribution to understanding subduction zone dynamics.

3. In Chapter 4, a rapid landward increase in GNSS velocity in the 21st century in the southernmost rupture area of the 1960  $M_w$  9.5 Chile earthquake is explained by a sudden downdip widening of the zone of megathrust locking. The  $\sim 5\text{mm/yr}$  increase in the

forearc and backarc region cannot be explained by the viscoelastic deformation process alone. This finding raises important new questions that challenge the present prevailing theoretical framework of megathrust slip behaviour. The potential of rapid change in the area of megathrust locking during the interseismic period has important implications to hazard assessment.

4. In the Appendix, we extend the study of subduction zone rheology to a non-tectonic process in southern Chile in which surface deformation is induced by glacial melting instead of earthquakes. GNSS data indicate that recent mass loss at the Northern and Southern Patagonian icefields, both situated above the Chile Ridge slab window, results in very fast ongoing uplift. Our numerical models indicate that the Maxwell viscosity in the north, younger part of the slab window is about one order of magnitude lower than that in the southern, older part. The results help to understand how tectonic history controls the along-strike heterogeneity of mantle rheology in the slab window setting.

## **Appendix. Along-strike viscosity variation in Chile slab window inferred from uplift due to recent glacial melting**

The material included in this Appendix, the rheological contrast within the Chile slab window at the southern terminus of the 1960 great Chile subduction earthquake, is an integral part of my PhD research. The main body of the Appendix is a journal article [Russo et al., 2021]. The Appendix consists of three sections, with Section A.1 describing basic information of the article, Section A.2 presenting the article itself, and Section A.3 providing the Supplemental Material accompanying the submitted article. This journal article is a second product of the international collaboration that produced the paper presented in Chapter 4 above. The team of scientists from the United States, Netherland, Romania, and Portugal carried our GNSS field work using their personal funds and processed the data. The leader of this team, Dr. R. M. Russo of University of Florida, is the lead author of this paper. I carried out most of the scientific interpretation, conceived the key idea of rheological contrast within the slab window, conducted all the modelling, and created all the figures in the main paper and all but one figures in the Supplemental Material. Given my primary contribution in this work and its importance to my PhD research, it is appropriate to include it in this dissertation. However, because I am not the lead author of the article, I include the article here as an Appendix.

### **A.1. Article Information**

#### **A.1.1. Author and Coauthor Contributions**

The author of this dissertation H.L. proposed the idea of rheological contrast, synthesized glacial mass loss history from the literature, carried out all the modelling, and drafted all (except Figure A.6) of the figures. K.W., R.M.R., and H.L. wrote the manuscript. Coauthors R.M.R. and K.W. led the collaboration. Coauthor J.H. wrote the numerical code and assisted in the modelling. Coauthor B.A. processed the GNSS data. Coauthor V.M. led the GNSS field work, joined by R.M.R., R.F., and B.A.. Coauthors T.J. and M.B. contributed to the conceptualization of the GIA process. All the authors contributed to editing the manuscript.

### A.1.2. Citation

Russo, R.M., Luo, H., Wang, K., Ambrosius, B., Mocanu, V., He, J., James, T., Bevis, M. & Fernandes, R. (2021). Lateral variation in slab window viscosity inferred from GNSS-observed uplift due to recent mass loss at Patagonia icefields. *Geology*. doi: 10.1130/G49388.1.

### A.1.3. Author's Names and Affiliations

Raymond M. Russo<sup>1</sup>, Haipeng Luo<sup>2</sup>, Kelin Wang<sup>3,2</sup>, Boudewijn Ambrosius<sup>4</sup>, Victor Mocanu<sup>5</sup>, Jiangheng He<sup>3</sup>, Thomas James<sup>3,2</sup>, Michael Bevis<sup>6</sup>, and Rui Fernandes<sup>7</sup>

<sup>1</sup> Department of Geological Sciences, University of Florida, Gainesville, Florida 32608, USA.

<sup>2</sup> School of Earth and Ocean Sciences, University of Victoria, Victoria, British Columbia, Canada, V8W 2Y2.

<sup>3</sup> Pacific Geoscience Centre, Geological Survey of Canada, 9860 West Saanich Road, Sidney, British Columbia, Canada, V8L 4B2.

<sup>4</sup> Faculty of Aerospace Engineering, Delft University of Technology, Kluyverweg 1, 2629 HS, Delft, The Netherlands

<sup>5</sup> Department of Geophysics, University of Bucharest, 6 Traian Vuia Street, RO-020956, Bucharest, Romania

<sup>6</sup> School of Earth Sciences, Ohio State University, 125 South Oval Mall, Columbus, Ohio 43210, USA

<sup>7</sup> University of Beira Interior, Instituto D. Luiz, Rua Marquês d'Ávila e Bolama, 6201-001 Covilhã, Portugal

Corresponding author: Victor Mocanu (vi\_mo@yahoo.com)

### A.1.4. Article Format

The text and figures included in Section A.2 are taken directly from the submitted article. The Supplemental Material for the article is given in Section A.3. Sections, figures, and tables in the original article have been renumbered to be compatible with the

chapter format of the dissertation. However, a very long table in the original Supplemental Material that lists numerical values of weekly GNSS data is not included here. Words that used American spelling as required by the journal have been changed to Canadian spelling in this Appendix. References cited in the article are included in the bibliography of the dissertation.

## **A.2. Lateral variation in slab window viscosity inferred from global navigation satellite system (GNSS)-observed uplift due to recent mass loss at Patagonia ice fields**

### **A.2.1. Abstract**

The geographical coincidence of the Chile Ridge slab window and the Patagonia ice fields offers a unique opportunity for assessing the effects of slab window rheology on glacial isostatic adjustment (GIA). Mass loss of these icefields since the Little Ice Age causes rapid but variable crustal uplift, 12-24 mm/yr around the North Patagonia Icefield, increasing to a maximum of 41 mm/yr around the South Patagonia Icefield, as determined from newly collected or processed geodetic data. We used these observational constraints in a three-dimensional Maxwell viscoelastic finite element model of GIA response above both subducting slab and slab window in which the upper-mantle viscosity is parameterized to be uniform with depth. We find that the viscosity of the northern part of the slab window,  $\sim 2 \times 10^{18}$  Pa s, is lower than the southern part by approximately an order of magnitude. We propose that this along-strike viscosity contrast is due to the late Cenozoic ridge subduction beneath the northern part of the slab window, which increases asthenospheric temperature and reduces viscosity.

### **A.2.2. Introduction**

The Patagonian slab window, which developed as a consequence of the subduction of the Chile ridge at the Chile triple junction (CTJ;  $\sim 46.5^\circ\text{S}$ ) (Figure A.1a) (Cande and Leslie, 1986; Breitsprecher and Thorkelson, 2009; Russo et al., 2010a; 2010b), lies beneath both the Northern and Southern Patagonia ice fields (NPI and SPI, respectively). However, the locus of Chile ridge subduction has generally migrated northward since



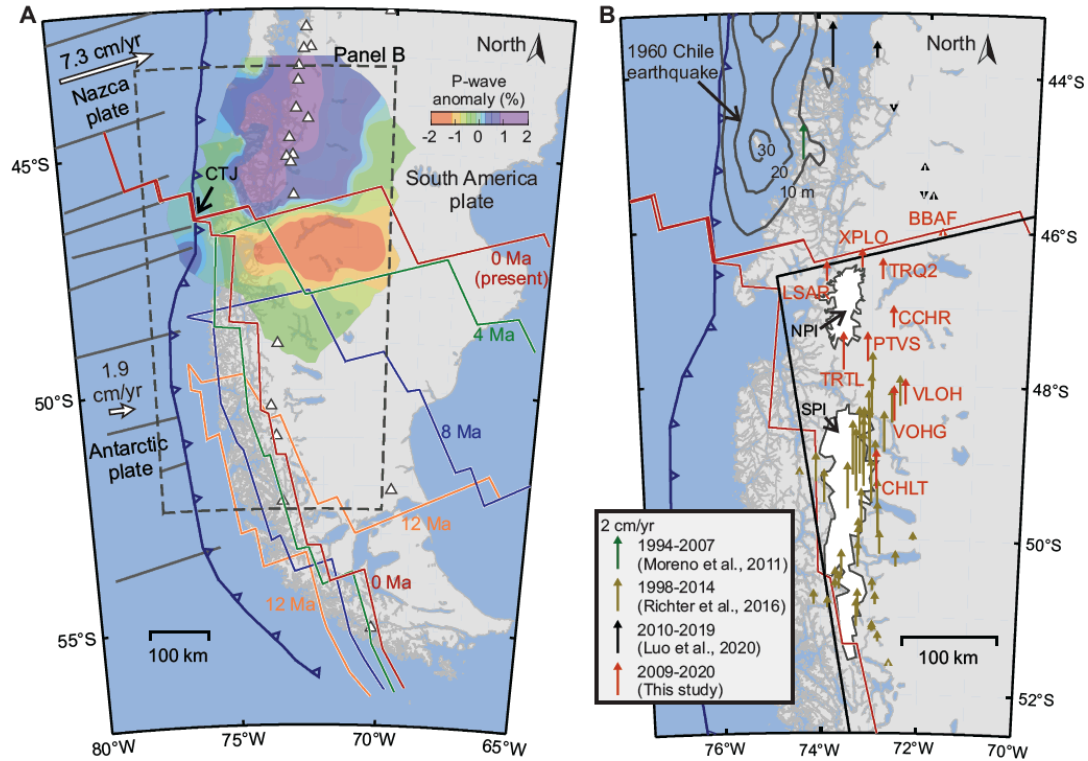


**Figure A.1.** (a) Regional tectonic setting and slab window history of Patagonia, based on Breitsprecher and Thorkelson (2009). P-wave velocity anomalies at 100 km depth (Russo et al., 2010a) show a contrast across the northern edge of the present slab window. Current plate motion vectors relative to South America plate from DeMets et al. (2010). Triangles are Holocene volcanos. CTJ: Chile triple junction. (b) GNSS uplift rates. Red arrows labelled with station names show values determined in this work (Table A.1). Coseismic slip of the 1960 M 9.5 earthquake (grey contours) from Ho et al. (2019). NPI and SPI—Northern and Southern Patagonia ice fields, respectively.

the Miocene to reach its current position (Figure A.1a), as various segments of the spreading ridge entered the Chile trench. We hypothesize that the asthenosphere in the more recently formed northern slab window is warmer and less viscous than that in the southern window. Testing this hypothesis is the goal of this investigation.

Published seismic imaging of the slab window, confined to north of  $\sim 49^\circ\text{S}$ , resolves P wave velocities at depths from 50-250 km that are  $\sim 6\%$  slower than those observed farther north (Figure A.1a; Russo et al., 2010a), implying low viscosities. Preliminary results from an ongoing seismic imaging project that samples a broader region suggest higher seismic velocities south of  $\sim 49^\circ\text{S}$  (Mark et al., 2020), although the results await confirmation by more complete analyses. Recent mass loss from the ice fields developed

above the slab window has led to glacial isostatic adjustment (GIA), and consequent rapid uplift rates are strong functions of upper mantle viscosity. Using a combination of new and existing global navigation satellite system (GNSS) observations of uplift as constraints for GIA models, we were able to examine the north-south viscosity contrast within the slab window.

### **A.2.3. Ice mass loss and its geodetic signature**

Patagonia ice mass loss histories from a number of studies (e.g., Rignot et al., 2003; Chen et al., 2007; Ivins et al., 2011; Willis et al., 2012a,b) (Figure A.5a in Supplemental Material) were synthesized by Lange et al. (2014) into a representative ice loss history (history B) which was translated into a history of uniform ice thinning rate shown in Figure A.2a. Lange et al. (2014) also constructed an alternative (history A), in which most of the ice loss occurred prior to the 1940's. We used history B as the primary loading history in our modelling, but we also tested the effects of history A. According to a number of studies, the ice thinning rates at the NPI and SPI on average were similar over the past few decades (Figure A.5b). For simplicity, we assumed the same thinning history for both ice fields for most of our modelling, but we also conducted additional tests to address uncertainties associated with this assumption.

GNSS data around the shrinking SPI reveal the fastest ( $> 40$  mm/yr) geodetically observed GIA uplift anywhere on Earth, consistent with rebound above an upper mantle with viscosity values of  $\sim 10^{18} - 10^{19}$  Pa s (Ivins and James, 1999, 2004; Lange et al., 2014; Richter et al., 2016). However, these results are only valid for the SPI, situated above the early-formed part of the slab window (Figure A.1b), and they derive from modelling that was either one-dimensional (1-D; laterally homogeneous), neglecting the subduction zone structure (Ivins and James, 2004; Lange et al., 2014), or two-dimensional along an east-west profile crossing the SPI (Klemann et al., 2007) and thus not designed to resolve along-strike rheological variability. To test the hypothesis of variable viscosities in the slab window, we installed new GNSS stations around the previously under-sampled NPI and processed other relevant GNSS data (Figure A.1b) to

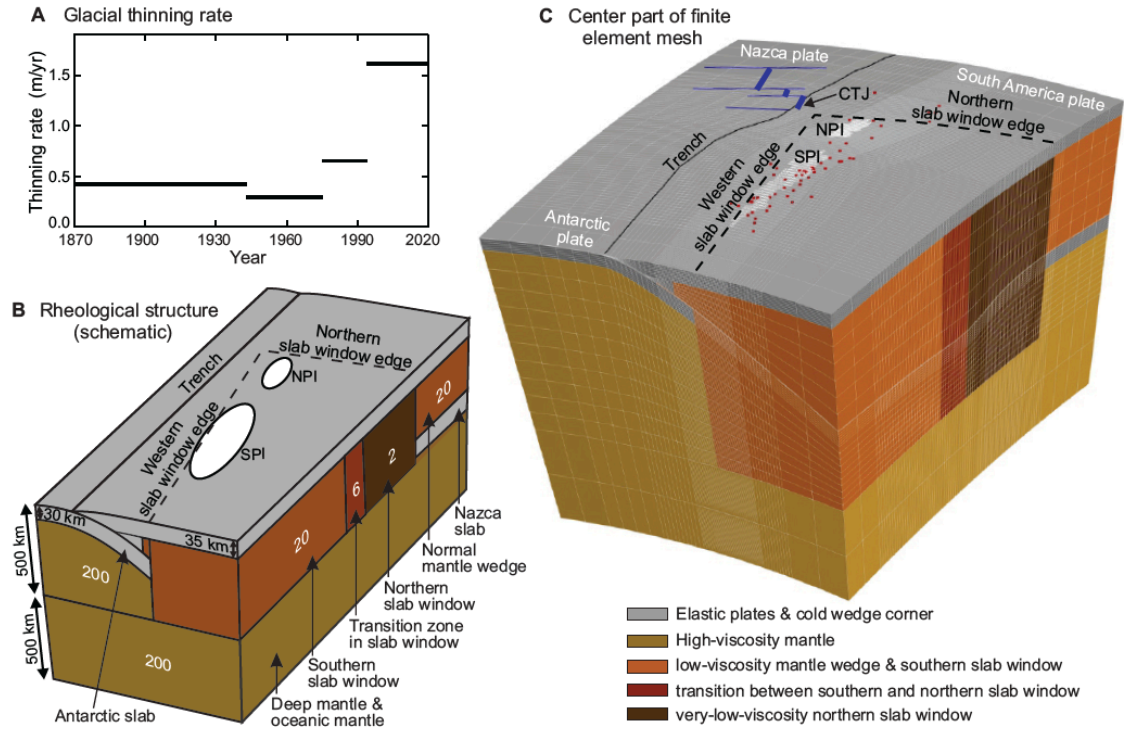


**Figure A.2.** (a) Ice thinning rate for both the Northern and Southern Patagonian ice fields (NPI/SPI) based on history B of Lange et al. (2014) (with a small extrapolation to 2020). See Figure A.5 for other proposed histories. (b) Model structure and rheology (not to scale). Viscosity (white numbers, in  $10^{18}$  Pa s) and thickness values are for the preferred model (Table A.2). (c) Center part of the finite element mesh. Each element has 27 nodes. Edges of the slab have been simplified to straight lines (dashed). See Figure A.1b for GNSS sites (red dots).

model the GIA response to the post-Little Ice Age mass loss histories of the entire Patagonian Icefield region.

New continuous GNSS observations at five sites installed by us in 2013 around the NPI (Figure A.1b), and post-2012 data from existing GNSS stations (Blewitt et al., 2018) were processed using the GipsyX software (Bertiger et al., 2020). We used the International Terrestrial Reference Frame 2014 (ITRF14, <https://www.iers.org/IERS/EN/DataProducts/ITRF/itrf.html>) and computed velocities (red arrows in Figure A.1b; Table A.1; Figure A.6) by fitting a linear trend plus seasonal terms. We also used campaign GNSS data from around the SPI (Richter et al., 2016) in our modelling. Potential differences in vertical rates (0–2 mm/yr) caused by the use of

different reference frames in processing of these GNSS data was at least an order of magnitude less than observed uplift rates in the region (Figure A.1b).

#### **A.2.4. Modelling GIA above the slab window**

##### **A.2.4.1. Along-Strike Viscosity Contrast**

We constructed finite element models with Maxwell viscoelasticity (see Supplemental Material) to assess the GIA-induced uplift in the presence of the Patagonia slab window (Figures A.2b, 2c). Previous modelling (Wang et al., 2007; Moreno et al., 2011; Luo et al., 2020) suggested that vertical deformation due to megathrust earthquake cycles is negligibly small at the NPI and SPI relative to the GIA deformation. To test the hypothesis stated in the Introduction, we allowed two areas of uniform viscosity within the slab window with a  $1^\circ$  wide zone of transition in between (Figures A.2b, 2c). With trial-and-error, we found the optimal location of the center line of the transition zone to be  $49^\circ\text{S}$ . Recent independent seismic imaging (Mark et al., 2020) supports this choice.

Our preferred model best fits the GNSS observations (Figures A.3a, 3b; Table A.2). A comparison with the 1-D model of Lange et al. (2014), incorporating model-predicted horizontal motion as well, is shown in Figure A.7. Errors in the GNSS data around SPI are large because they are campaign measurements (Richter et al., 2016), but the many campaign sites collectively provide good model constraints (Figure A.3b). The preferred model features a factor of 10 contrast in upper-mantle viscosity between the northern ( $2 \times 10^{18}$  Pa s) and southern ( $2 \times 10^{19}$  Pa s) parts of the slab window; the higher viscosity of the southern window is equivalent to “normal” mantle wedge outside the window (Figure A.2b) and is comparable to other active tectonic regions (e.g., James et al., 2009; Austermann et al., 2020). However, the viscosity beneath the NPI is decidedly low, comparable only to upper mantle viscosity in regions where Cenozoic ridge subduction has taken place (e.g., Larsen et al., 2005; Nield et al., 2014) or on Iceland, where a plume-spreading ridge interaction is ongoing (Pagli et al., 2007).

Models without an along-strike viscosity contrast in the slab window cannot simultaneously explain GNSS observations around both the NPI and SPI, as shown in Figure A.3c. The required along-strike viscosity contrast is insensitive to structural

details of the model. The upper plate thickness of 35 km in the preferred model is consistent with the seismic imaging study of Rodriguez and Russo (2020) and earlier GIA models (Ivins et al., 2011; Lange et al., 2014; Richter et al., 2016). Uniformly changing the upper plate thickness by 10 km would necessitate changing the slab-window viscosities by a factor of  $\sim 1.3$  but would not eliminate the large along-strike contrast. A model with upper plate thickness of 25 km in the north but 45 km in the south still requires a viscosity contrast of  $\sim 6.4$  times to fit the GNSS data (Figure A.8a). If we neglect the subduction zone and use a layered-Earth model including lateral variations, a large along-strike contrast in upper mantle viscosity is still required to fit the data (Figure A.8b). The Root-Mean-Square (RMS) values of the differences between model and GNSS uplift rates for the subduction zone models are shown in Table A.2 and various figures.

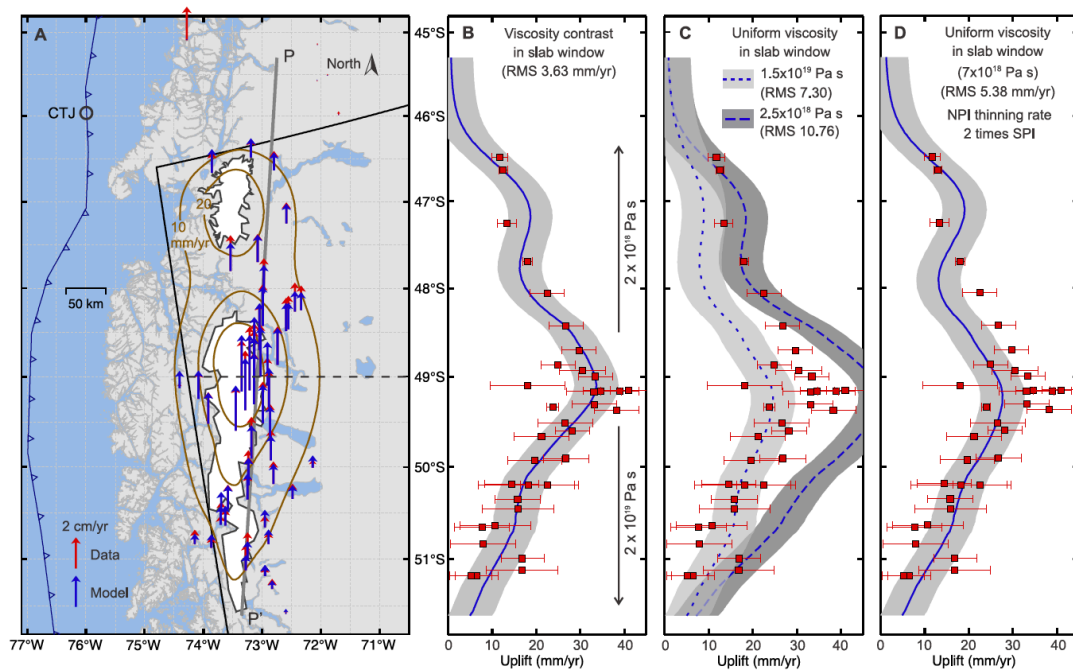


**Figure A.3.** (a) Uplift rates (brown contours) predicted by our preferred model (Figure A.2b) and GNSS observations. Dashed line marks the center of the  $1^\circ$  wide viscosity transition (Table A.2). (b) Model uplift rates in (a) along profile P-P' (blue curve)  $\pm 5$  mm/yr (grey area). GNSS values with  $1\text{-}\sigma$  error bars are from within 30 km of the profile. The viscosity values show the N-S contrast. (c) Model uplift rates but for models of uniform viscosity in slab window. (d) A model of uniform viscosity but with contrasting ice thinning rates (Figure A.5d). In (b), (c), and (d), RMS is Root-Mean-Square fit of model results to data (in mm/yr). NPI/SPI—Northern/Southern Patagonia ice fields.

#### A.2.4.2. Uncertainties in Ice Loss History

Uncertainties in the ice mass loss history affect the estimated degree of the along-strike viscosity contrast, but do not negate the requirement of the contrast. If we employ alternative ice-loss history A of Lange et al. (2014) (Figure A.5c), the required viscosity contrast is even greater than in the preferred model (Figure A.8c). Because the mass loss during recent decades in history A is slower than in history B by a factor of  $\sim 2.5$ , viscosities required to fit the GNSS uplift rates are much lower,  $10^{17}$  Pa s and  $3 \times 10^{18}$  Pa s for the northern and southern windows, respectively (Table A.2).

Although available observations are more consistent with both ice fields thinning at similar rates for most of the past few decades, there is indication that the NPI rate may have exceeded SPI since about 2010 (Figure A.5b). The effect of this recent change may be the largest source of uncertainty in our results, since our sensitivity tests (not displayed) indicate that post-2010 ice loss accounts for about 50% of the model-predicted uplift rates in Figure A.3a. However, the present large scatter of estimated thinning rates (Figure A.5b) does not allow a more quantitative assessment of this effect. Instead, we constructed a model with NPI ice thinning rate being always twice the SPI rate (Figure A.5c). The combined mass loss rate equals that of the preferred model (history B). With a uniform slab-window viscosity of  $7 \times 10^{18}$  Pa s, this model can marginally fit the overall GNSS pattern (Figure A.3d), but it systematically underestimates the uplift rates immediately north of  $49^\circ\text{S}$ , suggesting the need for a lower viscosity in this area.

#### A.2.5. Discussion

Geodetic data north and south of the CTJ clearly show the dominance of two different tectonic processes. North of the CTJ (Figure A.4), the plate margin is primarily affected by rapid subduction of the Nazca plate, and geodetic measurements there generally reflect both megathrust earthquake cycles and permanent deformation of South America due to convergence. Postseismic deformation due to the 1960  $M_w = 9.5$  megathrust earthquake is the prevalent geodetic signal observed (Plafker and Savage, 1970; Wang et al., 2007; Moreno et al., 2011; Luo et al., 2020). South of the CTJ, slow

subduction and limited Antarctic slab extent minimize the effects of plate convergence. Instead, available geodetic data predominantly reflect rapid GIA above the slab window. A contrast in mantle viscosity north and south of the CTJ has been suggested by previous seismic imaging (Figure A.1a). Our new results show that a viscosity contrast is present also within the slab window.

Although our model is the first GIA model to include 3-D subduction zone structure, it maintains the simplicity of the earlier 1-D model of Lange et al. (2014) in terms of mantle viscosity parameterization. The Lange et al. (2014) model (Figure A.7b) features an elastic plate overlying a uniform viscoelastic half space, and their preferred viscosity based on ice loss history B is  $8 \times 10^{18}$  Pa s. Richter et al. (2016) found that this model systematically underpredicted uplift rates in the northernmost SPI and overpredicted uplift rates for the rest of the SPI. We can readily verify this misfit pattern if we also assume a uniform viscosity of  $8 \times 10^{18}$  Pa s, which is between the two uniform values in Figure A.3c, for the slab window. This strongly supports the need to invoke non-uniform viscosity within the slab window (Figure A.3b).

Subduction of the actively spreading Chile Ridge advects hot upper mantle to shallow depths beneath South America. Models of thermal anomalies due to ridge subduction without active mantle flow – thus prescribing minimum temperature increases – show elevation of the geotherm by 150-250°C in the mantle wedge between depths of 40 and 150 km, and the thermal effects can persist for up to 30 m.y. (Iwamori, 2000). Temperatures in the subducted slab increase similarly, and adakitic slab melts are possible. Predicted temperatures in the asthenospheric slab window are likely to be significantly higher if modelling includes mantle flow advecting heat into the slab window (DeLong et al., 1979). Thus, both advected hot mantle of the spreading ridge and asthenospheric upwelling to fill the slab window bring the slab window upper mantle closer to solidus and decrease its viscosity. This effect is the strongest north of 49°S in the youngest part of the slab window (Figure A.1a).

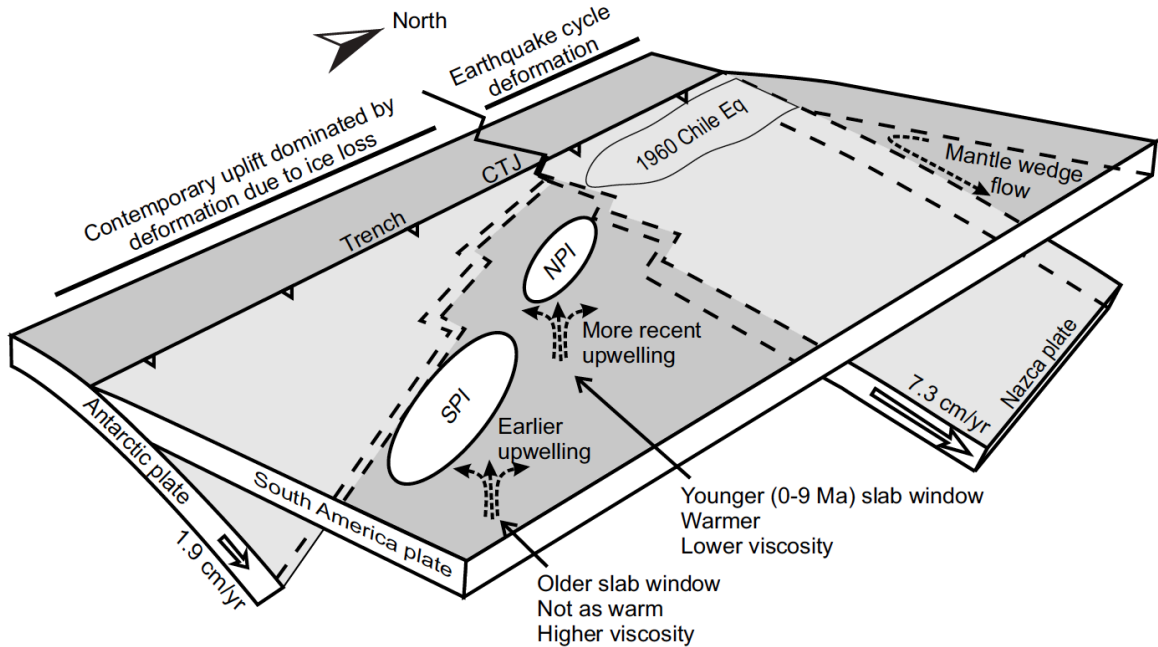


**Figure A.4.** Geodynamics and crustal deformation in the region of Chile triple junction (CTJ). North of CTJ, deformation is dominated by megathrust earthquake cycles. South of CTJ, GIA deformation at the Northern and Southern Patagonian ice fields (NPI and SPI, respectively) suggests a viscosity contrast of one order of magnitude between the two parts of the slab window. More complex 3-D flow due to slab window migration and other tectonic processes is not shown.

#### A.2.6. Conclusion

New GNSS data from the NPI area, in combination with published data from the SPI, allow us to test the hypothesis of an along-strike rheology contrast in the Patagonia slab window. Assuming ice thinning rates are the same for both icefields, GNSS-observed GIA uplift rates are consistent with an upper mantle viscosity of  $2 \times 10^{18}$  Pa s for the more recently developed, northern part of the slab window, and an order of magnitude higher in the southern part. This large, along-strike viscosity contrast is insensitive to details in assumed model structure. With a uniform viscosity, even an assumed NPI ice thinning rate twice that of the SPI cannot satisfactorily explain the GNSS data. Details of the ice thinning history of the most recent decade not addressed by our modelling may affect the degree, but not the presence, of the viscosity contrast. Our results support the notion that advected hot mantle due to ridge subduction and asthenospheric upwelling in



the wake of the northward migration of the Nazca edge of the slab window caused a viscosity decrease in the slab window.

### **A.2.7. Acknowledgements**

We thank Sergio Barrientos, Juan Carlos Baez of Universidad de Chile, Gonzalo Hermosilla of Servicio Nacional de Geología y Minería (Chile), Pablo Keupuchur, Ian Farmer, Don Gustavo, Cristina López Quintana, and Raul Tarnovschi for field support. Andrea Valenzuela, Adrián Escobar, Gabriela Gomez, the National Park Guards at Laguna San Rafael, Corporación Nacional Forestal (Chile), aided with permitting. Don Cirilo, Oscar Molinos, Artemio Perez, and Isidro Rivas gave permission to install GNSS stations. Hans van der Marel of Technische Universiteit Delft (TU Delft, Netherlands) and George Slad, Greg Chavez, and Noel Barstow of IRIS PASSCAL helped with the station power setup. TU Delft provided equipment and partial funding for the fieldwork. We thank Xin Zhou for collaboration in benchmarking our code and five anonymous reviewers for comments.

## **A.3. Supplemental Material**

### **A.3.1. Modelling Method**

Much glacial thinning has occurred at the NPI and SPI from the Little Ice Age maximum (~1870; Figure A.5). In our models, we calculate the viscoelastic response of glacial thinning from this time, with fixed glacial areas of 4000 km<sup>2</sup> and 13500 km<sup>2</sup> for the NPI and SPI, respectively (e.g., Davies and Glasser, 2012). We have also tested the effects of smaller mountain glaciers between the NPI and SPI and slightly to the east (Falaschi et al., 2017) but found their effects to be negligibly small and thus excluded them from our models for simplicity.

We use the spherical-Earth 27-node-finite-element code PGCviscl-3D that was developed by one of us (J. He) and described in Hu (2011) and Wang et al. (2012) to model the GIA-induced deformation. This code has been benchmarked against all available analytical solutions in GIA modelling and in viscoelastic postseismic

deformation modelling. For the spatial scale of this work, it would make no difference if a Cartesian code were used. The governing equation is,

$$\nabla \cdot \boldsymbol{\tau} - \nabla(\mathbf{u} \cdot \rho g \hat{\mathbf{r}}) = 0$$

where  $\boldsymbol{\tau}$  is the stress tensor,  $\mathbf{u}$  is the displacement vector,  $\hat{\mathbf{r}}$  is the radial unit vector,  $\rho$  is rock density, and  $g$  is gravitational acceleration. The second term in this equation is the contribution of advection of pre-stress (restoring force of isostasy) (Peltier, 1974).

Additional terms that describe the effects of buoyancy and self-gravitation in a more complete governing equation for GIA modelling (James, 1991) are important for modelling large loading areas and longer glacial history but are negligible for our problem at hand. The effect of ice thinning is identical to an upward pulling traction which is the product of the thinning rate, ice density ( $920 \text{ kg/m}^3$ ), and gravitational acceleration ( $9.8 \text{ m/s}^2$ ). We apply this traction at the surface.

Our model spans 50 latitudinal and longitudinal degrees, with the center portion shown in Figure A.2c, and a depth range of 0 – 1000 km. It is a variation of previous models of subduction earthquake cycles for the Chile margin (e.g., Wang et al., 2012; Sun et al., 2018; Luo et al., 2020). However, the effect of the Kelvin component of the bi-viscous transient rheology used in the earthquake models is negligibly small for the timescale of the GIA model of this work, and therefore here we assume a Maxwell rheology for the sub-lithospheric mantle. Otherwise, we keep the parameter structure simple and compatible with the earthquake models. Outside of the slab window, it features an elastic slab, upper plate, and “cold nose” of the mantle wedge (Luo and Wang, 2021), and the viscosity of the viscoelastic portion of the mantle wedge is an order of magnitude lower than the oceanic mantle. The rock density and Poisson’s ratio for the entire model are uniformly  $3300 \text{ kg/m}^3$  and 0.25, respectively. The rigidities for the elastic plates and viscoelastic mantle are 48 GPa and 64 GPa, respectively. The trench location is from Bird (2003), and the slab geometry is from Hayes et al. (2012) with an additional southward extrapolation to  $52^\circ\text{S}$ . The edges of the slab window are simplified from those of Breitsprecher and Thorkelson (2009) (Figure A.1b).

For simplicity and to be consistent with the resolving power of the GNSS observations, we ignore viscosity variations with depth except for a contrast across 500 km which approximates the mantle transition zone (Figure A.2b). The layer between the

upper plate and this depth in our model is a compromise between end-member options for the viscoelastic layer underlying the upper plate used in previous modelling of Patagonia GIA, such as a uniform half space (Ivins and James, 1999; Ivins et al., 2011; Lange et al., 2014; Richter et al., 2016) or a lower-viscosity asthenosphere of 100 – 200 km thick overlying higher-viscosity mantle (Ivins and James, 2004). Because of the rather small areas of the icefields and very short unloading history dealt with in this study, the exact thickness of this layer is of little importance; setting its bottom to 300 km or 700 km would yield similar results. In particular, it does not affect our investigation of the along-strike variations.

### A.3.2. Supplemental Figures and Tables

**Table A.1.** Newly obtained uplift rates for the ten continuous GNSS sites shown in red in Figure A.1a. \*

Site	Longitude (°W)	Latitude (°S)	Height (m)	Vu (mm/yr)	SigVu (mm/yr)	T_first (yymmdd)	T_last (yymmdd)	T_span (years)
PTVS	73.0785	47.6975	62.3	18.04	0.53	13-Feb-25	17-Mar-19	4.06
LSAR	73.8586	46.6617	28.2	12.42	1.03	14-Apr-09	19-May-21	5.11
BBAF	71.7029	45.9825	761.9	1.02	0.43	13-Feb-27	19-Nov-17	6.72
VLOH	72.3395	48.2481	451.0	15.87	0.47	13-Feb-24	18-Jul-21	5.4
TRQ2	72.8017	46.6356	403.7	13.04	0.45	13-Feb-28	19-Nov-19	6.72
XPLO	73.1948	46.484	95.2	11.77	0.92	16-Mar-07	19-Nov-02	3.65
VOHG	72.5566	48.4648	301.8	21.54	1.00	14-Feb-14	19-Dec-07	5.81
TRTL	73.541	47.8031	99.1	22.98	0.61	15-Mar-24	18-Apr-23	3.08
CHLT	72.8856	49.3405	485.4	24.00	0.50	09-Jun-04	19-Jun-17	10.04
CCHR	72.5907	47.253	189.8	13.42	1.07	17-Feb-09	20-Jan-13	2.93

\* The first five sites were installed for this study. Raw data for the bottom five sites are from Blewitt et al. (2018). Time series from these ten sites are shown in Figure A.6.

**Table A.2.** Slab window viscosity values (in  $10^{18}$  Pa s) and RMS fit to GNSS data in different models.\*

Model	Northern	Transitional (48.5°-49.5°)	Southern	Model RMS (mm/yr)	Figures
Preferred	2	6	20	3.64	Figure A.3a, 3b
Uniform: low viscosity	2.5	2.5	2.5	10.76	Figure A.3c
Uniform: high viscosity	15	15	15	7.30	Figure A.3c
Uniform viscosity: NPI thinning rate 2 times SPI	7	7	7	5.38	Figure A.3d
Variable upper-plate thickness	2.5	7	16	4.08	Figure A.8a
Mass loss history A	0.1	0.5	3	4.39	Figure A.8c

\*In all the models, the viscosity is  $2 \times 10^{20}$  Pa s for the oceanic mantle and deeper mantle and  $2 \times 10^{19}$  Pa s for the regular mantle wedge outside of the slab window (e.g., Figure A.2b).

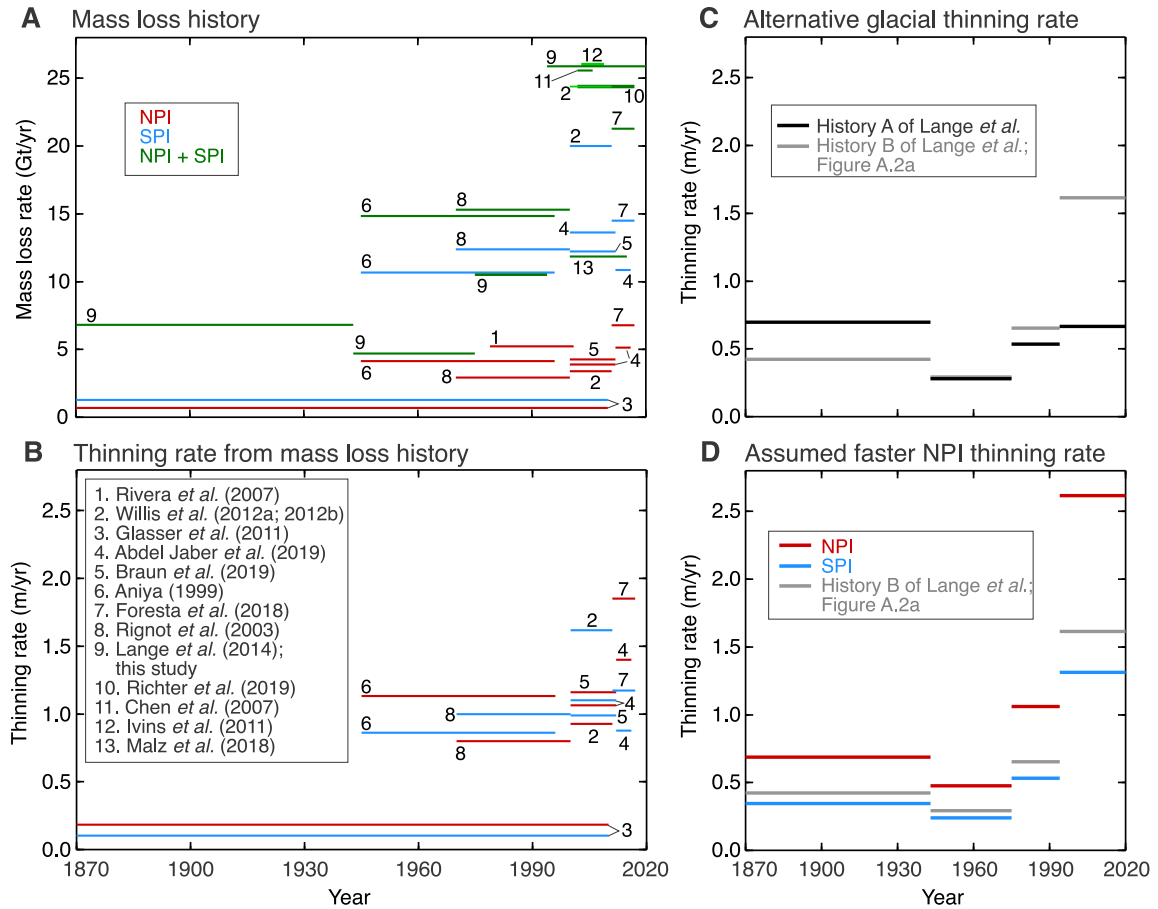


**Figure A.5.** (a) Ice mass loss history of NPI and SPI and/or their combination seen in the literature. Some of the studies provided rates only for one, or the total, of the two icefields. Lange *et al.* (2014) proposed two histories; only history B is shown here. (b) Ice thinning histories of NPI and SPI approximately translated from the mass loss histories in (a) for studies that provided estimates for both ice fields, assuming constant areas of 4000 and 13500 km<sup>2</sup> for NPI and SPI, respectively. (c) Uniform ice thinning history translated from history A of Lange *et al.* (2014) which is used for the test model shown in Figure A.8c, in comparison with that translated from history B (reproduced from Figure A.2a) which is used for the preferred model shown in Figures A.3a and 3b. (d) The ice thinning history used for the uniform-viscosity model shown in Figure A.3d, with the NPI thinning rate 2 times SPI, in comparison with the history used for the preferred model.

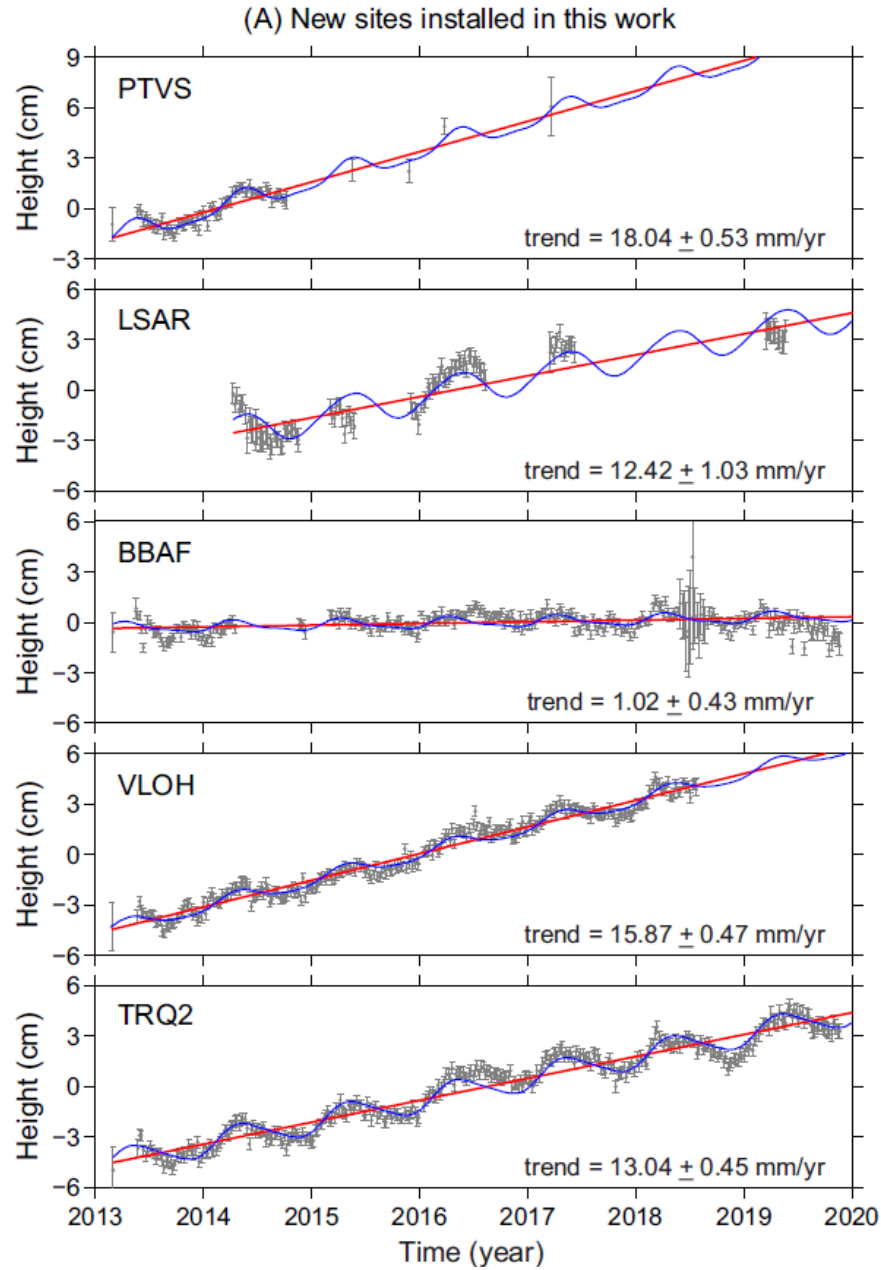


**Figure A.6.** Weekly vertical positions (grey circles) of the GNSS sites listed in Table A.1. Error bar represents 2.5 standard deviation. Blue curve is best-fit model that includes the linear trend and annual and semiannual cycles. The linear trend, which provides the uplift rate of each site shown in Table A.1, Figure A.1a, and Figure A.3, is also shown using a red line. The data are processed using the GipsyX software (Bertiger et al., 2020) in the ITRF14 reference frame following the procedure described in Luo et al. (2020). (a) Data from the five new sites established in this study. (b) Five existing sites from Blewitt et al. (2018).

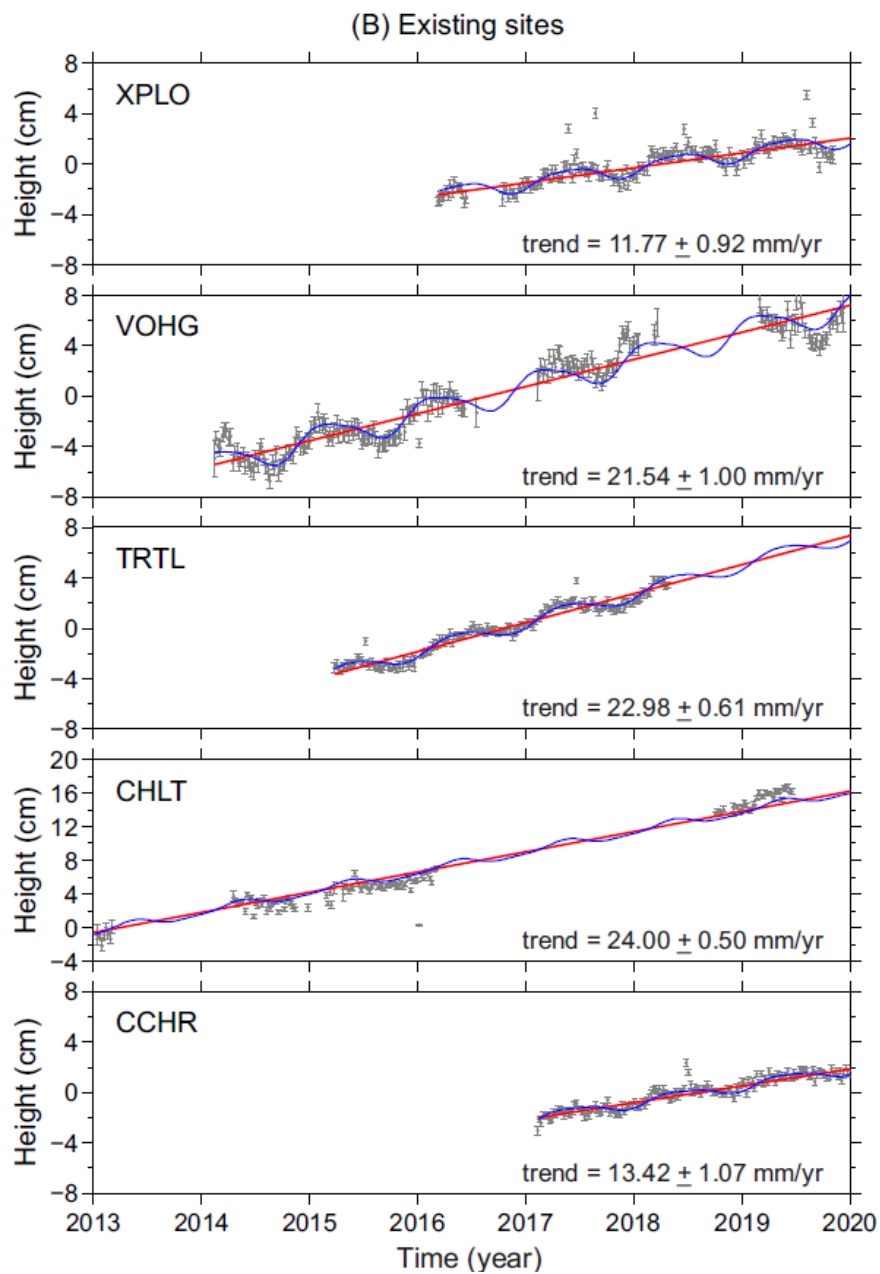
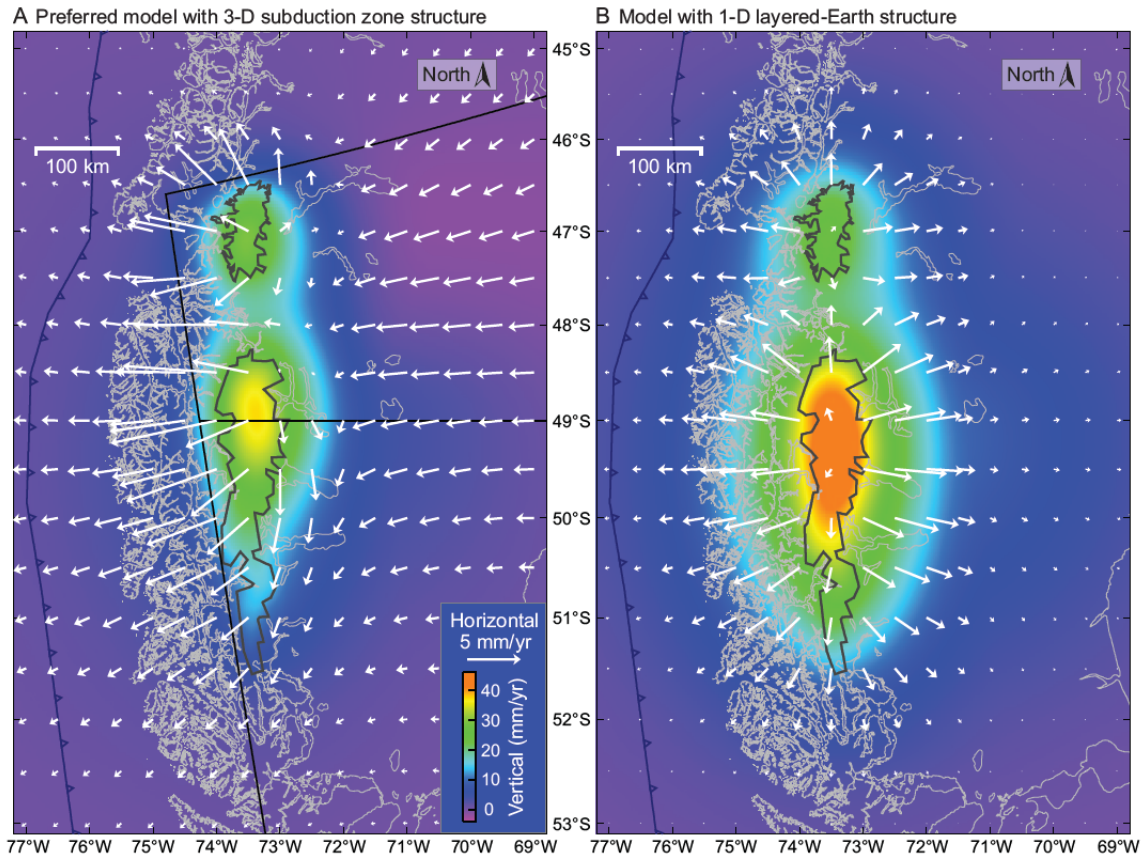
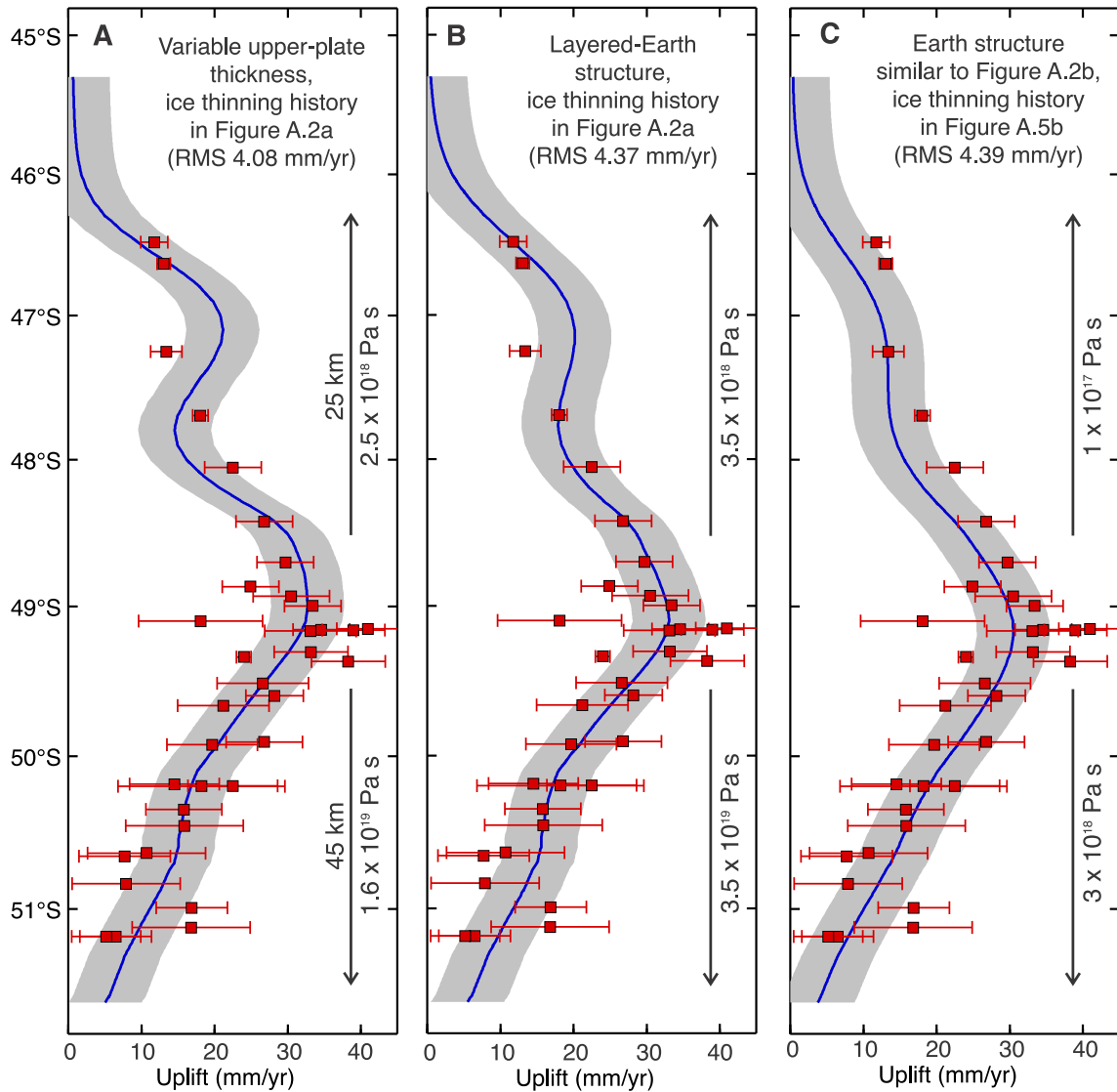


Figure A.6. Continued.



**Figure A.7.** (a) Vertical as well as horizontal deformation predicted by the 3-D preferred model shown in Figure A.3a (Table A.2). (b) Deformation predicted by the 1-D model of Lange et al. (2014) (also used by Richter et al. (2016)), featuring a 35 km thick elastic layer overlying a viscoelastic half space with viscosity  $8 \times 10^{18}$  Pa s. In the 1-D model, deformation is symmetric with respect to the load center. In the 3-D model, less viscous upper-mantle material exhibits faster flow toward the load center in response to ice melting, causing systematic motion of the overlying elastic layer in the direction of the more viscous part of the mantle. In (a), the dominant westward motion reflects the contrast between the high-viscosity oceanic mantle and low-viscosity mantle wedge, and the presence of a pronounced southward component reflects the N-S viscosity contrast in the slab window.





**Figure A.8.** Three test models that can roughly explain the GNSS data using the viscosity values shown for the northern and southern parts of the slab window. Model uplift rates (blue curve) are along profile P-P' of Figure A.3a  $\pm$  5 mm/yr (grey area). GNSS values with 1- $\sigma$  error bars are from within 30 km of the profile. (a) A model with a N-S contrast of 20 km in upper-plate thickness as shown. (b) A layered-Earth model. The pattern of N-S variations in viscosity is similar to that of Figure A.2b except for the lack of a subducting slab. (c) Similar to the preferred model (Figure A.2b) but with the ice thinning history shown in Figure A.5b based on history A of Lange et al. (2014).

## Bibliography

- Abdel Jaber, W., Rott, H., Floricioiu, D., Wuite, J., & Miranda, N. (2019). Heterogeneous spatial and temporal pattern of surface elevation change and mass balance of the Patagonian ice fields between 2000 and 2016. *The Cryosphere*, 13(9), 2511-2535.
- Abers, G. A., Van Keken, P. E., & Hacker, B. R. (2017). The cold and relatively dry nature of mantle forearcs in subduction zones. *Nature Geoscience*, 10(5), 333-337.
- Agard, P., Plunder, A., Angiboust, S., Bonnet, G., & Ruh, J. (2018). The subduction plate interface: rock record and mechanical coupling (from long to short timescales). *Lithos*, 320, 537-566.
- Amos, C. B., Audet, P., Hammond, W. C., Bürgmann, R., Johanson, I. A., & Blewitt, G. (2014). Uplift and seismicity driven by groundwater depletion in central California. *Nature*, 509(7501), 483-486.
- An, C., Sepúlveda, I., & Liu, P. L. F. (2014). Tsunami source and its validation of the 2014 Iquique, Chile, earthquake. *Geophysical Research Letters*, 41(11), 3988-3994.
- Aniya, M. (1999). Recent glacier variations of the Hielos Patagónicos, South America, and their contribution to sea-level change. *Arctic, Antarctic, and Alpine Research*, 31(2), 165-173.
- Argus, D. F., *et al.* (2010). The angular velocities of the plates and the velocity of Earth's centre from space geodesy. *Geophysical Journal International*, 180(3), 913-960.
- Aron, F., Allmendinger, R. W., Cembrano, J., González, G., & Yáñez, G. (2013). Permanent fore-arc extension and seismic segmentation: Insights from the 2010 Maule earthquake, Chile. *Journal of Geophysical Research: Solid Earth*, 118, 724–739. doi:10.1029/2012JB009339.
- Austermann, J., Chen, C. Y., Lau, H. C., Maloof, A. C., & Latychev, K. (2020). Constraints on mantle viscosity and Laurentide ice sheet evolution from pluvial paleolake shorelines in the western United States. *Earth and Planetary Science Letters*, 532, 116006.
- Bai, Y., Cheung, K. F., Yamazaki, Y., Lay, T., & Ye, L. (2014). Tsunami surges around the Hawaiian Islands from the 1 April 2014 North Chile Mw 8.1 earthquake. *Geophysical Research Letters*, 41, 8512–8521. doi:10.1002/2014GL061686
- Baker, A., Allmendinger, R. W., Owen, L. A., & Rech, J. A. (2013). Permanent deformation caused by subduction earthquakes in northern Chile. *Nature Geoscience*, 6(6), 492.
- Barbot, S. (2020). Frictional and structural controls of seismic super-cycles at the Japan

- trench. *Earth, Planets and Space*, 72, 1-25.
- Barrientos, S. E., & Ward, S. N. (1990). The 1960 Chile earthquake: inversion for slip distribution from surface deformation. *Geophysical Journal International*, 103(3), 589-598.
- Barrientos, S. E., Plafker, G., & Lorca, E. (1992). Postseismic coastal uplift in southern Chile. *Geophysical Research Letters*, 19(7), 701-704.
- Bertiger, W., Desai, S. D., Haines, B., Harvey, N., Moore, A. W., Owen, S., & Weiss, J. P. (2010). Single receiver phase ambiguity resolution with GPS data. *Journal of Geodesy*, 84(5), 327-337.
- Bertiger, W., *et al.* (2020). GipsyX/RTGx, a new tool set for space geodetic operations and research. *Advances in Space Research*, 66(3), 469-489.
- Bevis, M., Bedford, J., & Caccamise II, D. J. (2020). The art and science of trajectory modelling. In *Geodetic Time Series Analysis in Earth Sciences* (pp. 1-27). Springer, Cham.
- Bird, P. (2003). An updated digital model of plate boundaries. *Geochemistry, Geophysics, Geosystems*, 4, 1027.
- Blewitt, G., Hammond, W. C., & Kreemer, C. (2018). Harnessing the GPS data explosion for interdisciplinary science. *Eos*, AGU 99.
- Bostock, M. G., Hyndman, R. D., Rondenay, S., & Peacock, S. M. (2002). An inverted continental Moho and serpentinization of the forearc mantle. *Nature*, 417(6888), 536-538.
- Braun, M. H. *et al.* (2019). Constraining glacier elevation and mass changes in South America. *Nature Climate Change*, 9(2), 130-136.
- Breitsprecher, K., & Thorkelson, D. J. (2009). Neogene kinematic history of Nazca–Antarctic–Phoenix slab windows beneath Patagonia and the Antarctic Peninsula. *Tectonophysics*, 464(1-4), 10-20.
- Brooks, B. A., *et al.* (2003). Crustal motion in the Southern Andes (26°–36° S): Do the Andes behave like a microplate? *Geochemistry, Geophysics, Geosystems*, 4(10), 1085.
- Brown, L., Wang, K., & Sun, T., 2015. Static stress drop in the Mw 9 Tohoku-oki earthquake: Heterogeneous distribution and low average value. *Geophysical Research Letters*, 42, 10,595–10,600. <https://doi.org/10.1002/2015GL066361>
- Bürgmann, R., & Dresen, G. (2008). Rheology of the lower crust and upper mantle: Evidence from rock mechanics, geodesy, and field observations. *Annual Review of Earth and Planetary Sciences*, 36, 531-567.

- Cande, S. C., & Leslie, R. B. (1986). Late Cenozoic tectonics of the southern Chile trench. *Journal of Geophysical Research: Solid Earth*, 91(B1), 471-496.
- Cembrano, J., Lavenu, A., Reynolds, P., Arancibia, G., López, G., & Sanhueza, A. (2002). Late Cenozoic transpressional ductile deformation north of the Nazca–South America–Antarctica triple junction. *Tectonophysics*, 354(3-4), 289-314.
- Chang, C. & Zoback, M. D. (2009). Viscous creep in room-dried unconsolidated Gulf of Mexico shale (I): Experimental Results. *Journal of Petroleum Science and Engineering*, 69, 239-246.
- Chen, J. L., Wilson, C. R., Tapley, B. D., Blankenship, D. D., & Ivins, E. R. (2007). Patagonia icefield melting observed by gravity recovery and climate experiment (GRACE). *Geophysical Research Letters*, 34, L22501.
- Cifuentes, I. L. (1989). The 1960 Chilean earthquakes. *Journal of Geophysical Research: Solid Earth*, 94(B1), 665-680.
- Davies, B. J., & Glasser, N. F. (2012). Accelerating shrinkage of Patagonian glaciers from the Little Ice Age (~ AD 1870) to 2011. *Journal of Glaciology*, 58(212), 1063-1084.
- DeLong, S. E., Schwarz, W. M., & Anderson, R. N. (1979). Thermal effects of ridge subduction. *Earth and Planetary Science Letters*, 44(2), 239-246.
- Delouis, B., Nocquet, J. M., & Vallée, M. (2010). Slip distribution of the February 27, 2010 Mw= 8.8 Maule earthquake, central Chile, from static and high-rate GPS, InSAR, and broadband teleseismic data. *Geophysical Research Letters*, 37(17), L17305.
- DeMets, C., Gordon, R. G., & Argus, D. F. (2010). Geologically current plate motions. *Geophysical Journal International*, 181(1), 1-80.
- de Waal, J. A. & Smits, R. M. M. (1988). Prediction of reservoir compaction and surface Subsidence: Field application of a new model. *SPE Formation Evaluation*, 3(2), 347-356. doi:10.2118/14214-PA.
- Dietrich, R., Ivins, E. R., Casassa, G., Lange, H., Wendt, J., & Fritsche, M. (2010). Rapid crustal uplift in Patagonia due to enhanced ice loss. *Earth and Planetary Science Letters*, 289(1-2), 22-29.
- Dudley, J. W., Myers, M. T., Shew, R. D., & Arasteh, M. M. (1998). Measuring compaction and compressibilities in unconsolidated reservoir materials by time-scaling creep. *SPE Reservoir Evaluation & Engineering*, 1(5), 430-437. doi:10.2118/51324-PA
- Duputel, Z., et al. (2015). The Iquique earthquake sequence of April 2014: Bayesian modeling accounting for prediction uncertainty. *Geophysical Research Letters*,

42(19), 7949–7957.

- Ericksen, G. E. (1981). Geology and the origin of the Chilean nitrate deposits. *Geological Survey Professional Paper 1188*, U. S. Government Printing Office, Washington, D. C., 37 pp.
- Falaschi, D., Bolch, T., Rastner, P., Lenzano, M. G., Lenzano, L., VECCHIO, A. L., & Moragues, S. (2017). Mass changes of alpine glaciers at the eastern margin of the Northern and Southern Patagonian Icefields between 2000 and 2012. *Journal of Glaciology*, 63(238), 258-272.
- Feng, L., Hill, E. M., Banerjee, P., Hermawan, I., Tsang, L. L., Natawidjaja, D. H., Suwargadi, B. W., & Sieh, K. (2015). A unified GPS-based earthquake catalog for the Sumatran plate boundary between 2002 and 2013. *Journal of Geophysical Research: Solid Earth*, 120(5), 3566-3598.
- Findley, W. N., Lai, J. S., & Onaran, K. (1976). Creep and Relaxation of Nonlinear Viscoelastic Materials with an Introduction to Linear Viscoelasticity, Dover Publications, North-Holland, 380 pp.
- Freed, A. M., Hashima, A., Becker, T. W., Okaya, D. A., Sato, H., & Hatanaka, Y. (2017). Resolving depth-dependent subduction zone viscosity and afterslip from postseismic displacements following the 2011 Tohoku-oki, Japan earthquake. *Earth and Planetary Science Letters*, 459, 279-290.
- Foresta, L., *et al.* (2018). Heterogeneous and rapid ice loss over the Patagonian Ice Fields revealed by CryoSat-2 swath radar altimetry. *Remote Sensing of Environment*, 211, 441-455.
- Furukawa, Y. (1993). Depth of the decoupling plate interface and thermal structure under arcs. *Journal of Geophysical Research: Solid Earth*, 98(B11), 20005-20013.
- Gallego, A., Russo, R. M., Comte, D., Mocanu, V., Murdie, R. E., & VanDecar, J. C. (2013). Tidal modulation of continuous nonvolcanic seismic tremor in the Chile triple junction region. *Geochemistry, Geophysics, Geosystems*, 14(4), 851-863.
- Gao, X., & Wang, K. (2014). Strength of stick-slip and creeping subduction megathrusts from heat flow observations. *Science*, 345(6200), 1038-1041.
- Gao, X., & Wang, K. (2017). Rheological separation of the megathrust seismogenic zone and episodic tremor and slip. *Nature*, 543(7645), 416-419.
- Glasser, N. F., Harrison, S., Jansson, K. N., Anderson, K., & Cowley, A. (2011). Global sea-level contribution from the Patagonian Icefields since the Little Ice Age maximum. *Nature Geoscience*, 4(5), 303-307.
- Govers, R., Furlong, K. P., Van de Wiel, L., Herman, M. W., & Broerse, T. (2018). The geodetic signature of the earthquake cycle at subduction zones: Model constraints on

- the deep processes. *Reviews of Geophysics*, 56(1), 6-49.
- Gusman, A. R., Murotani, S., Satake, K., Heidarzadeh, M., Gunawan, E., Watada, S., & Schurr, B. (2015). Fault slip distribution of the 2014 Iquique, Chile, earthquake estimated from ocean-wide tsunami waveforms and GPS data. *Geophysical Research Letters*, 42(4), 1053-1060.
- Hagin, P. N., & Zoback, M. D. (2004a). Viscous deformation of unconsolidated sands—Part 1: Time-dependent deformation, frequency dispersion, and attenuation. *Geophysics*, 69(3), 731-741.
- Hagin, P. N., & Zoback, M. D. (2004b). Viscous deformation of unconsolidated sands—Part 2: Linear viscoelastic models. *Geophysics*, 69(3), 742-751.
- Hayes, G. P., Wald, D. J., & Johnson, R. L. (2012). Slab1.0: A three-dimensional model of global subduction zone geometries. *Geophysical Research Letters*, 117, B01302, doi:10.1029/2011JB008524.
- Hayes, G. P., Herman, M. W., Barnhart, W. D., Furlong, K. P., Riquelme, S., Benz, H. M., Bergman, E., Barrientos, S., Earle, P.S., & Samsonov, S. (2014). Continuing megathrust earthquake potential in Chile after the 2014 Iquique earthquake. *Nature*, 512(7514), 295.
- Hergert, T., & Heidbach, O. (2006). New insights into the mechanism of postseismic stress relaxation exemplified by the 23 June 2001 Mw= 8.4 earthquake in southern Peru. *Geophysical Research Letters*, 33(2).
- Ho, T. C., Satake, K., Watada, S., & Fujii, Y. (2019). Source estimate for the 1960 Chile earthquake from joint inversion of geodetic and transoceanic tsunami data. *Journal of Geophysical Research: Solid Earth*, 124(3), 2812-2828.
- Hoffmann, F., Metzger, S., Moreno, M., Deng, Z., Sippl, C., Ortega-Culaciati, F., & Oncken, O. (2018). Characterizing afterslip and ground displacement rate increase following the 2014 Iquique-Pisagua Mw 8.1 earthquake, Northern Chile. *Journal of Geophysical Research: Solid Earth*, 123(5), 4171-4192.
- Horiuchi, S. S., & Iwamori, H. (2016). A consistent model for fluid distribution, viscosity distribution, and flow-thermal structure in subduction zone. *Journal of Geophysical Research: Solid Earth*, 121(5), 3238-3260.
- Hu, Y. (2011). Deformation processes in great subduction zone earthquake cycles, *PhD thesis*, University of Victoria, Victoria, BC.
- Hu, Y., & Wang, K. (2012). Spherical-Earth finite element model of short-term postseismic deformation following the 2004 Sumatra earthquake. *Journal of Geophysical Research: Solid Earth*, 117(B5).

- Hu, Y., Wang, K., He, J., Klotz, J., & Khazaradze, G. (2004). Three-dimensional viscoelastic finite element model for postseismic deformation of the great 1960 Chile earthquake. *Journal of Geophysical Research: Solid Earth*, 109(B12).
- Hu, Y., Bürgmann, R., Freymueller, J. T., Banerjee, P., & Wang, K. (2014). Contributions of poroelastic rebound and a weak volcanic arc to the postseismic deformation of the 2011 Tohoku earthquake. *Earth, Planets and Space*, 66(1), 1-10.
- Hu, Y., Bürgmann, R., Uchida, N., Banerjee, P., & Freymueller, J. T. (2016). Stress-driven relaxation of heterogeneous upper mantle and time-dependent afterslip following the 2011 Tohoku earthquake. *Journal of Geophysical Research: Solid Earth*, 121(1), 385-411.
- Hyndman, R. D., & Peacock, S. M. (2003). Serpentinization of the forearc mantle. *Earth and Planetary Science Letters*, 212(3-4), 417-432.
- Ide, S. (2012). Variety and spatial heterogeneity of tectonic tremor worldwide. *Journal of Geophysical Research: Solid Earth*, 117, B03302.
- Ioki, K., & Tanioka, Y. (2016). Re-estimated fault model of the 17th century great earthquake off Hokkaido using tsunami deposit data. *Earth and Planetary Science Letters*, 433, 133-138.
- Itoh, Y., Wang, K., Nishimura, T., & He, J. (2019a). Compliant volcanic arc and backarc crust in southern Kurile suggested by interseismic geodetic deformation. *Geophysical Research Letters*, 46(21), 11790-11798.
- Itoh, Y., Nishimura, T., Ariyoshi, K., & Matsumoto, H. (2019b). Interplate slip following the 2003 Tokachi-oki earthquake from ocean bottom pressure gauge and land GNSS data. *Journal of Geophysical Research: Solid Earth*, 124(4), 4205-4230.
- Ivins, E. R., & James, T. S. (1999). Simple models for late Holocene and present-day Patagonian glacier fluctuations and predictions of a geodetically detectable isostatic response. *Geophysical Journal International*, 138(3), 601-624.
- Ivins, E. R., & James, T. S. (2004). Bedrock response to Llanquihue Holocene and present-day glaciation in southernmost South America. *Geophysical Research Letters*, 31(24).
- Ivins, E. R., Watkins, M. M., Yuan, D. N., Dietrich, R., Casassa, G., & Rülke, A. (2011). On-land ice loss and glacial isostatic adjustment at the Drake Passage: 2003–2009. *Journal of Geophysical Research: Solid Earth*, 116, B02403.
- Iwamori, H. (2000). Thermal effects of ridge subduction and its implications for the origin of granitic batholith and paired metamorphic belts. *Earth and Planetary Science Letters*, 181(1-2), 131-144.

- James, T., 1991, Post-glacial deformation, *PhD thesis*, Princeton University, Princeton, NJ.
- James, T. S., Gowan, E. J., Wada, I., & Wang, K. (2009). Viscosity of the asthenosphere from glacial isostatic adjustment and subduction dynamics at the northern Cascadia subduction zone, British Columbia, Canada. *Journal of Geophysical Research: Solid Earth*, 114, B04405.
- Jara, J., Sánchez-Reyes, H., Socquet, A., Cotton, F., Virieux, J., Maksymowicz, A., Díaz-Mojica, J., Walpersdorf, A., Ruiz, J., Cotte, N., & Norabuena, E. (2018). Kinematic study of Iquique 2014 *Mw*8.1 earthquake: Understanding the segmentation of the seismogenic zone. *Earth and Planetary Science Letters*, 503, 131–143.
- Kendrick, E., Bevis, M., Smalley Jr, R., & Brooks, B. (2001). An integrated crustal velocity field for the central Andes. *Geochemistry, Geophysics, Geosystems*, 2(11).
- Khazaradze, G., Wang, K., Klotz, J., Hu, Y., & He, J. (2002). Prolonged post-seismic deformation of the 1960 great Chile earthquake and implications for mantle rheology. *Geophysical Research Letters*, 29(22), 7-1.
- Klein, E., Fleitout, L., Vigny, C., & Garaud, J. D. (2016). Afterslip and viscoelastic relaxation model inferred from the large-scale post-seismic deformation following the 2010 *M* w 8.8 Maule earthquake (Chile). *Geophysical Journal International*, 205(3), 1455-1472.
- Klemann, V., Ivins, E. R., Martinec, Z., & Wolf, D. (2007). Models of active glacial isostasy roofing warm subduction: Case of the South Patagonian Ice Field. *Journal of Geophysical Research: Solid Earth*, 112, B09405.
- Klotz, J., Khazaradze, G., Angermann, D., Reigber, C., Perdomo, R., & Cifuentes, O. (2001). Earthquake cycle dominates contemporary crustal deformation in Central and Southern Andes. *Earth and Planetary Science Letters*, 193(3-4), 437-446.
- Kogan, M. G., Vasilenko, N. F., Frolov, D. I., Freymueller, J. T., Steblov, G. M., Levin, B. W., & Prytkov, A. S. (2011). The mechanism of postseismic deformation triggered by the 2006–2007 great Kuril earthquakes. *Geophysical Research Letters*, 38(6).
- Kogan, M. G., Vasilenko, N. F., Frolov, D. I., Freymueller, J. T., Steblov, G. M., Prytkov, A. S., & Ekström, G. (2013). Rapid postseismic relaxation after the great 2006–2007 Kuril earthquakes from GPS observations in 2007–2011. *Journal of Geophysical Research: Solid Earth*, 118(7), 3691-3706.
- Kostoglodov, V., Husker, A., Shapiro, N. M., Payero, J. S., Campillo, M., Cotte, N., & Clayton, R. (2010). The 2006 slow slip event and nonvolcanic tremor in the Mexican subduction zone. *Geophysical Research Letters*, 37(24), L24301.
- Krawczyk, C. M. *et al.* (2016) in *The Andes: Active Subduction Orogeny* (eds Oncken, O. *et al.*) 171–192 (Springer).



- Kreemer, C., & Zaliapin, I. (2018). Spatiotemporal correlation between seasonal variations in seismicity and horizontal dilatational strain in California. *Geophysical Research Letters*, 45(18), 9559-9568.
- Lay, T., Yue, H., Brodsky, E. E., & An, V. (2014). The 1 April 2014 Iquique, Chile, Mw 8.1 earthquake rupture sequence. *Geophysical Research Letters*, 41, 3818–3825. doi:10.1002/2014GL060238.
- Lange, H., Casassa, G., Ivins, E. R., Schröder, L., Fritsche, M., Richter, A., Groh, A., & Dietrich, R. (2014). Observed crustal uplift near the Southern Patagonian Icefield constrains improved viscoelastic Earth models. *Geophysical Research Letters*, 41(3), 805-812.
- Larsen, C. F., Motyka, R. J., Freymueller, J. T., Echelmeyer, K. A., & Ivins, E. R. (2005). Rapid viscoelastic uplift in southeast Alaska caused by post-Little Ice Age glacial retreat. *Earth and planetary Science letters*, 237(3-4), 548-560.
- Lewis, T. J., Bentkowski, W. H., Davis, E. E., Hyndman, R. D., Souther, J. G., & Wright, J. A. (1988). Subduction of the Juan de Fuca plate: thermal consequences. *Journal of Geophysical Research: Solid Earth*, 93(B12), 15207-15225.
- Li, S., Freymueller, J., & McCaffrey, R. (2016). Slow slip events and time-dependent variations in locking beneath Lower Cook Inlet of the Alaska-Aleutian subduction zone. *Journal of Geophysical Research: Solid Earth*, 121(2), 1060-1079.
- Li, S., Bedford, J., Moreno, M., Barnhart, W. D., Rosenau, M., & Oncken, O. (2018). Spatiotemporal variation of mantle viscosity and the presence of cratonic mantle inferred from 8 years of postseismic deformation following the 2010 Maule, Chile, earthquake. *Geochemistry, Geophysics, Geosystems*, 19(9), 3272-3285.
- Li, S., Fukuda, J. I., & Oncken, O. (2020). Geodetic evidence of time-dependent viscoelastic interseismic deformation driven by megathrust locking in the southwest Japan subduction zone. *Geophysical Research Letters*, 47(4), e2019GL085551.
- Lin, Y. N. N., *et al.* (2013). Coseismic and postseismic slip associated with the 2010 Maule Earthquake, Chile: Characterizing the Arauco Peninsula barrier effect. *Journal of Geophysical Research: Solid Earth*, 118(6), 3142-3159.
- Linde, A. T., & Silver, P. G. (1989). Elevation changes and the great 1960 Chilean earthquake: Support for aseismic slip. *Geophysical Research Letters*, 16(11), 1305-1308.
- Liu, C., Zheng, Y., Wang, R., & Xiong, X. (2015). Kinematic rupture process of the 2014 Chile Mw 8.1 earthquake constrained by strong-motion, GPS static offsets and teleseismic data. *Geophysical Journal International*, 202(2), 1137–1145.
- Lorenzo-Martín, F., Roth, F., & Wang, R. (2006). Inversion for rheological parameters from post-seismic surface deformation associated with the 1960 Valdivia earthquake,

- Chile. *Geophysical Journal International*, 164(1), 75-87.
- Lorito, S., Romano, F., Atzori, S., Tong, X., Avallone, A., McCloskey, J., Cocco, M., Boschi, E., & Piatanesi, A. (2011). Limited overlap between the seismic gap and coseismic slip of the great 2010 Chile earthquake. *Nature Geoscience*, 4(3), 173-177.
- Loveless, J. P., Hoke, G. D., Allmendinger, R. W., González, G., Isacks, B. L., & Carrizo, D. A. (2005). Pervasive cracking of the northern Chilean Coastal Cordillera: New evidence for forearc extension. *Geology*, 33(12), 973-976.
- Loveless, J. P., Allmendinger, R. W., Pritchard, M. E., Garroway, J. L., & González, G. (2009). Surface cracks record long-term seismic segmentation of the Andean margin. *Geology*, 37(1), 23-26.
- Loveless, J. P., Scott, C. P., Allmendinger, R. W., & González, G. (2016). Slip distribution of the 2014 Mw=8.1 Pisagua, northern Chile, earthquake sequence estimated from coseismic fore-arc surface cracks. *Geophysical Research Letters*, 43(19), 10-134.
- Luo, H., Wang, K., Sone, H., & He, J. (2019). A model of shallow viscoelastic relaxation for seismically induced tension cracks in the Chile-Peru forearc. *Geophysical Research Letters*, 46(19), 10773-10781. doi: 10.1029/2019GL084536
- Luo, H., Ambrosius, B., Russo, R. M., Mocanu, V., Wang, K., Bevis, M., & Fernandes, R. (2020). A recent increase in megathrust locking in the southernmost rupture area of the giant 1960 Chile earthquake. *Earth and Planetary Science Letters*, 537, 116200. doi:10.1016/j.epsl.2020.116200.
- Luo, H., & Wang, K. (2021). Postseismic geodetic signature of cold forearc mantle in subduction zones. *Nature Geoscience*, 14(2), 104-109. doi: 10.1038/s41561-020-00679-9.
- Luttrell, K. M., Tong, X., Sandwell, D. T., Brooks, B. A., & Bevis, M. G. (2011). Estimates of stress drop and crustal tectonic stress from the 27 February 2010 Maule, Chile, earthquake: Implications for fault strength. *Journal of Geophysical Research: Solid Earth*, 116, B11401.
- Malz, P., Meier, W., Casassa, G., Jaña, R., Skvarca, P., & Braun, M. H. (2018). Elevation and mass changes of the Southern Patagonia Icefield derived from TanDEM-X and SRTM data. *Remote Sensing*, 10(2), 188.
- Mark, H. F., Wiens, D., Pourpoint, M., Magnani, M.B., Ivins, E.R., Richter, A., & Barrientos, S.E. (2020). Seismic structure and the extent of the slab window beneath the Northern and Southern Patagonia Icefields: In *AGU Fall Meeting 2020*, AGU, 1–17 December.
- Materna, K., Bartlow, N., Wech, A., Williams, C., & Bürgmann, R. (2019). Dynamically triggered changes of plate interface coupling in Southern Cascadia. *Geophysical*

- Research Letters*, 46(22), 12890-12899.
- Mavrommatis, A. P., Segall, P., & Johnson, K. M. (2014). A decadal-scale deformation transient prior to the 2011 Mw 9.0 Tohoku-oki earthquake. *Geophysical Research Letters*, 41(13), 4486-4494.
- Melnick, D., *et al.* (2018). Back to full interseismic plate locking decades after the giant 1960 Chile earthquake. *Nature communications*, 9(1), 1-10.
- Melosh, H. J., & Raefsky, A. (1981). A simple and efficient method for introducing faults into finite element computations. *Bulletin of the Seismological Society of America*, 71(5), 1391-1400.
- Moreno, M. S., Bolte, J., Klotz, J., & Melnick, D. (2009). Impact of megathrust geometry on inversion of coseismic slip from geodetic data: Application to the 1960 Chile earthquake. *Geophysical Research Letters*, 36(16), L16310.
- Moreno, M., *et al.* (2011). Heterogeneous plate locking in the South–Central Chile subduction zone: Building up the next great earthquake. *Earth and Planetary Science Letters*, 305(3-4), 413-424.
- Moreno, M., *et al.* (2012). Toward understanding tectonic control on the Mw 8.8 2010 Maule Chile earthquake. *Earth and Planetary Science Letters*, 321, 152-165.
- Müller, R. D., Sdrolias, M., Gaina, C., & Roest, W. R. (2008). Age, spreading rates, and spreading asymmetry of the world's ocean crust. *Geochemistry, Geophysics, Geosystems*, 9(4), Q04006.
- Muto, J., Moore, J. D. P., Barbot, S., Iinuma, T., Ohta, Y., & Iwamori, H. (2019). Coupled afterslip and transient mantle flow after the 2011 Tohoku earthquake. *Science advances*, 5(9), eaaw1164.
- Nakagawa, H. (2009). Development and validation of GEONET new analysis strategy (Version 4) (in Japanese). *J. Geogr. Surv. Inst.*, 118, 1-8.
- Nicolsky, D. J., Freymueller, J. T., Witter, R. C., Suleimani, E. N., & Koehler, R. D. (2016). Evidence for shallow megathrust slip across the Unalaska seismic gap during the great 1957 Andreanof Islands earthquake, eastern Aleutian Islands, Alaska. *Geophysical Research Letters*, 43(19), 10-328.
- Nield, G. A., Barletta, V. R., Bordonì, A., King, M. A., Whitehouse, P. L., Clarke, P. J., Domack, E., Scambos, T.A., & Berthier, E. (2014). Rapid bedrock uplift in the Antarctic Peninsula explained by viscoelastic response to recent ice unloading. *Earth and Planetary Science Letters*, 397, 32-41.
- Nishimura, T. (2014). Pre-, co-, and post-seismic deformation of the 2011 Tohoku-oki earthquake and its implication to a paradox in short-term and long-term deformation. *Journal of disaster research*, 9(3), 294-302.

- Obara, K. (2011). Characteristics and interactions between non-volcanic tremor and related slow earthquakes in the Nankai subduction zone, southwest Japan. *Journal of Geodynamics*, 52(3-4), 229-248.
- Ozawa, S., Nishimura, T., Munekane, H., Suito, H., Kobayashi, T., Tobita, M., & Imakiire, T. (2012). Preceding, coseismic, and postseismic slips of the 2011 Tohoku earthquake, Japan. *Journal of Geophysical Research: Solid Earth*, 117(B7), B07404.
- Pagli, C., *et al.* (2007). Glacio-isostatic deformation around the Vatnajökull ice cap, Iceland, induced by recent climate warming: GPS observations and finite element modeling. *Journal of Geophysical Research: Solid Earth*, 112, B08405.
- Peltier, W. R. (1974). The impulse response of a Maxwell Earth. *Reviews of Geophysics*, 12(4), 649-669.
- Peña, C., Heidbach, O., Moreno, M., Bedford, J., Ziegler, M., Tassara, A., & Oncken, O. (2019). Role of lower crust in the postseismic deformation of the 2010 Maule earthquake: Insights from a model with power-law rheology. *Pure and Applied Geophysics*, 176(9), 3913-3928.
- Peña, C., Heidbach, O., Moreno, M., Bedford, J., Ziegler, M., Tassara, A., & Oncken, O. (2020). Impact of power-law rheology on the viscoelastic relaxation pattern and afterslip distribution following the 2010 Mw 8.8 Maule earthquake. *Earth and Planetary Science Letters*, 542, 116292.
- Plafker, G. (1969). Tectonics of the March 27, 1964 Alaska earthquake, U.S. Geological Survey Professional Paper 543-I, (<https://pubs.usgs.gov/pp/0543i/>).
- Plafker, G., & Savage, J. C. (1970). Mechanism of the Chilean earthquakes of May 21 and 22, 1960. *Geological Society of America Bulletin*, 81(4), 1001-1030.
- Pollitz, F. F., *et al.* (2011). Coseismic slip distribution of the February 27, 2010 Mw 8.8 Maule, Chile earthquake. *Geophysical Research Letters*, 38, L09309.
- Pollitz, F. F. (2019). Lithosphere and shallow asthenosphere rheology from observations of post-earthquake relaxation. *Physics of the Earth and Planetary Interiors*, 293, 106271.
- Pritchard, M. E., & Simons, M. (2006). An aseismic slip pulse in northern Chile and along-strike variations in seismogenic behavior. *Journal of Geophysical Research: Solid Earth*, 111, B08405.
- Rech, J. A., Quade, J., & Hart, W. S. (2003). Isotopic evidence for the source of Ca and S in soil gypsum, anhydrite and calcite in the Atacama Desert, Chile. *Geochimica et Cosmochimica Acta*, 67, 575-586. doi: 10.1016/S0016-7037(02)01175-4.
- Richter, A., *et al.* (2016). Crustal deformation across the Southern Patagonian Icefield observed by GNSS. *Earth and Planetary Science Letters*, 452, 206-215.

- Richter, A., *et al.* (2019). The rapid and steady mass loss of the patagonian icefields throughout the grace era: 2002–2017. *Remote Sensing*, 11(8), 909.
- Rignot, E., Rivera, A., & Casassa, G. (2003). Contribution of the Patagonia Icefields of South America to sea level rise. *Science*, 302(5644), 434-437.
- Rivera, A., Benham, T., Casassa, G., Bamber, J., & Dowdeswell, J. A. (2007). Ice elevation and areal changes of glaciers from the Northern Patagonia Icefield, Chile. *Global and Planetary Change*, 59(1-4), 126-137.
- Rodell, M., Famiglietti, J. S., Wiese, D. N., Reager, J. T., Beaulieu, H. K., Landrerer, F. W., & Lo, M. H. (2018). Emerging trends in global freshwater availability. *Nature*, 557(7707), 651-659.
- Rodriguez, E. E., & Russo, R. M. (2020). Southern Chile crustal structure from teleseismic receiver functions: Responses to ridge subduction and terrane assembly of Patagonia. *Geosphere*, 16(1), 378-391.
- Ruiz, S., Metois, M., Fuenzalida, A., Ruiz, J., Leyton, F., Grandin, R., Vigny, C., Madariaga, R., & Campos, J. (2014). Intense foreshocks and a slow slip event preceded the 2014 Iquique Mw 8.1 earthquake. *Science*, 345(6201), 1165–1169.
- Russo, R. M., VanDecar, J. C., Comte, D., Mocanu, V. I., Gallego, A., & Murdie, R. E. (2010a). Subduction of the Chile Ridge: Upper mantle structure and flow. *GSA Today*, 20(9), 4-10.
- Russo, R. M., Gallego, A., Comte, D., Mocanu, V. I., Murdie, R. E., & VanDecar, J. C. (2010b). Source-side shear wave splitting and upper mantle flow in the Chile Ridge subduction region. *Geology*, 38(8), 707-710.
- Russo, R.M., Luo, H., Wang, K., Ambrosius, B., Mocanu, V., He, J., James, T., Bevis, M. & Fernandes, R. (2021). Lateral variation in slab window viscosity inferred from GNSS-observed uplift due to recent mass loss at Patagonia icefields. *Geology*. doi: 10.1130/G49388.1.
- Sáez, M., Ruiz, S., Ide, S., & Sugioka, H. (2019). Shallow nonvolcanic tremor activity and potential repeating earthquakes in the Chile Triple Junction: seismic evidence of the subduction of the active Nazca–Antarctic spreading center. *Seismological Research Letters*, 90(5), 1740-1747.
- Sawai, Y., Satake, K., Kamataki, T., Nasu, H., Shishikura, M., Atwater, B. F., Horton, B. P., Kelsey, H.M., Nagumo, T., & Yamaguchi, M. (2004). Transient uplift after a 17th-century earthquake along the Kuril subduction zone. *Science*, 306(5703), 1918-1920.
- Schurr, B., *et al.*, (2014). Gradual unlocking of plate boundary controlled initiation of the 2014 Iquique earthquake. *Nature*, 512(7514), 299.

- Scott, C. P., Allmendinger, R. W., González, G., & Loveless, J. P. (2016). Coseismic extension from surface cracks reopened by the 2014 Pisagua, northern Chile, earthquake sequence. *Geology*, 44(5), 387-390.
- Sone, H., & Condon, K. J. (2017). Ductile behavior of thermally-fractured granite rocks. 51st US Rock Mechanics / Geomechanics Symposium, San Francisco, CA, June 25-28, paper 17-443.
- Sone, H., & Zoback, M. D. (2013). Mechanical properties of shale-gas reservoir rocks — Part 2: Ductile creep, brittle strength, and their relation to the elastic modulus. *Geophysics*, 78(5), D393-D402.
- Sone, H., & Zoback, M. D. (2014). Time-dependent deformation of shale gas reservoir rocks and its long-term effect on the in situ state of stress. *International Journal of Rock Mechanics and Mining Sciences*, 69, 120-132.
- Suito, H. (2017). Importance of rheological heterogeneity for interpreting viscoelastic relaxation caused by the 2011 Tohoku-Oki earthquake. *Earth, Planets and Space*, 69(1), 1-12.
- Suito, H., & Freymueller, J. T. (2009). A viscoelastic and afterslip postseismic deformation model for the 1964 Alaska earthquake. *Journal of Geophysical Research: Solid Earth*, 114(B11).
- Sun, T., *et al.* (2014). Prevalence of viscoelastic relaxation after the 2011 Tohoku-oki earthquake. *Nature*, 514(7520), 84-87.
- Sun, T., & Wang, K. (2015). Viscoelastic relaxation following subduction earthquakes and its effects on afterslip determination. *Journal of Geophysical Research: Solid Earth*, 120, 1329–1344. doi:10.1002/2014JB011707.
- Sun, T., Wang, K., & He, J. (2018). Crustal deformation following great subduction earthquakes controlled by earthquake size and mantle rheology. *Journal of Geophysical Research: Solid Earth*, 123(6), 5323-5345.
- Syracuse, E. M., van Keken, P. E., & Abers, G. A. (2010). The global range of subduction zone thermal models. *Physics of the Earth and Planetary Interiors*, 183(1-2), 73-90.
- Thatcher, W. (1984). The earthquake deformation cycle at the Nankai Trough, southwest Japan. *Journal of Geophysical Research: Solid Earth*, 89(B5), 3087-3101.
- Tong, X., *et al.* (2010). The 2010 Maule, Chile earthquake: Downdip rupture limit revealed by space geodesy. *Geophysical Research Letters*, 37, L24311.
- Tsang, L. L.H., *et al.* (2016). Afterslip following the 2007 Mw 8.4 Bengkulu earthquake in Sumatra loaded the 2010 Mw 7.8 Mentawai tsunami earthquake rupture zone. *Journal of Geophysical Research: Solid Earth*, 121(12), 9034-9049.

- Tsumura, N., Matsumoto, S., Horiuchi, S., & Hasegawa, A. (2000). Three-dimensional attenuation structure beneath the northeastern Japan arc estimated from spectra of small earthquakes. *Tectonophysics*, 319(4), 241-260.
- van Dinther, Y., Preiswerk, L. E., & Gerya, T. V. (2019). A secondary zone of uplift due to megathrust earthquakes. *Pure and Applied Geophysics*, 176(9), 4043-4068.
- Vigny, C., *et al.* (2011). The 2010 Mw 8.8 Maule megathrust earthquake of central Chile, monitored by GPS. *Science*, 332(6036), 1417-1421.
- Von Herzen, R., Ruppel, C., Molnar, P., Nettles, M., Nagihara, S., & Ekström, G. (2001). A constraint on the shear stress at the Pacific-Australian plate boundary from heat flow and seismicity at the Kermadec forearc. *Journal of Geophysical Research: Solid Earth*, 106(B4), 6817-6833.
- Wada, I., & Wang, K. (2009). Common depth of slab-mantle decoupling: Reconciling diversity and uniformity of subduction zones. *Geochemistry, Geophysics, Geosystems*, 10, Q10009.
- Wahr, J., & Wyss, M. (1980). Interpretation of postseismic deformation with a viscoelastic relaxation model. *Journal of Geophysical Research: Solid Earth*, 85(B11), 6471-6477.
- Wallace, L. M., & Beavan, J. (2010). Diverse slow slip behavior at the Hikurangi subduction margin, New Zealand. *Journal of Geophysical Research: Solid Earth*, 115, B12402.
- Wang, K., He, J., Dragert, H., & James, T. S. (2001). Three-dimensional viscoelastic interseismic deformation model for the Cascadia subduction zone. *Earth, Planets and Space*, 53(4), 295-306.
- Wang, K., Hu, Y., Bevis, M., Kendrick, E., Smalley Jr, R., Vargas, R. B., & Lauría, E. (2007). Crustal motion in the zone of the 1960 Chile earthquake: Detangling earthquake-cycle deformation and forearc-sliver translation. *Geochemistry, Geophysics, Geosystems*, 8(10), Q10010.
- Wang, K., Hu, Y., & He, J. (2012). Deformation cycles of subduction earthquakes in a viscoelastic Earth. *Nature*, 484(7394), 327.
- Wang, K., Brown, L., Hu, Y., Yoshida, K., He, J., & Sun, T. (2019). Stable forearc stressed by a weak megathrust: Mechanical and geodynamic implications of stress changes caused by the M= 9 Tohoku-oki earthquake. *Journal of Geophysical Research: Solid Earth*, 124(6), 6179-6194.
- Wang, K., Sun, T., Brown, L., Hino, R., Tomita, F., Kido, M., Iinuma, T., Kodaira, S., & Fujiwara, T. (2018). Learning from crustal deformation associated with the M9 2011 Tohoku-oki earthquake. *Geosphere*, 14(2), 552-571.

- Wang, K., & Tréhu, A. M. (2016). Invited review paper: Some outstanding issues in the study of great megathrust earthquakes—The Cascadia example. *Journal of Geodynamics*, 98, 1-18.
- Wang, P. L., Engelhart, S. E., Wang, K., Hawkes, A. D., Horton, B. P., Nelson, A. R., & Witter, R. C. (2013). Heterogeneous rupture in the great Cascadia earthquake of 1700 inferred from coastal subsidence estimates. *Journal of Geophysical Research: Solid Earth*, 118(5), 2460-2473.
- Wang, Z., Zhao, D., Liu, X., Chen, C., & Li, X. (2017). P and S wave attenuation tomography of the Japan subduction zone. *Geochemistry, Geophysics, Geosystems*, 18(4), 1688-1710.
- Wei, S. S., & Wiens, D. A. (2018). P-wave attenuation structure of the Lau back-arc basin and implications for mantle wedge processes. *Earth and Planetary Science Letters*, 502, 187-199.
- Weiss, J. R., *et al.* (2019). Illuminating subduction zone rheological properties in the wake of a giant earthquake. *Science advances*, 5(12), eaax6720.
- Willis, M. J., Melkonian, A. K., Pritchard, M. E., & Ramage, J. M. (2012a). Ice loss rates at the Northern Patagonian Icefield derived using a decade of satellite remote sensing. *Remote Sensing of Environment*, 117, 184-198.
- Willis, M. J., Melkonian, A. K., Pritchard, M. E., & Rivera, A. (2012b). Ice loss from the Southern Patagonian ice field, South America, between 2000 and 2012. *Geophysical research letters*, 39, L17501.
- Yagi, Y., Okuwaki, R., Enescu, B., Hirano, S., Yamagami, Y., Endo, S., & Komoro, T. (2014). Rupture process of the 2014 Iquique Chile Earthquake in relation with the foreshock activity. *Geophysical Research Letters*, 41(12), 4201–4206.  
<http://doi.org/10.1002/2014GL060274>.
- Yokota, Y., & Koketsu, K. (2015). A very long-term transient event preceding the 2011 Tohoku earthquake. *Nature communications*, 6(1), 1-5.
- Yokota, Y., Ishikawa, T., & Watanabe, S. I. (2018). Seafloor crustal deformation data along the subduction zones around Japan obtained by GNSS-A observations. *Scientific data*, 5(1), 1-11.
- Yue, H., Lay, T., Rivera, L., An, C., Vigny, C., Tong, X., & Baez Soto, J. C. (2014). Localized fault slip to the trench in the 2010 Maule, Chile Mw= 8.8 earthquake from joint inversion of high-rate GPS, teleseismic body waves, InSAR, campaign GPS, and tsunami observations. *Journal of Geophysical Research: Solid Earth*, 119(10), 7786-7804.



Zumberge, J. F., Heflin, M. B., Jefferson, D. C., Watkins, M. M., & Webb, F. H. (1997). Precise point positioning for the efficient and robust analysis of GPS data from large networks. *Journal of geophysical research: solid earth*, 102(B3), 5005-5017.